



Politecnico di Torino

DIPARTIMENTO ENERGIA "GALILEO FERRARIS"
Master of Science in Energy and Nuclear Engineering

M.Sc. THESIS

Influence of vegetation on vertical mass exchange velocity in urban street canyon

Candidate:
Giacomo Balestrieri

Thesis Advisor:
Andrea Carpignano

Research Supervisor:
Pietro Salizzoni

March 2021

Contents

Summary	6
1 Introduction	8
1.1 Generalities	8
1.1.1 Mediterranean climate and climate changes	8
1.1.2 The Urban Heat Island	10
1.2 The effect of vegetation in urban areas	13
1.2.1 The Urban Cool Island	13
1.2.2 Influence of land cover configuration	15
1.3 Aim of the study	16
2 Methodology, relevant phenomena and models	19
2.1 Influence of vegetation on pollutant concentrations	19
2.1.1 Reference scenario	20
2.1.2 Effect of the presence of trees	21
2.1.3 Effect of street aspect ratio	23
2.1.4 Effect of wind direction	24
2.1.5 Particles deposition on vegetation	25
2.1.6 Wash-out process	28
2.2 The Atmospheric Boundary Layer	29
2.2.1 Spatial scales	30
2.2.2 Wind profile in the Atmospheric Boundary Layer	31
2.2.3 Dispersion in the Atmospheric Boundary Layer	34
2.2.4 Urban canopy flow	36
2.2.5 Dispersion in the urban canopy	38

3	Setup, measurement instruments and experimental methods	41
3.1	The experimental setup	41
3.2	The measurement techniques	44
3.2.1	The Flame Ionization Detector	44
3.2.2	The Laser Doppler Anemometer	46
3.2.3	The Pitot tube	50
4	Canyon alignment and wind profile in the tunnel	51
4.1	Canyon alignment	51
4.2	Wind profile	53
4.2.1	Wind profiles along wind direction	53
4.2.2	Characteristic parameters of the wind profile	58
5	Preliminary measurements of the vertical exchange velocity u_d	61
5.1	Mass exchange velocity u_d	61
5.2	Data treatment	64
5.3	Mass conservation verification	65
5.4	Sensitivity analysis on the grid refinition	70
5.5	Results	73
5.5.1	Concentration maps	73
5.5.2	Flux maps	76
5.5.3	Vertical exchange velocity	80
6	Analysis of the time series of $w'c'$	83
6.1	Traditional statistics	84
6.2	Complex network analysis	92
6.2.1	Introduction	92
6.2.2	Network mathematical formulation	95
6.2.3	Network types and construction	97
6.2.4	Visibility graphs	99
6.2.5	Network metrics	101
6.2.6	Results	105
7	Conclusions	110

List of Figures

1.1	Trend of average monthly temperature in Turin	10
1.2	UHI temperature profile	11
1.3	Green spaces' cooling effect	13
2.1	Principal flow structures inside a street canyon	21
2.2	Flow zones around a single building	37
2.3	Flow regimes around multiple buildings	38
3.1	Wind tunnel at the École Centrale de Lyon	41
3.2	Street network inside the wind tunnel	43
3.3	Tree configuration and reference system with control volume . . .	44
3.4	Convergence of FID measures	46
3.5	LDA images	48
3.6	Convergence of LDA measures	49
4.1	Concentration profiles along the reference street canyon	52
4.2	Sketch of the four points where wind profiles are measured	54
4.3	Wind profiles along x direction	55
4.4	Vertical profiles obtained during wind profile characterization . .	56
4.5	Extended wind profile obtained with LDA and Pitot tube	57
4.6	Results of linear regression in the interval of constant Reynolds stresses	58
5.1	Shear layer vortices	62
5.2	Velocity streamlines inside the street canyon	62
5.3	Measurement grids	63

5.4	Grid adopted for $\overline{w'c'}$, \overline{w} and \overline{c} measures	66
5.5	Best-fit for measured values	67
5.6	Maps of measured values and relative 3D canyon configuration and measurement grid	68
5.7	Results of the integral	69
5.8	Sensitivity analysis on single sections/profiles	70
5.9	Sensitivity analysis on the measurement grid	71
5.10	Combined sensitivity analysis	72
5.10	Concentration maps	75
5.10	Concentration profiles along y	76
5.11	$\overline{w'c'}$ maps	78
5.12	$\overline{w} \cdot \overline{c}$ maps	79
5.13	\overline{w} maps	80
5.14	\overline{c} maps	81
6.1	Examples of curves with different skewness and kurtosis	85
6.2	Traditional statistics of $w'c'$	86
6.3	Turbulent and mean mass fluxes profiles	87
6.4	Exiting flowrate along y	88
6.5	Spectra of $w'c'$	90
6.6	Examples of time series and corresponding networks	95
6.7	Building process of a network from a time series with the visibil- ity algorithm	99
6.8	Network metrics from $w'c'$ time-series	107

Summary

The aim of the present thesis has been to study the effect of the presence of trees on the vertical mass transport velocity u_d in a long street canyon perpendicular to the wind velocity, a parameter that describes the mass transfer between the inner region of the canyon and the external atmosphere. To do so, a model representing a typical city network has been recreated in a recirculating windtunnel, and concentration measures and wind velocity measures have been taken both inside the reference street and on its rooftop, in order to define the flow field and the concentration maps necessary for the estimation of u_d . Two different configurations have been analyzed: one in absence of trees and one with two rows of 21 equally spaced trees each.

The study is multidisciplinary, because fluidodynamic knowledge is needed to fully comprehend the dynamics of the wind profile in the Atmospheric Boundary Layer, but also energetic knowledge is required for understanding the general frame in which the work is inserted (effects of pollution on humans and on climate change, correct use of vegetation to reduce the impact of pollutants) and, more specifically, for reading concentration maps and understanding what are the main phenomena that influence them.

Before executing concentration and wind velocity measurements, some preliminary analyses have been performed. In particular, a verification of the perfect orientation of the street canyon and a verification of the mass conservation within the canyon have been carried out, together with the characterization of the parameters of the wind profile along the windtunnel.

Concentration measures are taken with a Flame Ionization Detector, while wind velocity measures are taken with a Laser Doppler Anemometer. Also coupled measures of wind velocity and concentration have been taken, joining the

work of the two instruments. After the experimental campaign, u_d has been calculated for both setups and concentration maps have been analyzed, in order to understand the effect of the presence of trees.

A further analysis on the time-series of coupled velocity-concentration measures has been finally performed, adopting both traditional statistics such as variance, skewness and kurtosis, and a network-based analysis. The aim is to describe the mass transport phenomenon in a more detailed way, as well as introducing an alternative methodology (the network-based analysis) for time-series analysis of fluidodynamic measures, highlighting thus analogies and differences with respect to a more traditional approach.

1. Introduction

Climate change has become a very relevant issue in the past years and decades, especially when considering its effects on the urban environment. Nowadays around 55% of the world population lives in cities, but this percentage is expected to rise up to 68% within 2050, according to the United Nations. Hence it is a crucial matter for human health to correctly define which are the main concerns related to urban climate change and how to possibly mitigate them.

1.1 *Generalities*

1.1.1 *Mediterranean climate and climate changes*

Generally speaking, Mediterranean climate is characterized by high spatial variability in both seasonal mean temperatures and total precipitations, and this fact is mainly due to the complex orography of the area. This region is also considered to be a "climate change hot-spot", an area which is very responsive to global climate change (Giorgi 2006). Many studies also found out a relationship between large scale atmospheric circulation modes in the Northern Hemisphere (the North Atlantic Oscillation (NAO), the East Atlantic pattern, the East Atlantic/Western Russia pattern and the Scandinavian pattern) and the Mediterranean climate, especially during winter season; in particular, Mediterranean winter precipitations and monthly precipitations variability are heavily influenced by these circulation modes (Xoplaki et al. 2004).

If the whole Mediterranean region is considered, without focusing on a city scale, it is possible to see from observational data and gridded products that in the last 60 years a significant increase in the mean summer temperature has been

experienced, together with a decrease in summer and winter precipitations (Ulbrich et al. 2013). Together with mean temperatures, also temperature extremes (defined by the 5th and 95th percentiles of the distributions of daily observations) undergo a relevant change in the last decades: summer hot extremes are increasing almost everywhere in the Mediterranean, while winter cold extremes decrease in some areas (western and central Mediterranean) and increase in others (eastern Mediterranean); warm winter extremes, on the other hand, increase everywhere. These trends seem to have intensified after 1990, especially over the central and eastern Mediterranean (Efthymiadis et al. 2011). Hot extremes increase is also tightly linked to the higher frequency of heatwaves (such as the ones experienced in 2003 and in 2010), which may be very dangerous for human health in relation to heat-related mortality and heat stresses. Moreover, according to regional multi-model experiments, there's a steep increase in the probability of experiencing these "mega-heatwaves" (by a factor of 5-10) within the next 40 years (Ulbrich et al. 2013). Also sea level changes are relevant in the Mediterranean, as many cities are located on coastal areas and the whole region is centered around the sea. Since global temperatures are expected to rise, also a global sea level rise is expected, due to mass addition from inland ice sheets and glaciers.

As an example, in fig. 1.1 is shown the trend over the last 30 years (from 1990 to 2020) of the average monthly temperature in the metropolitan city of Turin, in the north of Italy (Nimbus 2020). The graph shows a slight increase in the average temperatures for all the considered periods (four months, representative of the four seasons), with temperature fluctuations. However, by averaging for each season the temperatures from 1990 to 2005 and then from 2006 to 2020, results show that in the last 15 years temperatures have risen with respect to the previous 15 years (+0.357 C in winter, +1.689 C in spring, +1.258 C in summer and +0.938 C in autumn), giving thus a further confirmation of the trend faced by previous studies.

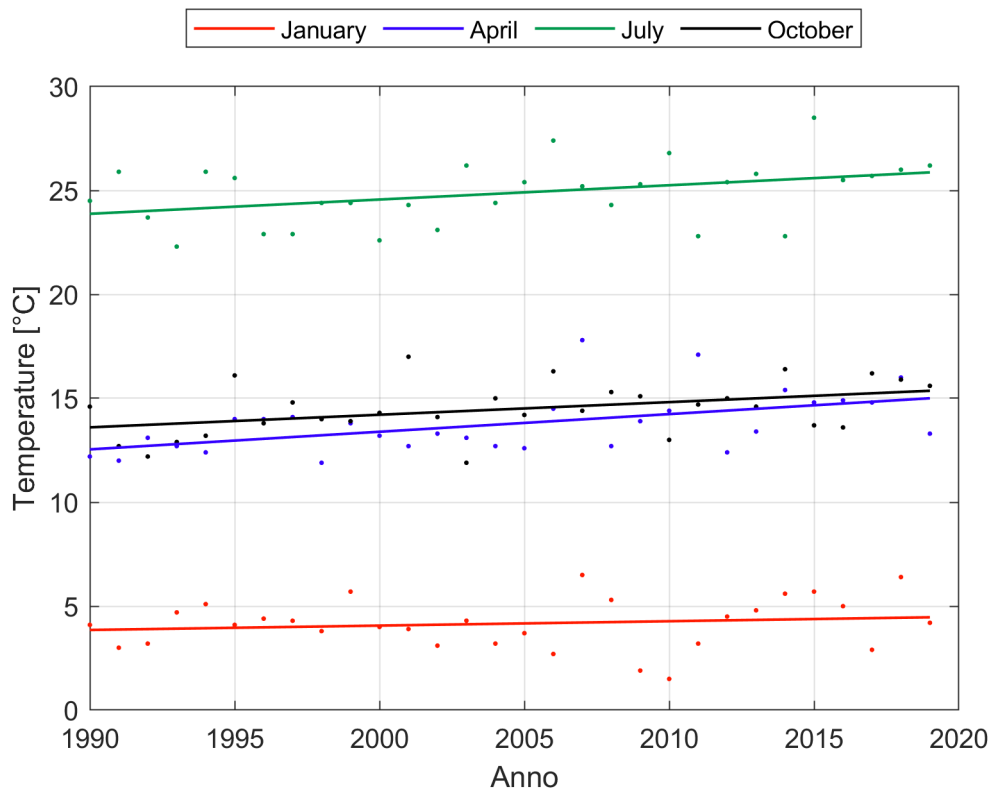


Figure 1.1: Trend of average monthly temperature in Turin. The dots represent the temperatures measured by meteorological stations, while the lines are regression lines computed over the 1990-2020 period for the considered months.

1.1.2 The Urban Heat Island

All these results due to climate change at a regional scale have to be joined with the effects of continuous expansion of cities, phenomenon that by itself is able to generate peculiar micro-climatic features. Negative effects on micro-climate due to the presence of cities (and their expansion) are known since the 1950s thanks to Ake Sundborg, who firstly wrote about the "existence of a warm core coinciding with the most densely build up and populated portion of the city". Urbanization deeply affects also other climatic variables such as precipitations, temperatures, humidity, etc. since the artificial structures that are built (tall buildings, pavements, paved streets, etc.) change the response of the surface with respect to rural areas (Choudhary and Tripathi 2018).

Moreover, also inside already existing urban areas, there's an increasing

trend of reduction of vegetation cover, which enhances the gap between cities and rural areas. The main issue related to the presence and growth of urban areas is the so-called Urban Heat Island (UHI): it is defined as urban areas being warmer than surrounding rural areas (Oake 1982).

Two are the types of UHI that rise in metropolitan areas: surface UHI and atmospheric UHI. The first one is due to the difference in the features of surfaces (in particular albedo and surface geometry) between urban and rural areas. Urban surfaces are characterized by a lower albedo (lower reflection of sun beams) and more complex geometry, which tends to trap escaping radiations, in particular during night time, reducing the rate of cooling; this results in a higher surface temperature with respect to rural areas. Atmospheric UHI, on the other hand, is the phenomenon in which urban air gets warmer than the adjacent rural air temperature (Bhargava et al. 2017).

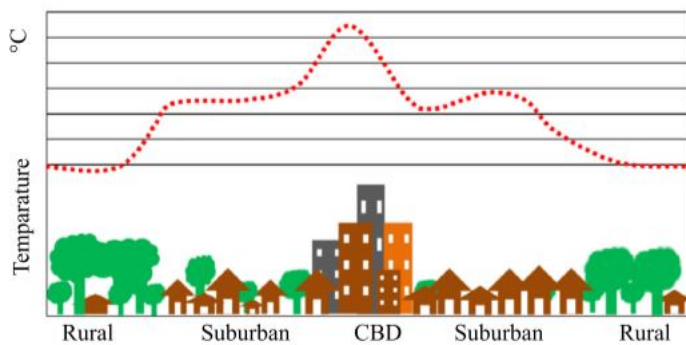


Figure 1.2: UHI temperature profile

Atmospheric UHI is further divided into a "canopy level" and a "boundary level": the first one refers to the layer that goes from ground level to the roof top level, while the second one refers to the layer that is above the previous one,

from the roof top level to a height where the presence of the city does not influence the atmosphere anymore. It is quite obvious that surface UHI tends to increase atmospheric UHI in the canopy level, since surfaces and canopy layer are very close to each other. A particular feature of this phenomenon is the fact that it is powered by city expansion, for the reasons mentioned before, but as urban areas grow, temperatures in the already existing part of the city remain almost unchanged (if variations are present, they are of minor importance, between 0.3°C and 2°C), while they rise only in the new urbanized areas.

The UHI strongly depends on atmospheric conditions, in particular wind speed and cloud cover: stronger UHIs occur under low wind speed and low cloud cover. In fact, with low winds, advection of heat away from the city is reduced and there's a higher trapping of radiations within the urban canyon. Cloud cover, on the other hand, decreases the UHI effect because longwave radiation coming from the clouds has a higher impact on rural areas (which are more exposed to the sky), reducing thus the temperature difference between city and surroundings. For these reasons it is crucial to understand how climate change (on a regional scale) will affect these parameters, in order to foresee how UHIs will develop in the future both in terms of frequency and intensity (Chapman et al. 2017). As a result, current UHIs cannot be simply added to climate change projections, since climate change itself is a phenomenon that affects the UHI formation.

The UHI not only has influence on human health issues (respiratory and cardiovascular problems for instance), but also on human energy consumption; in fact, especially during summer, the demand of electricity for cooling rises from 2% to 4% for every 1°C of temperature increase. Since typical yearly averaged temperature differences between urban and rural environment are between 1°C and 3°C, with peaks that can reach 12°C (Bhargava et al. 2017), it is clear that during summer the UHI leads to an energy consumption increase. However, in winter, its effect is opposite: temperatures are warmer and less heating is needed. Globally, the net anthropogenic heat release (due to cooling and heating) caused by the UHI "would either increase or decrease the UHI depending on whether the reduction in heating or increase in cooling requirements was larger" (Oleson 2012). It is thus important to take into account anthropogenic heat in the evaluation of the phenomenon, otherwise there's the risk of underestimating urban temperatures, particularly in the most densely populated areas where anthropogenic heat releases are highest (Chapman et al. 2017).

1.2 The effect of vegetation in urban areas

1.2.1 The Urban Cool Island

The main effect of increasing urbanization and city growth is the fast reduction of green areas (Land-Use and Land-Cover change). This has a large impact on the urban micro-climate, since not only surface properties of green areas are better (higher albedo and reflectivity with respect to urban surfaces, lower thermal inertia), but also because natural features have the ability to absorb thermal energy through the evapotranspiration process, which describes the loss of water from a plant as vapour into the atmosphere. Evapotranspiration uses energy coming from solar radiation and increases latent rather than sensible heat; as a result, leaves are cooled down, as well as their surroundings. This reduces the amount of thermal energy reaching the earth's surface as well as the amount of heat that is emitted towards the atmosphere (Bhargava et al. 2017; Bowler et al. 2010); natural features also provide shadowing effect, reducing the heat build-up.

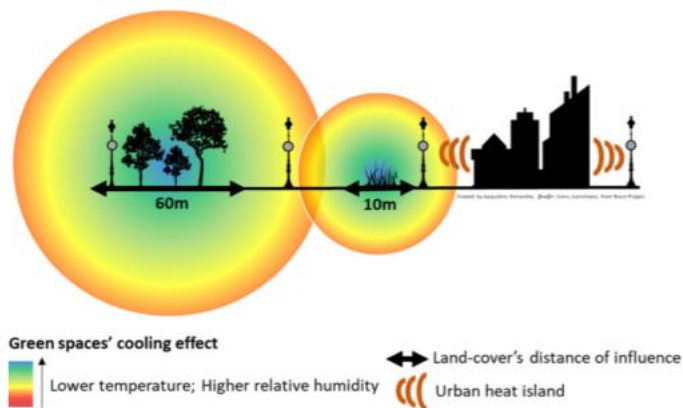


Figure 1.3: Green spaces' cooling effect

As a result, mitigation measures such as increased greening have proven to be very effective in reducing the effects of urban growth and consequent UHI; in particular, urban greening shows its maximum positive effects in the afternoon and evening hours, when the evaporative cooling by vegetation has a great impact (Fallmann et al. 2014). The positive effect on both temperature and humidity generated at urban level by green infrastructure is often referred to as "Urban cool island", in contrast to the "Urban heat island". For example, studies show that a single park can reduce temperatures

from 1°C to 7°C, depending on its characteristics (size, shape, type of vegetative cover), and that the cooling effect not only influences the park area, but also its surroundings (Georgakis and Santamouris 2017; Oliveira et al. 2011).

Not all green features, however, have the same impact on urban microclimate: usually the main distinction is made between tree canopy area and herbaceous vegetation, and in order to prove the effects of such types of green cover on climatic variables correlation coefficients relating each land-cover type with microclimate values have been calculated; also the macroclimate in which the study is performed influences the magnitude of the results. This analysis is done not only inside the green areas considered, but also on the surroundings, measuring thus the maximum distance at which each kind of cover is expected to have an impact (Grilo et al. 2020).

Results show that, for Mediterranean regions, there is a negative correlation between tree canopy area and mean summer temperature (meaning that if tree canopy area increases, mean summer temperature is expected to decrease in the area), as well as a positive correlation between tree canopy area and mean summer and winter relative humidity (meaning that if tree canopy area increases, mean summer and winter relative humidity are expected to increase as well in the area). Also for herbaceous cover correlations are similar, but the magnitude of positive effects is lower. This fact is also proven by the analysis of the distance at which vegetation has an impact on climate variables: trees have an impact on mean summer temperature and relative humidity up to a distance of 60 m, while shrubs and grass cover have effect only up to 10 m (Grilo et al. 2020).

These facts show that the choice of vegetation cover is very relevant when aiming at optimizing urban cooling island effect, with trees being the most efficient feature, most probably thanks to their shading effect and high evapotranspiration capacity with respect to herbaceous cover. While green areas contribute to a reduction of the UHI effect, grey areas (which include buildings, roads, pavements, parking lots etc.), as expected, have the opposite effect, as their coefficients show a positive correlation between grey cover area and mean summer temperature and a negative correlation coefficient between grey cover

area and mean relative humidity. The former is due to the high energy absorption by dark surfaces and by the higher thermal mass of buildings, which absorb heat during the day and release it overnight, contributing to the increase of mean temperature. The latter is caused by the fact that, being those surfaces impermeable, they promote water runoff into the stormwater system, reducing the amount of water absorbed by vegetation and thus available for evapotranspiration and evaporation processes (Grilo et al. 2020).

1.2.2 Influence of land cover configuration

The size of green areas (parks, as an example) influences their cooling impact too, but even small green spaces (≈ 0.5 ha) can have a positive effect on microclimate, reducing temperatures by 1°C - 3°C and increasing air humidity by 2% - 8%. However, different studies show that the minimum size required for obtaining a positive effect depends on the features of the green space itself and on the background climate (Monteiro et al. 2016; Oliveira et al. 2011; Chang et al. 2007; Feyisa et al. 2014). Besides land cover composition (abundance and variety of land cover features, regardless their spatial arrangement), also its configuration (spatial arrangement or distribution of land cover features) is relevant and contributes to increase the cooling effect generated by vegetation, even if the effect of configuration is lower with respect to the one of composition.

Keeping a fixed composition of land cover features, the most impacting configuration parameters are the edge density of both coarse and fine vegetation, their shape complexity and variability and the nearest neighbour distance among woody vegetation (a parameter that describes the distribution of woody vegetation over the whole considered surface). An increase in edge density of woody and herbaceous vegetation has a positive cooling effect, reducing the land surface temperature (LST) and thus the UHI effect, as well as an increase of shape complexity and variability of woody vegetation, probably because a higher shape complexity increases the shading effect and enhances energy exchanges between artificial areas and vegetation, reducing as well the UHI. An increase of nearest neighbour distance of woody vegetation also generates a positive cooling effect, providing thus evidence that an even distribution of

green areas throughout the city area is better than a clustered one (W. Zhou et al. 2011).

The cooling effect provided by trees depends also on their leaf color and foliage density and, more generally speaking, on the plant specific thermal and optical properties (B. Lin and Y. Lin 2010). The tendency of vegetation to adapt to the environment they live in has also an impact on cooling efficiency, since, for example, plants growing in hot and dry environments have evolved to absorb less radiation, influencing thus climatic variables in a different way than plants which have grown in a colder or more humid environment. For this reason the thermal impact of different species on the environment is likely to vary (Feyisa et al. 2014).

1.3 Aim of the study

The frame of the study regards the effects of the presence of vegetation in urban environments. The aim is to analyze both positive and negative impacts of vegetation on different measurable quantities, such as concentration of pollutants, mass fluxes and wind velocity, in a long street canyon perpendicular to the wind direction. To do so, two different street configurations are treated: one without trees and one with two rows of 21 equally spaced trees. Concentration measures are taken both inside the street canyon, in order to compute the average concentration in the control volume, and on the rooftop of the canyon, to compute the exiting mass flux. Wind velocity measures are taken only on the rooftop, coupled with concentration measures, in order to compute the flux as well. All the measures are taken in both configurations and are then used to calculate the vertical mass exchange velocity u_d , in order to see if and how the presence of trees influences it. This is an important parameter because it contains information on both turbulent and mean mass exchange between street canyon and external atmosphere, and for this reason it is used to compare different urban configurations in terms of efficiency of pollutants removal.

The final general objective of all the studies on this topic is to extract from the obtained results practical advices for urban planners on how to implement

vegetation in urban environments, in such a way that it becomes useful to control the effects of climate change and pollution at pedestrian level, which can have a deep impact on human health. In fact, past studies have already proven the positive effects that green features provide against the urban heat island effect and temperature rise (see section 1.2), but they haven't dealt with accuracy the issue of mass exchange between streets and external atmosphere and how vegetation influences it. This is an important topic since a significative portion of urban pollutants is produced at ground level by vehicular emissions, and knowing how pollutants disperse along streets and how to implement vegetation in such a way to control the air exchange with the external atmosphere could reduce health issues and improve human comfort.

The last part of the work, on the other hand, is dedicated to the analysis of the time series of the vertical turbulent flux $w'c'$ at the rooftop of the canyon, on the section in the middle of the source. To do so, two different approaches have been adopted: a traditional analysis using the various moments of the time series (mean, variance, skewness and kurtosis), as well as the spectrum of the signals, and a complex network analysis on the signal, based on the concept of visibility graphs and the related metrics. Network science is in fact a quite recent and innovative approach for the analysis of various types of signals, and in the present thesis it will be applied to the field of fluidodynamic measures.

The first objective of this part is to provide a more detailed analysis of the turbulent mass exchange in the shear layer, in order to describe the main features of the phenomenon itself and see how it evolves moving downwind, as well as understanding how the presence of vegetation modifies those characteristics. The second objective is to prove that complex network analysis can be a useful tool also if applied to fluidodynamic measures, since this type of application has been done only few times in previous studies and never on flux measures. Network science can in fact be a valid alternative to traditional statistics, being able to highlight the important features of a phenomenon through several network metrics, and the aim is to demonstrate that it can be successfully applied also to complicated fluidodynamic measures.

After this first introductory Chapter, where the general frame of the study and the objectives of the thesis have been presented, Chapter 2 starts to deal

more in detail with the issue of pollutant concentrations, with a description of the methodology generally adopted for this kind of studies and the analysis of the Atmospheric Boundary Layer. In Chapter 3 a description of the experimental setup of the wind tunnel, as well as a description of the measurement instruments, is performed. Assessments of canyon alignment and wind profile parameters are described in Chapter 4; these are necessary before executing all the needed measures in order to verify that the experimental model is correctly set up, and to have a complete description of the wind characteristics under which the study is performed. Chapter 5 is dedicated to the analysis of the vertical mass exchange velocity in the two configurations. A further verification of mass conservation for the "no trees" layout is also carried out, in order to try to assess if the measurement grid is sufficiently refined, and to be sure that there are no issues with the source and the model configuration. Signal analysis of time series of velocity-concentration correlation is performed in Chapter 6, both considering traditional statistics and network-based metrics. Finally, all the results are summed up in Chapter 7, together with future perspectives on the topic, possible practical implementations of the results, and advices on how to improve and verify the obtained results.

2. Methodology, relevant phenomena and models

In the first part of this chapter, a review of the most important past studies regarding the influence of vegetation on pollutants concentration has been made, highlighting the methodology usually adopted for this type of studies. In the second part of the chapter, the main dynamics of the Atmospheric Boundary Layer (the portion of the atmosphere in which all these phenomena occur) are analyzed, providing the necessary mathematical formulations needed to understand them.

2.1 Influence of vegetation on pollutant concentrations

Considering all the studies mentioned in Chapter 1, it is clear that vegetation has a deep and positive effect on urban microclimate; however, also the consequences that it has on pollutant concentrations, which is another crucial issue of city areas, especially at pedestrian level, must be taken into account in order to have a complete view of the scenario. Pollutants at pedestrian level are mainly coming from exhausts of vehicles running into streets; once they are produced, depending on the air flow field that is present in the urban pattern, they tend to be removed in a more or less efficient way. It is thus important to see how the presence of vegetation, in particular trees, in street canyons influences the air flow field and the concentration field, both in terms of magnitude and pattern. A street canyon is a road characterized by the presence of high buildings on both its sides, which is considered to be the basic unit of the urban geometry. To solve this problem, many studies (Gromke and Ruck 2007; Gromke and Ruck

2009; Buccolieri, Gromke, et al. 2009; Buccolieri, Salim, et al. 2011) compare different street canyon configurations: the tree-less one, which is considered as the reference scenario and is also useful to understand the dominating flow phenomena inside a street canyon, and several other configurations with tree rows, changing some parameters from one scenario to the other in order to see the influence of such aspects on flow field and concentration field. The comparison between the tree-less scenario and other various scenarios with different tree configurations is in fact the most used methodology to deal with this type of study. Not only the effect of tree features is analyzed, but also the one of wind direction and street aspect ratio, in order to consider the widest possible set of configurations that may occur in reality. All these studies are performed using wind tunnel models and/or CFD simulations, where traffic emissions are modelled through a line source.

2.1.1 Reference scenario

Starting from the reference scenario, the one without any trees and with wind perpendicular to the street canyon (90°), the main characteristics of the flow field inside a urban canyon are highlighted. Two fundamental structures are identified: the central vortex (CV), in the middle part of the canyon (length) and the corner eddies (CE), at the two ends of the street. The CV is a vortex structure, with horizontal axis, that is caused by the cross-flow above roof level: air is entrained into the street canyon and flows down in front of the windward wall (B); then, during the passage from windward to leeward wall (A) (which occurs at ground level, where the flow has an opposite direction with respect to the atmospheric one), it accumulates near-ground traffic emissions.

At the end, air flows upwards in front of wall A and is partially entrained back into the atmospheric flow above the roof level (there is not a complete exchange of air between two consecutive cycles of canyon vortex). Corner eddies, on the other hand, have vertical axis and tend to bring air directly into the street canyon from the outside environment; their effect, however, is felt only up to a length of approximately 3.5 street widths (Hunter et al. 1991). Globally, there is a net air inflow from lateral surfaces (due to corner eddies) and a net air outflow

from the upper surface (due to canyon vortex).

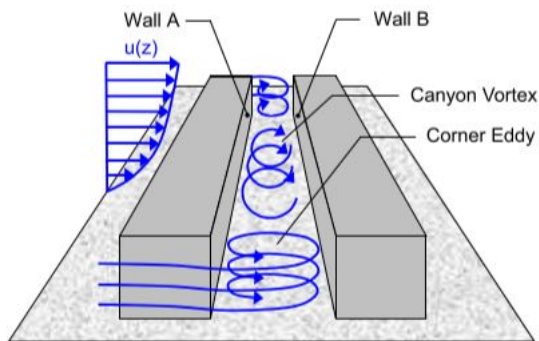


Figure 2.1: Principal flow structures inside a street canyon

With this defined flow structure, concentrations at both leeward and windward walls are measured. Results show that average concentration values at wall A are approximately 2.5 times higher than at wall B; this is mainly due to the circulation patterns inside the canyon: the CV tends to accumulate traffic emissions, bringing them towards the leeward wall before expelling them into the atmosphere.

Considering concentration patterns, for both walls the highest values are obtained in the middle of the street length, while a decrease in concentration is experienced towards street ends; this is due to the effect of corner eddies on the lateral portions of the walls, which provide additional ventilation (Gromke and Ruck 2007).

2.1.2 Effect of the presence of trees

Once the reference scenario without trees has been defined, a series of various tree arrangements has been analyzed, in order to see what is the effect of their presence on concentrations and flow field, and how different parameters impact on these two quantities. Gromke and Ruck (2007) proved that, for a street canyon characterized by $H/W=1$ and a single row of 9 m crown trees in the middle (with the same wind configuration of the reference case), pollutant concentrations increase at the edges of the leeward wall and slightly decrease at the whole windward wall, with a global increase considering both walls together. The increase at the edges of the leeward wall can be explained by the fact that tree crowns constitute obstacles and offer resistance to the air entering the canyon, reducing thus the lateral flow induced by corner eddies. The decrease at the windward wall on the other hand can be explained by the fact that

with the presence of trees the vertical velocity of wind entering the canyon in front of wall B is increased, leading thus to lower concentrations.

If there's an increase in the dimensions of tree crowns, up until the configuration where neighboring tree crowns are touching each other, the flow field is modified with reduced net air inflow from lateral surfaces, together with a reduced strength of the central canyon vortex. These effects lead to increased concentrations at the whole leeward wall and also at the edges of windward wall, because of the blocking effect of tree crowns. The height of tree trunks, on the other hand, has almost no influence on both flow field inside the canyon and pollutant concentrations, unless it causes the top of the tree crown to exceed the roof of the canyon. In that case, concentrations at wall A increase significantly, due to the reduced amount of air entrained into the canyon. Finally, tree spacing has been analyzed; an increased tree spacing leads to lower concentrations with respect to a denser tree configuration, because air flow is less hindered, as expected.

In a second study, Gromke and Ruck (2009) analyzed the effect of tree crown porosity. In fact, due to their porosity, tree crowns have unique aerodynamic properties in comparison to non-porous bodies, and these must be taken into account in order not to misestimate concentration and flow fields. Real trees are generally divided into coniferous and deciduous trees, with their crown porosities (expressed in pore volume fraction related to total crown volume [$m^3 m^{-3}$]) that roughly vary between 93% and 99% (Groß 1993; X. Zhou et al. 2002). Experimental results show that a decrease in crown porosity leads to increased average concentrations at the leeward wall and to decreased average concentrations at the windward wall, with enhanced blocking effect on corner eddies that causes an increase in local concentrations at the edges of both walls. However, once porosity drops down below a certain threshold, which was found to be 97%, a further decrease has no significant impact on concentrations at both walls. Through these studies, it is clear that there's a tight bond between vegetation, flow and concentration fields in street canyons, with a global negative effect of trees on pollutants dispersion with respect to the tree-less case.

2.1.3 Effect of street aspect ratio

Fortunately, not only vegetation has influence on concentration maps inside a street canyon. Buccolieri, Gromke, et al. (2009) showed in their study that one of the most relevant parameters is the street aspect ratio W/H . In particular, comparing the same tree configuration in two different canyons, one with $W/H=1$ and the other with $W/H=2$, it is clear that the negative role on pollutant dispersion played by vegetation is much less marked when the aspect ratio increases. This result can be attributed to the fact that with reduced W/H ratio there's less ventilation and thus reduced dispersion and dilution: as a measure of this, the global flowrate through the street roof and lateral surfaces was found to be reduced by 33% with respect to the tree-less case in the $W/H=2$ case, while the reduction was much more significant (62%) in the $W/H=1$ case. For this reason it would be advisable to prefer wider streets with maybe two rows of trees rather than narrow streets with a single row of trees.

Further studies on the effect of different aspect ratios have been performed by Fellini et al. (2020), in particular regarding smaller aspect ratios (narrower streets or higher walls). When the W/H ratio falls below a critical value, which is seen to be $2/3$, there's the formation of a second counter-rotating cell in the middle of the street canyon, below the main one, due to an excess of vorticity that accumulates at the bottom of the canyon as the aspect ratio becomes smaller. Roughness of downwind canyon wall also contributes to the generation of this second rotating cell, increasing the threshold of W/H ratio at which the phenomenon begins. The same effect occurs when the downwind wall is heated, but only if the aspect ratio is already below 1, otherwise thermal fluxes would not be strong enough to modify the topology of mean flow streamlines, and their effect would increase the intensity of turbulent kinetic energy, with consequent acceleration of wash-out process from the canyon and reduced concentrations within it (positive effect). The second cell that may appear is relevant because it has a negative effect on concentrations at pedestrian level. It inhibits the transfer of pollutants from street level to the external flow (thanks to a slow vertical transport between the lower and the upper cell); concentration maps are also different with respect to the single cell case, because the highest

concentration at pedestrian level is no more experienced at the leeward wall but at the windward wall, due to the presence of the counter-rotating lower cell that tends to entrain traffic emissions towards it.

2.1.4 Effect of wind direction

Also atmospherical conditions have their importance in this study, in particular wind direction. Past investigations (Vardoulakis et al. 2003; Ahmad et al. 2005) have shown that the perpendicular configuration (wind blowing at 90° with respect to the street canyon axis) leads to the largest in-canyon pollutant concentrations, thanks to the recirculating flow that confines the transport of pollutants, as the previous mentioned studies also confirmed. However, when wind direction changes, also concentration and flow fields change; Buccolieri, Salim, et al. (2011) showed that for the 45° inclined case the structure of the canyon vortices analyzed earlier is not so pronounced and is characterized by a superposition of canyon vortex and corner eddies. In this case, measurements of concentrations reveal that the negative effect of trees on dilution and dispersion are much less pronounced than in the 90° scenario. Moreover, the positive effect generated by an increase of the aspect ratio W/H is enhanced in the 45° case with respect to the 90° one, leading to a much higher reduction of average concentrations. In general, if wind direction changes from a perpendicular direction to a parallel one, the effect is a progressive reduction and superposition of canyon vortices and corner eddies, and the principal pollutant transport mechanism becomes the flow along the street axis, with consequent higher concentrations towards the downstream ends of the street. It is thus important for city planners to know in advance which are the main wind directions experienced in a city over the whole year, in such a way that it is possible to make the best decisions in terms of street planning.

2.1.5 Particles deposition on vegetation

Besides the impact that vegetation (and in particular trees) has on air exchange mechanisms inside a street canyon, and thus on pollutant dilution and dispersion, there's another effect that is relevant and has to be considered in the analysis: it is the phenomenon of pollutant deposition on vegetation, which acts as a sink for particles dispersed in the air. It is a positive effect that can counter-balance to some extent the negative effect generally produced by vegetation on pollutant dispersion. However, even if under a qualitative point of view the filtration effect is not disputable, under a quantitative point of view its ability to reduce particle concentrations is limited, because of the reduction of air exchange in the canyon and the natural emission of plants themselves. In fact, pollen emitted by plants can reach concentration levels up to $14 \mu m^{-3}$ in particular conditions; moreover, plants also contribute to particle generation with the emission of biogenic organic volatile compounds (BVOCs), which then condensate in the atmosphere (Litschke and Kuttler 2008). The main characteristics that influence particle deposition on vegetation are the deposition surface area (the larger the better) and the porosity: in fact plants have to be porous enough to let wind stream flow through their canopy, and not above or below it, in order to be effective in capturing air pollutants. Plants have a much larger surface area per unit of volume with respect to human-built structures, and that's the main reason why they are more efficient in removing particles through deposition (Janhäll 2015); 10 to 30 times faster deposition has been reported for sub-micrometre particles on synthetic grass compared with glass and cement surfaces (Roupsard et al. 2013).

Deposition is usually taken into account through the deposition velocity, which is the ratio of mass particle flow rate (F_p in $\mu g s^{-1} m^{-2}$) towards the leaf surface and the atmospheric particle concentration (C_p in $\mu g s^{-1} m^{-3}$), and is usually expressed in $cm s^{-1}$:

$$v_d = \frac{F_p}{C_p} \quad (2.1)$$

However, the description of the deposition phenomenon is often simplified

as a one-dimensional vertical deposition on a homogeneous layer of vegetation, and deposition velocities are usually calculated through empirical formulations or using wind tunnel measures. Moreover, since deposition velocity is influenced by various parameters (species and features of the involved plants, size of the particles, air humidity, wind speed and distance of vegetation from emission sources), differences arise among performed studies, but also between studies and reality (Litschke and Kuttler 2008; Petroff et al. 2008), depending on the complexity of the measurements.

Diameter and size of particles influence the main mechanism that drives deposition: for particles with $d_p > 10 \mu m$ sedimentation is the main deposition process; as particle size reduces, sedimentation becomes less effective because the mass of the particle and thus the acceleration due to gravity become smaller and smaller. Sedimentation is relevant until the size of $d_p = 1 \mu m$; between $1 \mu m$ and $0.1 \mu m$ deposition is mainly driven by impaction and interception: when air flows around obstacles, the path of the particle can either be too close to the obstacle (interception) or curved in such a way that the particle directly collides with the obstacle thanks to its inertia (impaction) (Lee and Ramamurthi 1993). Below $d_p = 0.1 \mu m$ interception and impaction become not so relevant in driving deposition, but measurements still sense a high deposition rate even with very small particles; this is due to diffusion processes. In fact, near the surfaces, particles are continuously deposited thanks to Brownian motion, which induces a concentration gradient that produces a mass flow towards the surface.

Air humidity also has a deep impact on deposition; this is due to the fact that particles are mainly hygroscopic and for this reason they change their size according to the absorption or discharge of water (Winkler 1988). If particle size changes, then also deposition processes change, as seen previously. Particle size increase is expressed through an exponential function of relative humidity (it increases by a factor 1.1 at 60% r.h., by a factor 1.2 at 80% r.h. and by a factor 1.7 near to saturation), and it also depends on the hygroscopicity of the considered aerosol; in fact, there are slight differences between urban and rural aerosol properties.

The effect of wind speed on particle deposition is strongly dependent by the influence that vegetation itself has on the air exchange. Beckett et al. (2000), through a wind tunnel study with NaCl, showed that a greater wind speed causes a higher deposition velocity, as particle inertia is enhanced, and this generates a more effective impaction. At the same time though, as already mentioned, one of the main effects produced by vegetation is the reduction of the near-surface air exchange, which is also proven to reduce wind speed, and this fact contributes to a reduction of the mass deposition flow. Globally thus, the role of vegetation as an obstacle to air flow has a dual negative effect: not only it reduces air exchange and replacement, but it also reduces the positive effect of particle deposition due to the reduced wind speed conditions near plant surfaces. The analytical definition of deposition velocity (equation 2.1), if converted, shows that the mass flow to a surface (supposing a constant deposition velocity) increases with increased concentration of particles:

$$F_p = v_d \cdot C_p \quad (2.2)$$

For this reason, vegetation should be planted as near as possible to the emission source, in such a way that filtration efficiency is maximized, but trying to limit the air exchange reduction to the minimum.

Another important aspect that must be taken into account is the fact that not all tree species have the same filtration efficiency; the spatial structure of branches and twigs and the shape of leaves and needles are key properties that influence the filtration capacity of a plant. In this sense, wind tunnel tests (Beckett et al. 2000) and experimental measures (Przybysz et al. 2014) have shown that particle deposition is higher on conifers (such as pines and cypresses) rather than on deciduous trees (poplar and maple for example), thanks to their aerodynamic properties, small needles and to the higher complexity of their structure. The difference between the two types of vegetation ranges between 65% and 320%, depending on the environmental conditions in which plants are placed. Moreover, deciduous trees lose their foliage cover during winter months, reducing dramatically their filtration efficiency in those periods; on the other hand, conifers keep their foliage for the whole year, resulting in a

higher total amount of particles removed from the air. However, this greater amount of pollutant deposited on conifers may result in more severe physiological damage to the plants themselves (Godzik et al. 1979). For this reason, evergreen plants should be planted where the concentration of pollutant is not at its maximum, in order to avoid an excessive poisoning. Besides this poor resistance to high pollutant levels, there are also technical problems in planting conifers in street canyons, such as the need to ensure adequate drive-through heights (the branch-free portion of the tree must be high enough to let cars pass) and the reduced solar access for people at ground level during winter. For these reasons, despite their filtration efficiency is lower, deciduous trees rather than conifers are the most common plants installed in urban street canyons (Litschke and Kuttler 2008).

2.1.6 Wash-out process

Once particles have been captured by plants, rain is the main phenomenon that leads to their removal from leaves. This fact is important in order to determine the total amount of PM deposition during a certain period, especially in regions characterized by heavy rainfall. Measurements on different plant species showed that up to 60% of the deposited particles are removed by rain, while the remaining 40% is trapped into the leaves' wax and cannot be washed out so easily (Popek et al. 2013). The surface of the ground below the vegetation should also be designed in such a way that it enhances the immobilisation of pollutants, once they have been washed out, in order to prevent their further re-suspension. Rural areas, where the surface below plants is mostly open soil covered with vegetation, face thus less re-suspension because PMs are trapped by the ground vegetation, while in urban areas, where the surfaces below plants are usually paved, pollutants are much more likely to be re-suspended. Among all deposited particles, the largest ones (10 – 100 μm) are those that are more easily removed (75%-87%), while the finest particles (0.2 – 0.5 μm) seem to adhere most strongly to the foliage (2%-5% of the total removed particles) (Przybysz et al. 2014). This is a positive effect for human health, since fine PMs are more dangerous than large PMs.

At the end of this analysis, vegetation shows both positive and negative effects on urban microclimate and air quality. Surface properties such as high albedo, high reflectivity and low thermal inertia of vegetation elements contribute to a reduction of the Urban Heat Island effect. Moreover, natural features tend also to absorb thermal energy through the evapotranspiration process, and offer a better shadowing effect with respect to human buildings. On the other hand, considering the effect on pollutant concentrations at pedestrian level, vegetation (trees in particular) is an obstacle to the air flowrate entering/exiting the street canyons, leading to higher pollutant concentrations. This effect is slightly counterbalanced by the deposition phenomenon, which is higher on vegetation than on human buildings thanks to the high porosity and high deposition surface area of natural features.

In the present thesis, turbulent transport of mass between the inner area of a street canyon and the outer atmosphere has been analyzed, focusing on the influence of trees on its magnitude. Studies on this topic, as well as further studies on the effect of vegetation on air flow and pollutant concentrations, are needed in order to fully comprehend how to implement natural features in the urban pattern, so that drawbacks are limited and a better air quality is achieved.

To do so, since all these processes take place in the Atmospheric Boundary Layer (ABL), a further analysis of its properties, wind profile and dispersion mechanisms is performed, together with a focus on flow and dispersion within urban canopies.

2.2 The Atmospheric Boundary Layer

The ABL is the region of the lower atmosphere that is directly influenced by the presence of the Earth. Its structure is mainly governed by physical and thermal properties, such as humidity and temperature, because these influence deeply the atmospheric stability, which is the main responsible of ABL modifications. The Atmospheric Boundary Layer is characterized by vertical turbulent exchanges of mass, momentum and heat; these exchanges are driven by vertical wind and thermal effects (surface heating) and are mainly convective fluxes,

even if in the very small layer directly above the Earth's surface diffusive phenomena are the most relevant.

When there's a stable atmosphere, the cooling of ground surface at night causes a compression of the ABL, with reduced vertical dispersion, while when there's an unstable atmosphere, which can be caused by ground surface heating during the day, there's a vertical expansion of the ABL thanks to the enhanced convective motions. It is clear thus that meteorological conditions heavily influence the depth of the Atmospheric Boundary Layer, in particular cloudiness and wind: the first one limits the amount of solar radiation reaching the ground during the day, as well as reducing the ground surface cooling at night; the second one is the key parameter that allows the various layers of the ABL to mix, in order to reduce temperature trends inside it.

2.2.1 Spatial scales

When considering the issue of pollutant dispersion in urban areas, spatial (and temporal) modelling scales are very important in the analysis, since different scales mean different parameters that influence dispersion. For example, when working with a small spatial and temporal scale, meteorological conditions can be taken as stationary, while this simplification is not possible when dealing with a large (either spatial or temporal) scale; this fact obviously has a deep impact on the complexity of the analysis. Usually, four are the different spatial scales that are adopted:

- **Regional scale:** in this scale, phenomena produced at city scale (such as the UHI effect) have the deepest impact. Cities are represented as areas characterised by a homogeneous roughness, higher than the one of the surrounding regions, and not described in their complexity. When dealing with a regional scale, the ABL is divided into three zones: an inertial zone, where the boundary layer adapts to the influence of the urban canopy, an intermediate zone where thermal effects start to be felt, and an upper level;
- **City scale:** when considering this scale, the complexity of the geometrical layout of buildings is not negligible anymore, since it affects mean

wind direction and turbulent fluctuations, which are the main responsibilities for pollutant dispersion. Besides inertial and outer regions, a further distinction is made between *urban canopy* and *roughness sub-layer*. In urban canopy recirculating regions are formed due to the influence of buildings layout on the airflow, while in roughness sub-layer the airflow is influenced by wakes generated by buildings;

- **Neighborhood scale:** it is a further extension of the city scale, where the flow analysis reaches a higher level of detail (making distinctions between neighborhoods for example), but still buildings are described with a statistical approach;
- **Local scale:** it is the scale characterized by the highest level of detail, for example a street canyon; all geometrical parameters (such as H/W ratio or L/W ratio) become fundamental in the analysis, as well as wind direction.

2.2.2 Wind profile in the Atmospheric Boundary Layer

As already mentioned, all the fluxes that characterize the Atmospheric Boundary Layer are turbulent fluxes (momentum, thermal energy), which can be described as random fluxes; for this reason, it is not possible to use a deterministic approach to establish the properties of the flow. Usually, a decomposition of variables into a mean part and a fluctuating part is performed, in such a way that the governing equation becomes a set of governing equations. This is easier to manage, but still it is necessary the use of similarity theory, because the number of unknowns is higher than the number of equations.

When thermal effects are negligible (neutral boundary layer), the profile of the mean flow in a lower region of the ABL (the inertial layer), can be described with the logarithmic law:

$$U(z) = \frac{u_*}{k} \ln \left(\frac{z - d}{z_0} \right) \quad (2.3)$$

Where:

u_* is the surface friction velocity, that expresses shear stresses under the form of a velocity so that they are comparable with flow velocity;

z_0 is the roughness length, which is the height in the ABL at which the wind speed theoretically becomes zero;

d is the zero-plane displacement, which represents the vertical displacement of the horizontal plane where wind velocity is assumed to be zero. The displacement is due to the presence of obstacles and is usually considered when dealing with a city (or lower) scale;

k is the von Karman constant, whose universal value is 0.4.

This logarithmic law can be derived using different approaches but keeping however two essential hypotheses:

- i. The flow is considered homogeneous on horizontal planes, i.e. the only length influencing the wind velocity is the distance from the wall;
- ii. The fluctuating velocity field has only one velocity scale, to which all velocity components are proportional.

Given these assumptions the following approaches can be adopted to obtain the log law:

- In the region where Reynolds stresses are almost constant with respect to mean velocity, tangential stresses are defined as a function of mean velocity gradient through the kinematic eddy viscosity ν_t . This quantity is itself defined as the product of a velocity, representing turbulent intensity (u_*), and a length scale, representing the size of turbulent structures (z), through the von Karman constant as a proportionality constant.

$$-\overline{\rho u'w'} = \rho u_*^2 = \text{const} \quad (2.4)$$

$$\begin{cases} u_*^2 = \nu_t \frac{dU}{dz} \\ \nu_t = \sigma_u l = u_* z k \end{cases} \quad (2.5)$$

By substituting, we obtain Equation (2.6), which, when integrated, provides the logarithmic wind profile:

$$u_* = kz \frac{dU}{dz} \quad (2.6)$$

- Define an intermediate region, called a "buffer region", where flow dynamics depend on structures that are big enough not to be influenced by roughness length and, at the same time, small enough not to be influenced by boundary layer depth. In this region, both wind profiles describing the inner and the outer region of the ABL must be valid and, to connect the solutions, an asymptotic matching is applied, defining specific limit conditions for both cases. This happens only if the wind profile is expressed through a logarithmic form, hence obtaining the desired function.
- Make a turbulent kinetic energy balance in a region close to the wall where the assumptions of nearly constant total shear stresses and concentrated mean velocity variations are valid. Considering a 2D steady flow, thus neglecting all time derivatives and every variable over y-direction, and neglecting molecular viscous transport and buoyancy flux, the obtained equation is:

$$u \frac{\partial q^2}{\partial x} + w \frac{\partial q^2}{\partial z} = -\frac{\partial \overline{wp}}{\partial z} - \frac{\partial \frac{\overline{wq^2}}{2}}{\partial z} - \overline{u'w'} \frac{\partial u}{\partial z} - \epsilon \quad (2.7)$$

where ϵ expresses dissipation. Considering the hypothesis previously made, production and dissipation become much more important than flux terms; thus the equation becomes:

$$\overline{u'w'} \frac{\partial u}{\partial z} + \epsilon = 0 \quad (2.8)$$

By the definition of $\epsilon = \frac{u_*^3}{kz}$ and reminding that $\overline{u'w'} = -u_*^2$ the final equation is equation 2.6, which gives the logarithmic wind profile when integrated.

This discussion is valid under the assumption of neutral boundary layer, where thermal fluxes are supposed to be negligible with respect to mechanical

production of turbulent kinetic energy. However, in reality, this is not always true: thermal fluxes may be present and their influence is relevant, because they cause significant variations in the depth of the boundary layer during the day. For this reason, Monin and Obukhov (1954) extended the similarity theory in order to consider also thermal fluxes. They introduced a new length scale, the Monin-Obukhov length η , that represents the distance from the wall at which the thermal production of turbulent kinetic energy is equal to the mechanic production. In this way, the ABL can be described considering only two portions:

- Above the Monin-Obukhov length a distinction between stable and unstable atmosphere must be made. If the atmosphere is stable, turbulent motions are reduced and the depth of the boundary layer δ is supposed to be exactly the Monin-Obukhov length η . If the atmosphere is unstable, the depth of the boundary layer is much higher than η and its dynamics do not depend anymore on the velocity and length scales of friction velocity and roughness length. When the ratio $\frac{\delta}{\eta}$ is large enough, all flow curves collapse into universal curves which have δ as characteristic length scale and the convective velocity $u_c = \left(\delta g \frac{\langle w \Delta \Theta \rangle}{\Theta} \right)^{\frac{1}{3}}$, where Θ is the potential temperature, as characteristic velocity scale;
- Under the Monin-Obukhov length, the characteristic length becomes η itself; the vertical variation of mean wind velocity becomes:

$$\frac{kz}{u_*} \frac{dU}{dz} = \Phi \left(\frac{z}{\eta} \right)$$

Where the function $\Phi \left(\frac{z}{\eta} \right)$ changes depending on the stability of the atmosphere.

2.2.3 Dispersion in the Atmospheric Boundary Layer

In the atmospheric boundary layer, the equation that theoretically describes the evolution in space and time of the concentration of a passive scalar is the

advection-diffusion equation, which comes from the mass conservation of pollutants:

$$\frac{\partial c}{\partial t} = -\frac{\partial}{\partial x_j} \left(u_j c - D_m \frac{\partial c}{\partial x_j} \right) \quad (2.9)$$

where D_m is the molecular diffusion coefficient. By neglecting molecular diffusion and applying the Reynolds average operator the final equation becomes:

$$\frac{\partial \bar{c}}{\partial t} = -\frac{\partial}{\partial x_j} (\overline{u'_j c'} + \bar{u}_j \bar{c}) \quad (2.10)$$

where \bar{c} is the mean scalar concentration and $\overline{u'_j c'}$ is the turbulent flux of passive scalar. The equation can be solved only by considering the analogy, pointed out by Boussinesq (1897), between the impact on instantaneous concentrations of thermal motion of molecules and the impact on averaged concentration \bar{c} of turbulent flux $\overline{u'_j c'}$. This allows to consider turbulent fluxes as molecular fluxes, using Fick's law:

$$\overline{u'_j c'} = -K_{ji} \frac{\partial \bar{c}}{\partial x_i} \quad (2.11)$$

Where K_{ij} is the turbulent diffusion tensor. In this way, equation 2.10 becomes:

$$\frac{\partial \bar{c}}{\partial t} = -\frac{\partial}{\partial x_j} \left(-K_{ji} \frac{\partial \bar{c}}{\partial x_i} + \bar{u}_j \bar{c} \right) \quad (2.12)$$

This equation can be analytically or numerically solved, depending on the typology of the conditions imposed at the boundaries. One of the most famous solutions, for the idealized case of a point source in a uniform mean wind field (directed along the x axis) and a homogeneous and isotropic turbulent flow, is the Gaussian gaussian plume model:

$$\bar{c}(x, y, z) = \frac{\dot{M}_q}{2\pi\sigma_y\sigma_z\bar{u}} \exp\left(-\frac{y^2}{2\sigma_y^2}\right) \exp\left(-\frac{z^2}{2\sigma_z^2}\right) \quad (2.13)$$

Where the relation between standard deviations and turbulent diffusion is $\sigma_z = (2K_{zz}t)^{\frac{1}{2}}$ and $\sigma_y = (2K_{yy}t)^{\frac{1}{2}}$. This solution can be conveniently adapted for

the cases of non-uniform wind and inhomogeneous and anisotropic turbulence (Soulhac et al. 2011). The hypothesis that must be verified for this solution to be considered valid are:

- Stationary flow (in statistical terms);
- Constant and diagonal turbulent diffusion tensor;
- Turbulent flux in streamwise direction that is negligible with respect to flux of mean motion ($\overline{uc} \gg \overline{u'c'}$);
- Homogeneous flow and uniform velocity \bar{u} .

This solution is valid when the flow is not disturbed by obstacles; it is usually applied to describe the dispersion of plumes that are emitted at heights above 100 m and surrounded by flat lands, so that the flow is not obstructed. In fact, if applied to a urban canopy scenario, the presence of the complex geometry of buildings and roads would lead to the invalidation of the hypothesis that are at the base of the model.

2.2.4 *Urban canopy flow*

When the analysis is made at a reduced scale, such as the local one, the description of the geometry of buildings becomes crucial, because they deeply affect the flow regime and, consequently, the dispersion of pollutants.

Starting from a single obstacle absorbed in the wind flow, different flow zones can be identified (figure 2.2):

- Undisturbed flow zone: it is the region before the building that is almost not modified by the presence of the building itself, where the logarithmic wind profile still remains valid;
- Displacement flow zone: it is the region where air encounters the obstacle. Air flow can be deflected around the sides, over the top or down the front the obstacle and, if there is separation of the flow from the surface of the obstacle, pressure drops, suction phenomena and small reverse flow may happen on the surface;

- Cavity flow zone: it is the region downwind the obstacle, where the pressure drop generates a circular motion of wind, in the form of a double eddy;
- Wake flow zone: it is the region downwind the obstacle, where its presence is not felt anymore and the logarithmic wind profile is re-established.

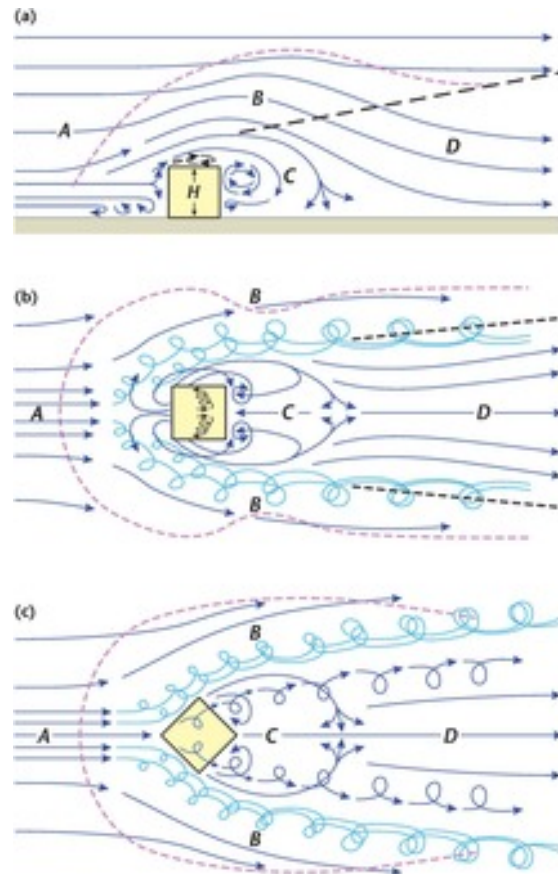


Figure 2.2: Flow zones around a single building: undisturbed flow (A), displacement flow (B), cavity zone (C), wake flow (D)

When the discussion comes to multiple obstacles, things change because the most important parameter that must be considered is the "height-to-width ratio" (H/W). According to its value, it is possible to distinguish three different flow regimes (figure 2.3):

- Isolated roughness flow, for $H/W < 0.3$: obstacles far enough to allow the re-establishment of the original flow conditions between them. Each obstacle witnesses a recirculation zone (as the one described previously) in its own downwind region, where pollutants tend to be trapped;
- Wake interference flow, for $0.3 < H/W < 0.65$: obstacles are close enough to allow the overlapping of wake structures, generating thus a complex flow field;
- Skimming flow, for $H/W > 0.65$: obstacles are so close that there's the formation of a single recirculation vortex inside the canyon; the interference between the inner and the outer flows is reduced and takes place only at the interface (upper roof of the canyon) between the flows.

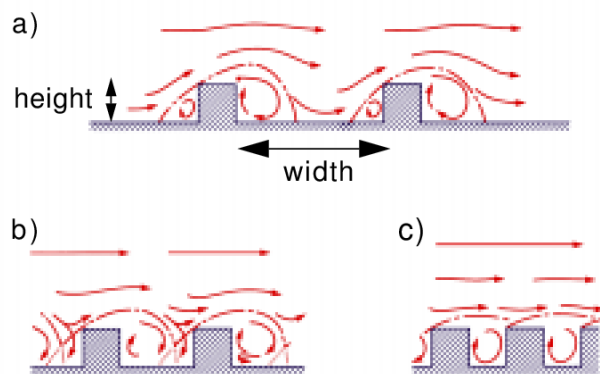


Figure 2.3: Flow regimes around multiple buildings: isolated roughness (a), wake interference flow (b), skimming flow (c)

2.2.5 Dispersion in the urban canopy

Pollutant dispersion in the urban canopy is heavily influenced by the effects of urban geometry on the flow field, such as the wake diffusion generated by buildings and the presence of a shear layer at the top of the canopy. These effects may lead to complications when modelling the atmospheric boundary layer, in particular in the characterization of the built region and the mass exchange with the external air flow.

Usually, dispersion problems within urban canopies are solved using either numerical models, parametric models or laboratory experiments. Numerical models are the most complete and, for this reason, demanding models; they solve flow and dispersion equations, using Lagrangian or Eulerian approach, with any boundary condition. There are two different families of numerical models:

- Models solving directly the Navier-Stokes equations for the whole flow or for a part of it, which are the most demanding models;
- Models solving the Reynolds-averaged Navier-Stokes equations, which are less demanding and, for this reason, they are the most employed models for urban dispersion problems.

Parametric models are less complex and less demanding than numerical models because they describe urban networks in a simplified way. They evaluate mass exchange in single streets and then join the analysis for different streets, summing their contributions, in order to get the complete model of the canopy. This is the most employed method when dealing with pollutant dispersion in a urban region, since the use of CFD numerical models requires a too high computational cost and time (due to the need of an accurate geometrical representation of the reality). The equation that is solved for every street is the following:

$$Q_{street} + Q_{in} - u_d LW \langle C(x, y, z) \rangle - u_s HW \langle C(x, y, z) \rangle = 0 \quad (2.14)$$

Where Q_{street} is the pollutant flow produced inside the street, Q_{in} is the pollutant flow that enters the street, L , W , and H are street length, width and height respectively, $\langle C(x, y, z) \rangle$ is the average concentration inside the street, u_d is the vertical mass transfer velocity between street and external flow and u_s is the advective velocity along street axis.

Among all these variables, the ones that influence mostly the analysis are the two mass transfer velocities u_d and u_s . Various studies proved that they depend

on geometrical features of streets, external turbulence conditions and wind direction. In particular, Salizzoni, Soulhac, et al. (2009) showed that a decreasing H/W ratio (larger streets) helps increasing the external turbulence, and this leads to higher u_d . In a further study, Buccolieri, Salim, et al. (2011) proved that the increased external turbulence generated by reducing the H/W ratio results in lower wall-averaged concentrations, showing thus the link between aspect ratio, external turbulence and pollutant concentrations. In the same study, also wind direction has been analyzed, proving that it influences the flow structures inside the canyon (as already mentioned in section 2.1.4) and thus mass transfer velocities.

For this reason, the parametric model should take all these considerations into account, in order to provide a good representation of what actually happens in reality.

In this frame, the present study regards pollutant dispersion in a wide and long street canyon (no intersections, aspect ratio $W/H = 2$), inserted in a typical european urban pattern, considering two different tree configurations:

- Without trees;
- With 2 rows of 7 trees.

In particular, the effect of trees on vertical mass exchange velocity and on time series of coupled velocity and concentration measurements at the canyon rooftop is analyzed. This will help to understand the impact of trees on the dynamics of the shear layer, which is the interface between the area inside the canyon and the Atmospheric Boundary Layer above it, responsible for the interaction between the inner zone of the canyon (the recirculating vortex) and the external atmosphere.

3. Setup, measurement instruments and experimental methods

3.1 The experimental setup

All the experiments have been performed in the wind tunnel of the *Laboratoire de Mécanique des Fluides et d'Acoustique*, at the *École Centrale de Lyon*. This is a recirculating wind tunnel 7.2 m wide, 24 m long and 7.4 m high; the measurement section, however, is 3.6 m wide, 12 m long and 2 m high.

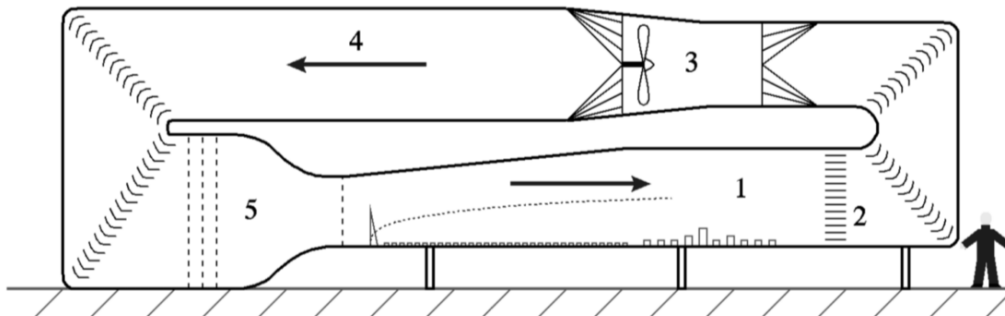


Figure 3.1: Wind tunnel at the *École Centrale de Lyon*: 1. Measurement Section; 2. Heat exchanger system; 3. Fan; 4. Diverging section; 5. Converging section and turbulence grid

As it is possible to see from figure 3.1, the fan (3) is situated above the measurement section (1) and is able to generate wind velocities from 0.5 m/s to 6 m/s; there is a diverging section (4) and a converging section with grids (5), whose aim is to generate homogeneous turbulence. There is also a heating/cooling system (2), which allows to keep a desired temperature inside the measurement section. The floor of the measurement section is a rotating panel,

which permits to change the orientation of the installed model with respect to the wind direction (represented by the black arrow in figure 3.1), in order to simulate different wind configurations if necessary. Upwind the measurement section there is also a set of 7 Irwin spires 95 cm high (Irwin 1981), necessary to produce a fully developed boundary layer along the length of the tunnel. All the instruments that are used inside the measurement section (FID, LDA, Pitot tube) are installed on a crane that moves along the length of the wind tunnel, so that measurements are possible wherever they are needed inside the tunnel.

The source is a linear source positioned on the rotating platform, 65 cm long and 1.5 cm wide, which emits ethane (C_2H_6); the choice of this specific gas as tracer is made because it is neutrally buoyant (it has almost the same molecular weight of air) and this allows to observe only advection and diffusion phenomena. The gas is emitted from a stainless steel tube equipped with needles into a mixing chamber, where it mixes with air; the mixture is then diffused to the measurement section through a grid. By changing the air/ethane ratio of the mixture it is possible to simulate different pollution levels inside the street canyon. For the present experiment, 0.5 l/min of ethane were mixed with 3.5 l/min of air, giving a global flow of 4 l/min.

The street canyon is reproduced using polystyrene blocks (10 cm high) to represent buildings. A long canyon covering the entire width of the wind tunnel was built in the center of the rotating platform. The width of the street is 20 cm, ensuring thus a W/H ratio of 2. Moreover, to represent the urban tissue of a typical European city, the whole wind tunnel measurement section has been filled with wood and polystyrene blocks (50 cm side and 10 cm high) positioned 20 cm apart along the wind direction and 10 cm apart across the wind direction, to reproduce the typical street network of European cities (figure 3.2). Every block has also been covered with a number of 5 mm high bolts, in order to represent the roughness that characterizes real life buildings, whose roof is not always flat; this also helps in the development of the boundary layer.

Two different configurations have been adopted for the present experiment: one with no trees inside the street canyon and one with two rows of 21 trees (figure 3.3); in the latter, trees have been placed at a distance of 7 cm one from the other, ensuring thus that the tree coverage extends way beyond the length of



Figure 3.2: Street network inside the wind tunnel

the source on both ends. The control volume, however, will be placed above the source and will be only 284 mm long (for both layouts), so that concentration measures do not depend on the position along the street canyon (because we are far away from the edges of the source); with this choice, only 7 trees per row out of the total 21 fall into the control volume. The model trees used are 8.5 cm high (considering crown and trunk) and 4.5 cm wide in both directions. Globally, the scale of the model is 1:200, thus referring to a real street canyon of $720 \times 40 \times 20 \text{ m}$ (length \times width \times height); with this configuration, the canyon is rather long than wide and thus the expected flow field is a bidimensional flow field.

Considering the reference system, the origin of the axes is set at the corner of the central polystyrene block, with the x axis directed along the wind direction and pointing downwind, the y axis directed across the wind direction and pointing from the right to the left and the z axis directed vertically and pointing upwards (3.3b).

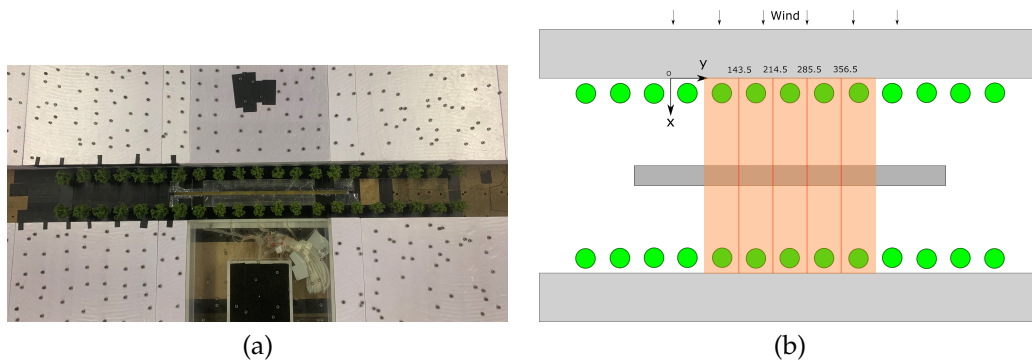


Figure 3.3: Tree configuration and reference system with control volume (in orange)

3.2 The measurement techniques

3.2.1 The Flame Ionization Detector

Concentration measurements are done using the Flame Ionization Detector (FID), an instrument that is able to detect ions formed during the combustion of organic compounds into a hydrogen flame; it is thus possible to measure concentrations of such organic compounds (for the experiment the tracer is ethane, as already mentioned) by exploiting the proportionality between the number of detected ions and the concentration itself. Ions are formed during combustion and are detected exploiting the potential difference generated between two electrodes (a positive and a negative one), which allows the formation of a current that is directly proportional to the number of ions generated.

The instrument sucks the polluted air from the measurement point and sends it to the combustion chamber by means of a thin tube 30 cm long; the tube must be as thin as possible so that it doesn't perturb the flow field, and the suction velocity has to be reasonably low for the same reason. The length of the tube, on the other hand, determines the frequency cut-off of the signal, which is 300 Hz for our case.

The raw output of the FID is a voltage signal, which is directly linked to the corresponding concentration measurement through a calibration line, whose slope has to be defined through a calibration process that has to be repeated twice a day, since the instrument (and thus the slope of the calibration line) is

very sensitive to temperature and pressure variations. Non negligible variations of these two quantities may in fact lead to errors of 10-15% in the concentration measures. Calibration is made by measuring four air-ethane mixtures, whose concentrations are known in advance (0, 500, 1000 and 5000 ppm); for every measure a voltage signal is obtained, and this allows to find the slope of the calibration line, performing a best-fit of the four measured points. However, if we are sure to work with concentrations far below 5000 ppm, it is advisable to take into account only the first three calibration points, so that the precision of the calibration is higher in the working range.

The output of each FID measure is a temporal series of instantaneous values of concentration, measured in a certain point; the FID records with a sampling frequency of 1000 Hz and the length of the temporal series has to be defined by studying the convergence of the statistics of the signal, in particular mean value and variance. For the present setup, an observation time of 120 s is chosen; figure 3.4 shows the convergence of the mean value of the signal as the observation time increases. It is clear that an observation time of 120 s is sufficiently long to reach the convergence of the mean value, while an observation time of 60 s isn't long enough to do so.

Since the wind tunnel is a recirculating wind tunnel, the tracer gas used during the experiments is recirculated too, leading to the formation of a background concentration which deeply affects the subsequent measurements (in fact the measured concentration will be the sum of the real concentration and the background one). For this reason, before and after each individual measure, the FID records the background noise by turning off the source, with a sampling time of 15 s; the background concentration is then subtracted from the measured concentration in order to get the real one. If the measured concentrations are much higher than the noise it is sufficient to subtract the mean value of the two background signals recorded, while if a more precise estimation is needed it is possible to link the two background concentrations with a line and then, for each instant in time, subtract the corresponding value of the noise from the line.

For the present experimental campaign, the Flame Ionization Detector is used both on its own (for concentration measures inside the canyon) and in

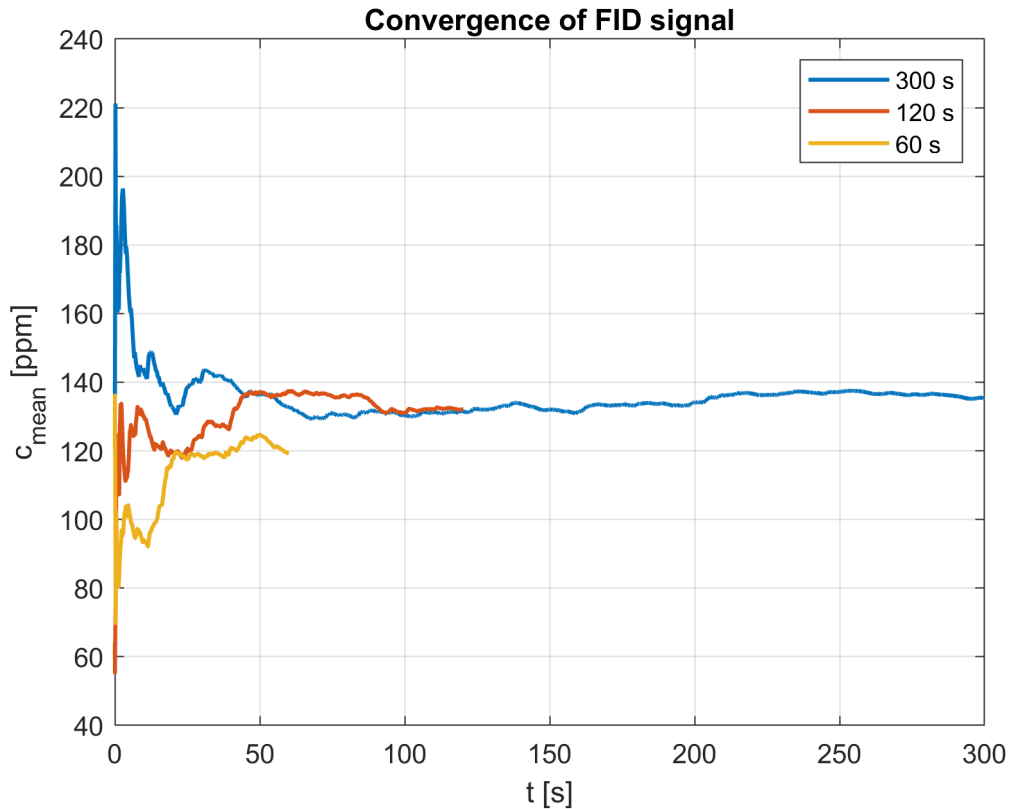


Figure 3.4: Convergence of FID measures

pair with the Laser Doppler Anemometer (for coupled measures of velocity and concentration at the roof of the canyon).

3.2.2 The Laser Doppler Anemometer

Wind velocity measurements are done using the Laser Doppler Anemometer (LDA), an instrument which exploits the use of a continuous wave laser to detect the motion of tracer particles present in the flow. The configuration of the LDA consists of two wave lasers with a beam splitter in order to generate four laser beams; optical fiber in order to transmit the beams to the probe inside the measurement section of the wind tunnel; receiving optics (photodetector and interference filter) used to detect the scattered light and convert it into an electrical signal (called "Doppler burst"); a signal conditioner and a signal processor, used to pre-process the raw data and extract from it useful information, as the

mean and fluctuating instantaneous values of velocity and other statistics.

To get flow velocity information it is necessary to send tracer particles within the flow; in fact the particles are able to scatter light proportionally to the local light intensity; this scattered light contains the so called "Doppler frequency", which is proportional to the velocity component perpendicular to the bisector of the two laser beams. The scattered light is thus collected by the photodetector, filtered from the noise of ambient light and other wavelengths and converted into an electric signal, which is then sent to the signal conditioner and signal processor.

Each couple of laser beams is able to measure one component of the velocity vector; one probe can only measure two of the three components, so in order to get complete information about the velocity vector in a certain point it is necessary to use either two appropriately tilted probes (in this case it is possible to measure all three components at the same time) or one probe and a mirror to reflect the laser beams (in this case two separate measurements are needed, one for the first two components and one for the third one, after appropriate reflection of the laser beam). For the sake of the present experiments, only two components of velocity are needed (since the flow within the wind tunnel is bidimensional and no border effects are expected due to the presence of a long canyon), so one measure with one probe and four beams is sufficient.

Seeding particles are needed especially for gaseous flows, as liquid flows usually contain enough natural seeding; it is important that the machine that produces the seeding (usually a smoke machine) does not perturb the flow field; it is also important not to saturate the measurement section with seeding particles, otherwise the LDA becomes less responsive to the seeding itself (and also the mirror for laser reflection gets dirty, if it is used).

The need of seeding particles introduces the main difference, in terms of sampling, between the LDA and the FID (but also the Hot Wire Anemometer, which is an alternative instrument to measure flow velocity used for previous works at the LMFA), which is the non-constant sampling frequency; in fact velocity is measured only when particles pass through the control volume and scatter light, but since particles follow the flow it is not possible to force them to transit with constant frequency in the measurement point. For this reason every

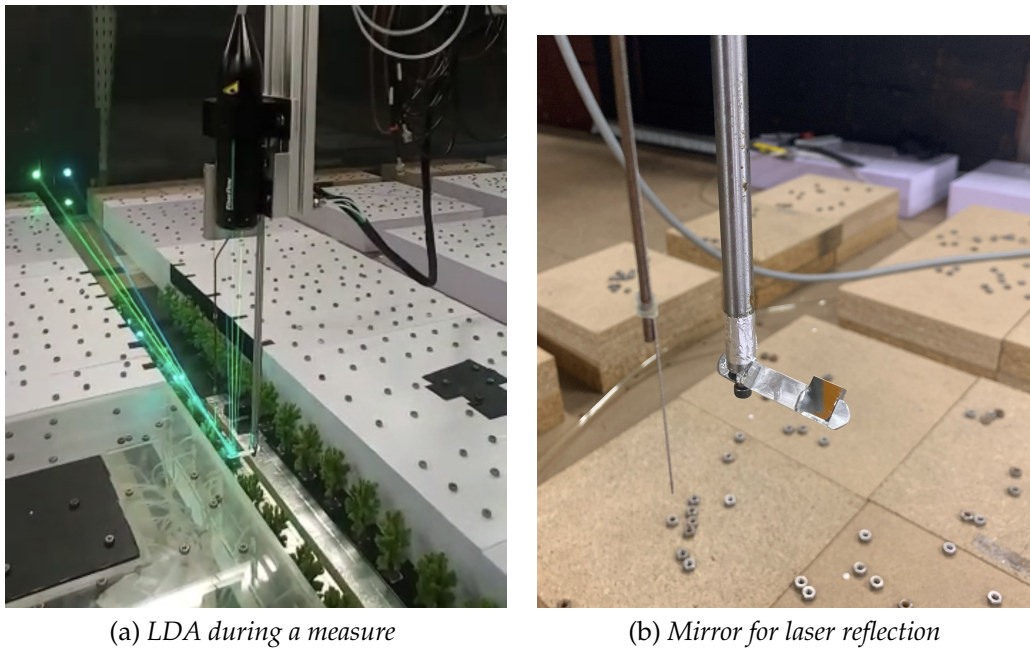


Figure 3.5: LDA images

recorded instantaneous measure is coupled with its own transit time, which is the Δt that corresponds to that specific measure, and this transit time is needed as a weight when computing all the statistics of the velocity field (mean value, variance etc.). Talking about convergence of the measures, when using the LDA it is necessary not to control the measurement time but the amount of particles transited within the control volume, since the record is done only when particles transit; by analyzing a long signal, taken with 500000 validated particles, it is possible to see that good convergence is reached after 350000 samples (figure 3.6); this number is thus set as the target for all the measures, ensuring good accuracy and not too long measure time.

One main advantage of the LDA is the fact that it doesn't need to be calibrated every time it is used (as the FID does); it is only necessary every now and then to check the alignment of the laser beams (especially if a mirror is used to reflect them, as in our case) and their focus, so that they are sensitive enough to detect all the particles that flow through the control volume.

For the present experimental campaign, the Laser Doppler Anemometer is used both on its own (to define the wind profile and its characteristics in the

wind tunnel) and coupled with the FID. For this last case, it is necessary to clarify that the seeding particles do not interfere with the concentration measurements performed by the FID, as it has been proven that the presence of seeding particles introduce only rare spikes in the concentration time series (which are not present without seeding particles), and this does not have high influence on the statistics, as the uncertainty introduced in the measures remains below 5% (Marro et al. 2020).

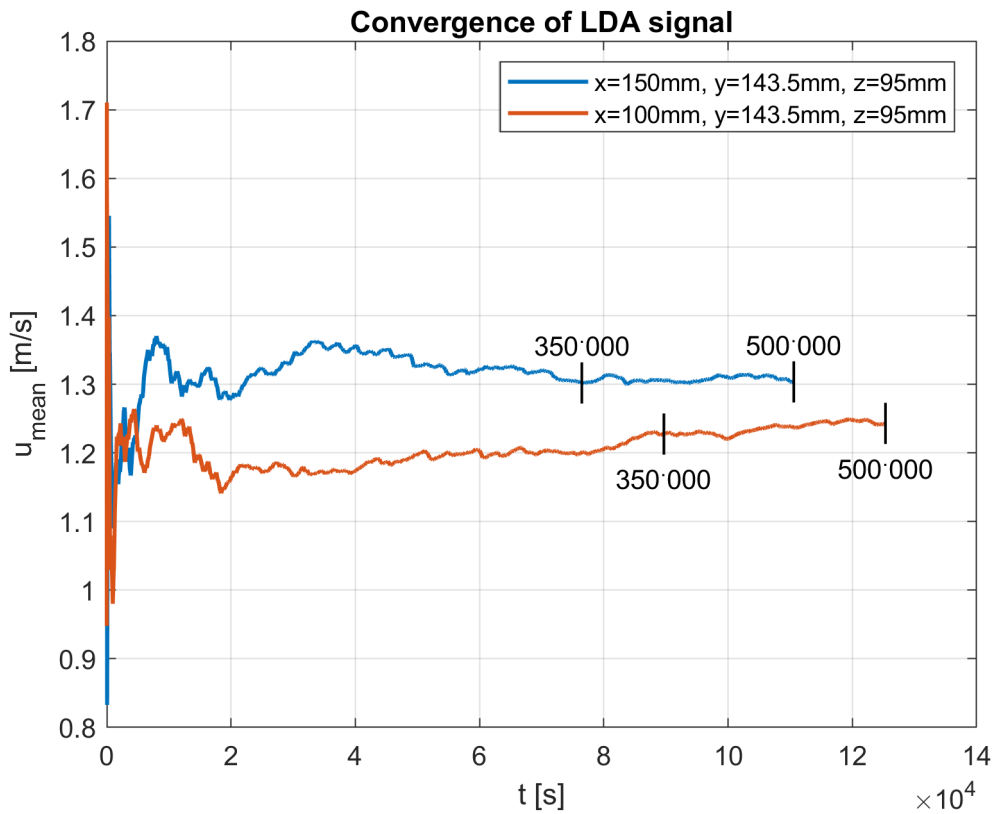


Figure 3.6: Convergence of LDA measures. The blue and red lines represent two different measurement points, while the two numbers (350 000 and 500 000) represent the number of particles recorded by the LDA at the corresponding time instant on the x-axis. It is clear thus that the convergence should be based on the number of transited particles rather than on the sampling time.

3.2.3 The Pitot tube

The Pitot tube is a much less advanced instrument with respect to the LDA, and inside the wind tunnel is used for the characterization of the wind profile in the upper part of the tunnel itself, where it is complicated both to have seeding particles for the LDA and to set the laser beams in the correct position (due to the limited movement of the crane where the probe is installed). The characterization of the upper portion of the wind profile, however, is needed in order to see the height of the boundary layer, and for this reason the Pitot tube comes in handy.

The Pitot tube is inserted along the flow, pointing into it, and it measures the total pressure p_{tot} (also called "stagnation pressure") given by the sum of static pressure and dynamic pressure (given by the movement of the fluid, in this case air):

$$p_{tot} = p_s + \frac{1}{2}\rho u^2 \quad (3.1)$$

Once the static pressure p_s is measured too, it is possible to recover the value of the dynamic pressure $\frac{1}{2}\rho u^2$ and thus the value of the instantaneous velocity:

$$u = \sqrt{\frac{2(p_{tot} - p_s)}{\rho}} \quad (3.2)$$

4. Canyon alignment and wind profile in the tunnel

4.1 Canyon alignment

The first thing that has been done before starting all the measures is a verification of the alignment of the street canyon with respect to the wind direction. The aim is to reproduce a long street that is perpendicular to the wind direction, in order to obtain a 2D configuration in the middle portion of the street, above the source. To verify the alignment, three different concentration profiles along y (at fixed x and z values) have been measured with the FID, as well as four full-section concentration maps in the central part of the canyon; figure 4.1 shows the three different normalized concentration profiles, together with the mean normalized concentration profile (average of the three measured ones) and with the four points representing the average normalized concentration for each of the four full measured sections.

Normalization has been performed by multiplying concentration values by the free-stream velocity u_∞ (the wind velocity at the top of the boundary layer, which is set to 5.3 m/s for all the experiments of this campaign), by a characteristic length (the length of the source, 0.65 m) and by δ , the height of the boundary layer (which is now assumed to be $\delta = 1.1$ m from previous experimental campaigns made in the same wind tunnel; this value will be checked later on, when the wind profile will be measured) and dividing everything by the ethane volumetric flowrate of the source.

From the graph it is possible to see that above the source (which is situated between $y = -75$ mm and $y = 575$ mm) all concentration profiles are almost

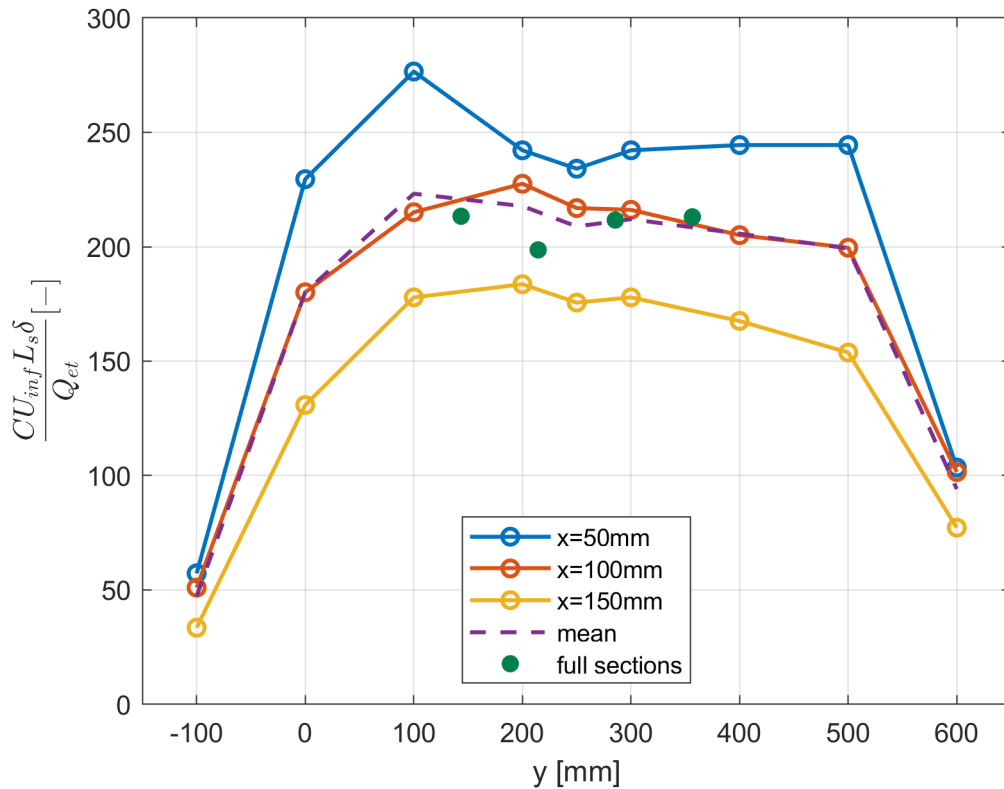


Figure 4.1: Concentration profiles along the reference street canyon

symmetric, with higher values near the upwind wall ($x = 50$ mm) and lower values towards the downwind wall ($x = 150$ mm), due to the recirculation vortex inside the canyon. This result thus shows that the canyon is aligned in a perpendicular position with respect to the wind direction as desired, because if it wasn't, then concentration profiles would not have been symmetric. This graph is also useful to understand that concentration drops quite rapidly when we move outside of the length of the source, as it is possible to see from the great difference between measures at $y = 100$ mm (outside of the source) and at $y = 0$ mm (still above the source); the same happens on the other end of the source.

4.2 Wind profile

Once the alignment has been verified, the second step is the characterization of the logarithmic boundary layer wind profile inside the tunnel. To do so, two different analyses have been done:

- Measures of vertical wind profiles at four different points along the wind direction, to determine the height of the boundary layer and if the boundary layer is fully developed or not;
- Determination of the characteristic parameters of the logarithmic wind profile (friction velocity u_* , roughness length z_0 and zero-plane displacement d) above the reference street canyon.

All the presented results are normalized with respect to u_∞ , so that they can be used to compare different scenarios and they are independent on the wind velocity on the top of the boundary layer, which can change.

4.2.1 Wind profiles along wind direction

For the first part of this work, four different reference points along the wind direction have been chosen (namely $x = -1400$ mm, $x = 0$ mm, $x = 700$ mm and $x = 1400$ mm) and, for each of these reference points, four wind profiles in different positions have been measured and averaged to obtain the final wind profile for the reference point. The four positions chosen for each reference point are based on the periodic unit of the urban canopy, which is repeated all along the length of the wind tunnel:

- Centre of the street canyon ('Canyon' point);
- Centre of the street parallel to the wind flow, immediately to the right of the 'Canyon' point ('Intersection' point);
- A point 350 mm downstream the 'Canyon' point, on the top of the downstream building ('Roof' point);
- A point 350 mm downstream the 'Intersection' point ('Street' point).

Figure 4.2 shows a sketch of the four points; it has to be noted that the reference street canyon ($x = 0$ mm) is a long canyon and for this reason the configuration of that specific unit of the urban canopy is different (no longitudinal streets).

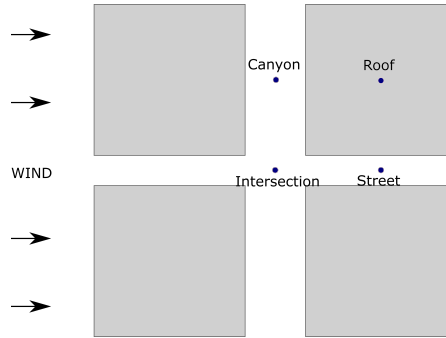


Figure 4.2: Sketch of the four points where wind profiles are measured

Results of this characterization (figure 4.3) show that there is a very good superposition of the various wind profiles measured along the length of the wind tunnel, proving thus that the boundary layer is fully developed, as the wind profile doesn't evolve anymore moving downwind.

A more detailed analysis is performed for the four points measured above the reference street canyon, showing vertical profiles of mean velocity, velocity correlation $\overline{-u'w'}$, standard deviation of u and w and ratio between standard deviation and wind velocity itself (figure 4.4) and an extended wind profile over z (figure 4.5), starting from $z = 100$ mm. In particular, it is clear from these graphs that $\overline{-u'w'}$ (measure that represents Reynolds stresses, which account for turbulent fluctuations in fluid momentum) presents a region where it has an almost constant value. It is also evident that both profiles of $\frac{\sigma_u}{u}$ and $\frac{\sigma_w}{w}$ show higher values in the lower portion of the boundary layer; since these ratios are typically considered an index of turbulence, it is clear that the lower portion of the boundary layer experiences a much higher variability of velocity components, which is due to the presence of buildings (which have less and less effect on wind variability as z increase).

It is important to note that, since these data come from LDA measures, they

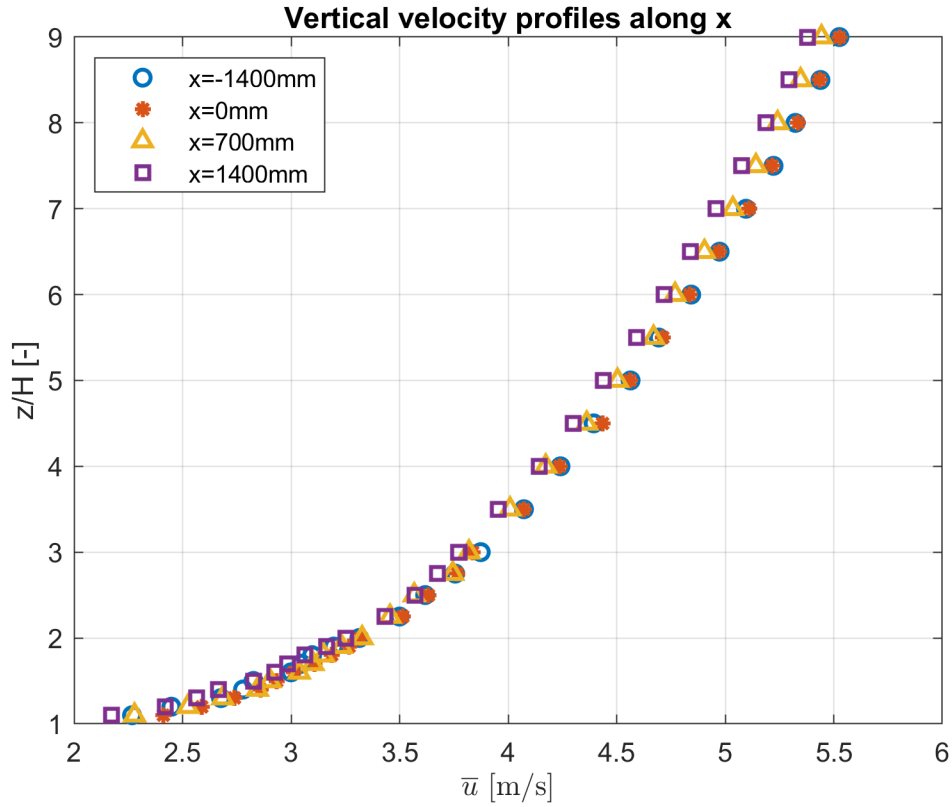


Figure 4.3: Wind profiles along x direction

are characterized by a non-constant acquisition frequency (because the sampling depends on the seeding, as explained in section 3.2.2) and, for this reason, they need to be treated by taking into account the transit time associated to each instantaneous measure. Accordingly, all the statistics of data coming from LDA measures (and coupled LDA-FID measures) are computed by weighting every instantaneous measure with its own transit time; for example, the average value of u will be:

$$\bar{u} = \frac{1}{\sum_{i=1}^N tt_i} \cdot \sum_{i=1}^N u_i \cdot tt_i \quad (4.1)$$

And the n -th order moment of u will be:

$$E[(u - \bar{u})^n] = \frac{1}{\sum_{i=1}^N tt_i} \cdot \sum_{i=1}^N (u_i - \bar{u})^n \cdot tt_i \quad (4.2)$$

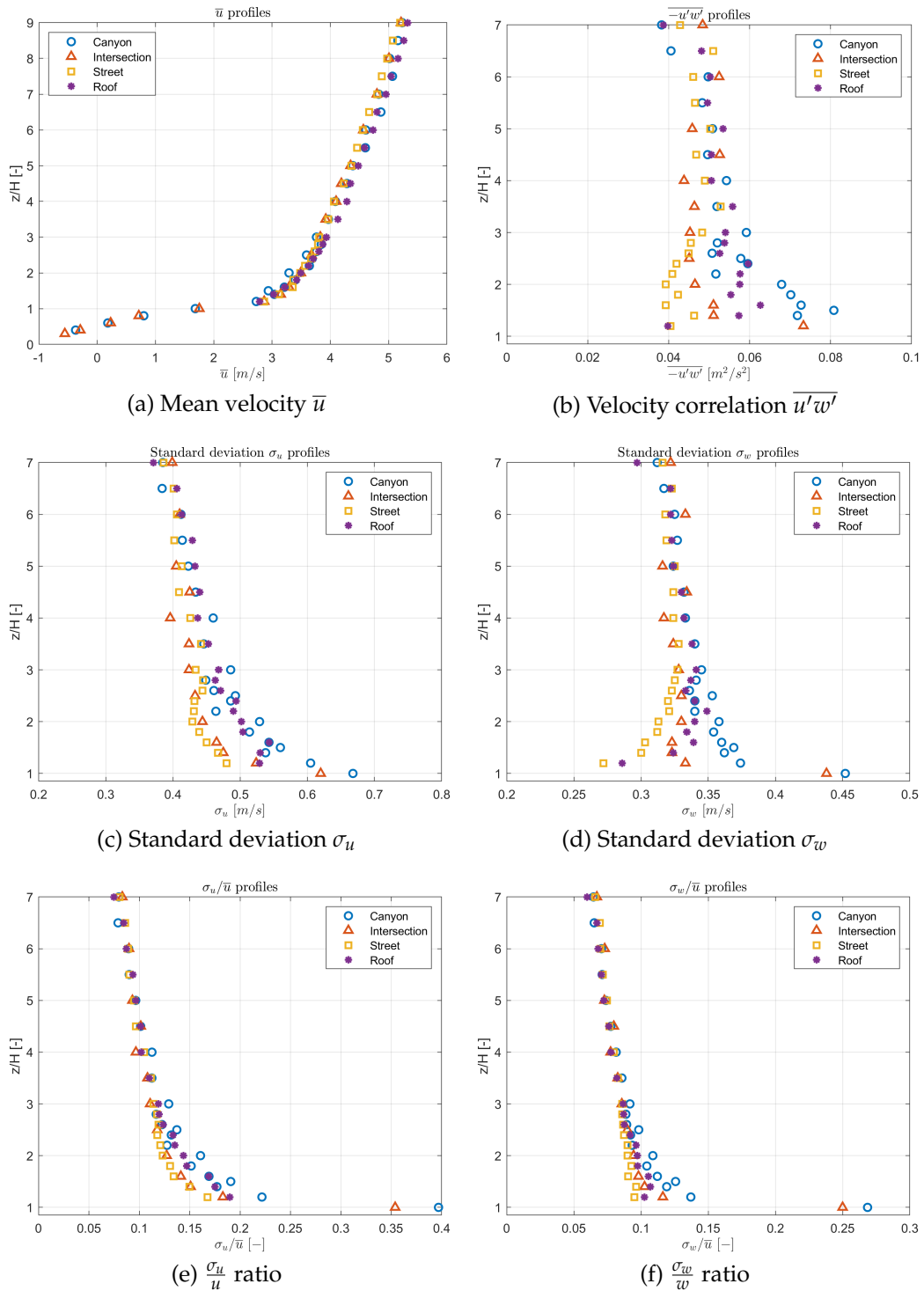


Figure 4.4: Vertical profiles obtained during wind profile characterization

From the extended wind profile, on the other hand, it is possible to measure the height δ of the boundary layer, which is the height at which wind speed stops to increase and remains constant (at a value of u_∞). From figure 4.5 it is possible to see that, for the present experiment $\delta = 1.1$ m; this value thus confirms the choice made earlier for the concentration normalization, based on previous experiments made in the wind tunnel with similar configurations. In this case, velocity measures have been taken with the LDA in the lower region of the windtunnel, while the Pitot tube has been used in the upper region. This choice is due to the fact that over a certain height (approximately $z/H = 8$) the seeding needed for LDA measures is no longer available, because the smoke machine used to produce it cannot send it to those heights, and for this reason it is not possible to use the LDA over the whole height of the tunnel. The Pitot tube, on the other hand, does not need any seeding and despite being less accurate than the LDA is able to provide the needed measures.

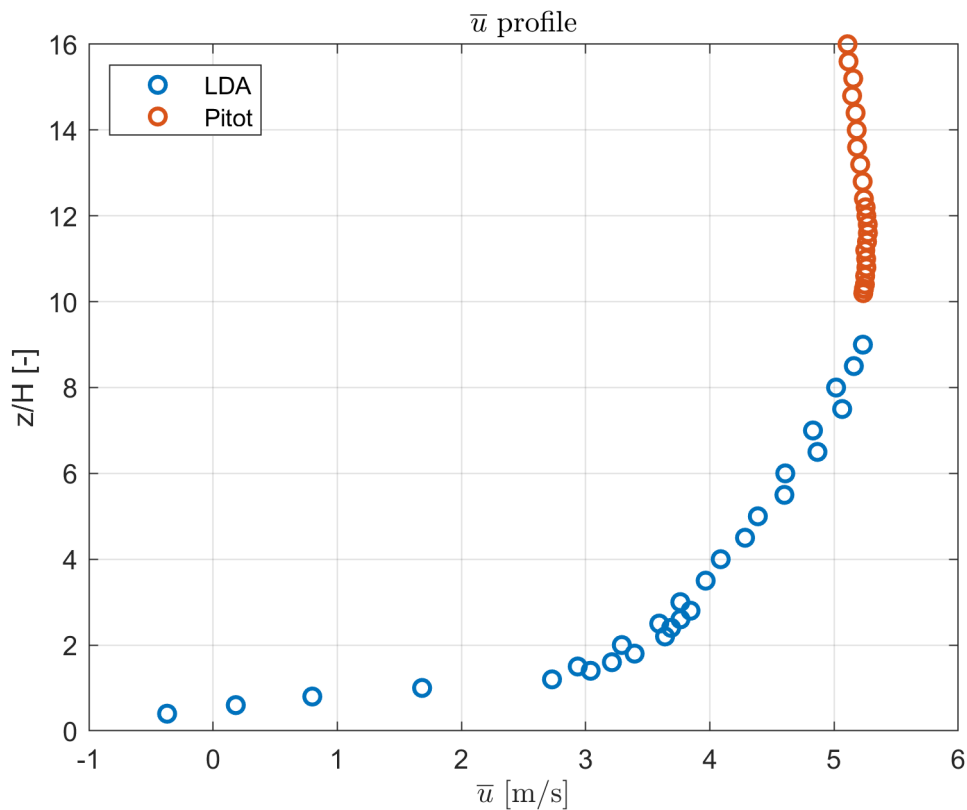


Figure 4.5: Extended wind profile obtained with LDA and Pitot tube

It is also possible to see that above δ height wind velocity remains constant for a certain period and then begins to drop down. This is due to the fact that the wind profile starts to feel the presence of the roof of the windtunnel, where wind velocity becomes null as on the floor of the tunnel.

4.2.2 Characteristic parameters of the wind profile

For the second part of this work, the determination of characteristic parameters of the wind profile above the reference street canyon, the first of the three methods proposed in section 2.2.2 will be used, namely the definition of the logarithmic wind profile in a region where Reynolds stresses can be considered constant (they vary only slightly with respect to their mean value), assuming that the flow is homogeneous on horizontal planes and defined by single length and velocity scales.

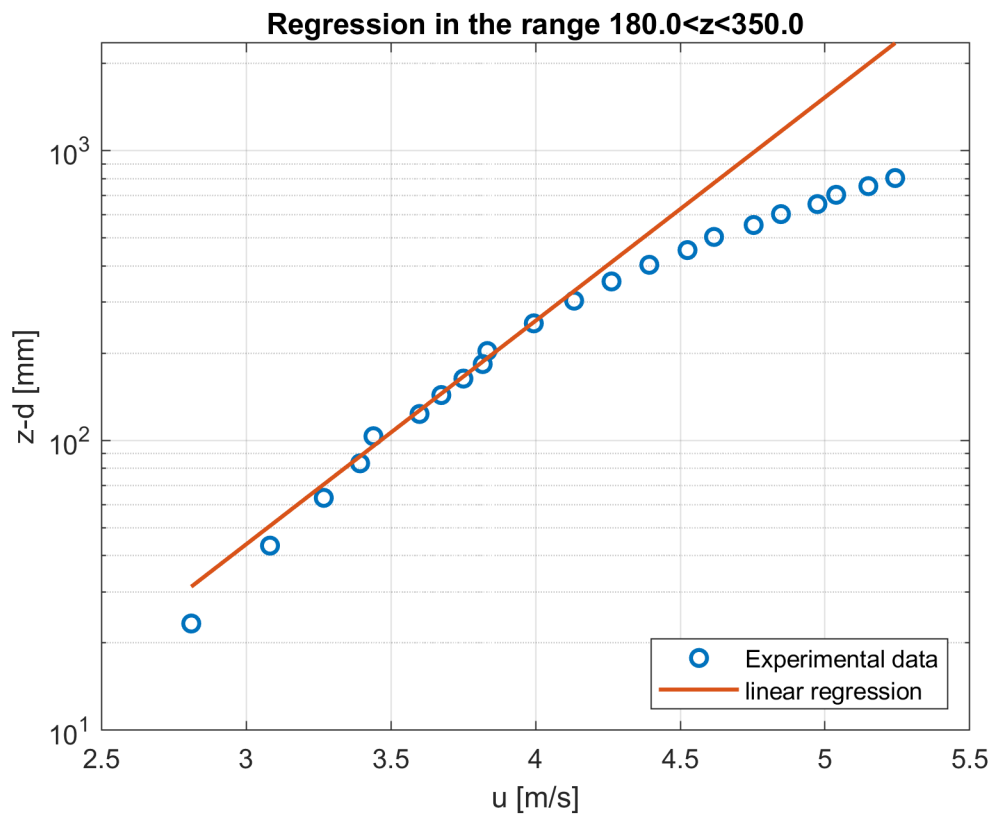


Figure 4.6: Results of linear regression in the interval of constant Reynolds stresses

To this aim, the height interval where velocity correlations can be considered constant has been identified, and given the (constant) value of $\overline{-u'w'}$, friction velocity u_* has been calculated as:

$$u_* = \sqrt{\overline{-u'w'}} \quad (4.3)$$

For the present experiment, the constant velocity correlation range is between $z = 180$ mm and $z = 450$ mm, with $u_* = 0.23$ m/s. Subsequently, to estimate zero-plane displacement d and roughness length z_0 , a linear regression in the plane $e^{\frac{ku}{u_*}} - z$ has been performed, since the logarithmic wind profile can be expressed as:

$$z = z_0 \cdot e^{\frac{ku}{u_*}} + d \quad (4.4)$$

The regression has been done with a procedure of best fitting within the range of constant Reynolds stresses, changing the extremes of the interval of fitting in order to take the one with highest correlation coefficient (R^2). Results of best fitting are shown in figure 4.6, and the corresponding values of interval of fitting, z_0 and d are: interval of fitting: 180 – 350mm, $z_0 = 0.21$ mm, $d = 96.6$ mm.

A similar approach was used by Salizzoni (2006) for the case of a street canyon with H/W ratio of 1/2 and a free stream velocity $u_\infty = 6.7$ m/s; results are presented in table 4.1.

Table 4.1: Comparison between present and past studies

	Height of buildings H [m]	$\frac{u_*}{u_\infty}$ [-]	z_0 [mm]	d [mm]
Present study	0.1	0.04	0.21	96.6
Salizzoni 2006	0.06	0.06	1.7	50

An alternative method is also proposed by Salizzoni (2006), which consists in fitting the logarithmic wind profile with the measured profile by adjusting u_* and z_0 in order to minimize the sum of differences between theoretical and measured points, assuming different d values within a predetermined range and

choosing at the end the one which gives the smallest total error.

5. Preliminary measurements of the vertical exchange velocity u_d

The main aim of the present experimental campaign is to calculate the mass exchange velocity u_d between the canyon and the external atmosphere above it, and see how the presence of trees influences it.

5.1 *Mass exchange velocity u_d*

Mass exchange velocity is a parameter that is used in most box models, which represents the mass transfer between the street canyon and the overlying atmosphere (see Equation 2.14). This phenomenon can be split into two components: turbulent mass transport and mean mass transport. The first one is unsteady and characterized by high intermittency, and it is driven by the dynamics of the shear layer at the top of the canyon, which are themselves influenced by the level of turbulence of the external flow. Within the shear layer (that is the thin layer that can be found at the boundary between the inner portion of the cavity and the outer atmosphere, responsible for the interaction between the two zones) instabilities arise and generate vortices; these vortices grow as they are advected downstream from the upwind corner of the canyon (figure 5.1), and are responsible for the turbulent mass exchange between the canyon and the external atmosphere (Salizzoni, Soulhac, et al. 2009). Turbulent fluxes are influenced not only by the external atmosphere conditions, but also by the canyon aspect ratio H/W and by small-scale roughness, and tend to increase as the canyon becomes larger and as roughness increases (Salizzoni, Van Liefferinge, et al. 2009).

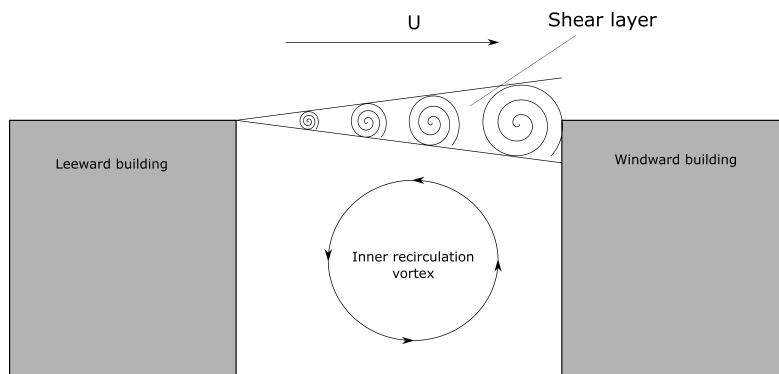


Figure 5.1: Shear layer vortices

The second one represents the mass transport generated by the mean value of the vertical component of wind velocity; at the roof of the canyon (in other word, at the height of the buidings), the vertical component of mean velocity is nearly null (figure 5.2), so mean mass transport can be neglected (Salizzoni, Soulhac, et al. 2009), but if we slightly move inside the canyon, as it is done for the present experimental campaign, this component cannot be neglected anymore.

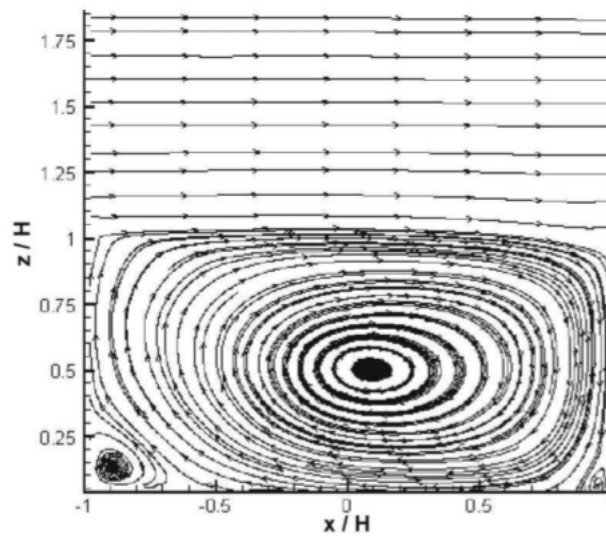


Figure 5.2: Velocity streamlines inside the street canyon; image from Salizzoni (2006)

Once u_d has been calculated, it can also be used to validate parametric dispersion models (such as SIRANE, developed at the *Laboratoire de Mécanique des Fluides et d'Acoustique*, see Soulhac et al. (2011)), whose aim is to get an estimation of this mass exchange velocity knowing only features of the geometry of the urban network, of the pollutant source and of the background concentration advected into the domain by the wind.

The formula used to calculate mass exchange velocity u_d is the following:

$$u_d = \frac{1}{LW \langle c \rangle} \cdot \int_L \int_W (\overline{w'c'} + \overline{w} \cdot \overline{c}) dx dy \quad (5.1)$$

Where L is the canyon length, W is the canyon width, $\langle c \rangle$ is the average concentration inside the control volume, \overline{w} is the mean value of the vertical component of wind velocity, \overline{c} is the mean value of the concentration and $\overline{w'c'}$ is the mean value of the turbulent mass flux (mean value of the product between velocity and concentration fluctuations). The average concentration is computed by averaging the measures taken at four reference sections inside the control volume (sections A, B, C and D), with the grid shown in figure 5.3a, over the reference volume. Measures of \overline{w} , \overline{c} and $\overline{w'c'}$ are taken at a height $z = 95$ mm, on the whole roof of the canyon, with the grid shown in figure 5.3b. The surface integral is then computed numerically, by multiplying each punctual measure by its own reference area and summing all contributes.

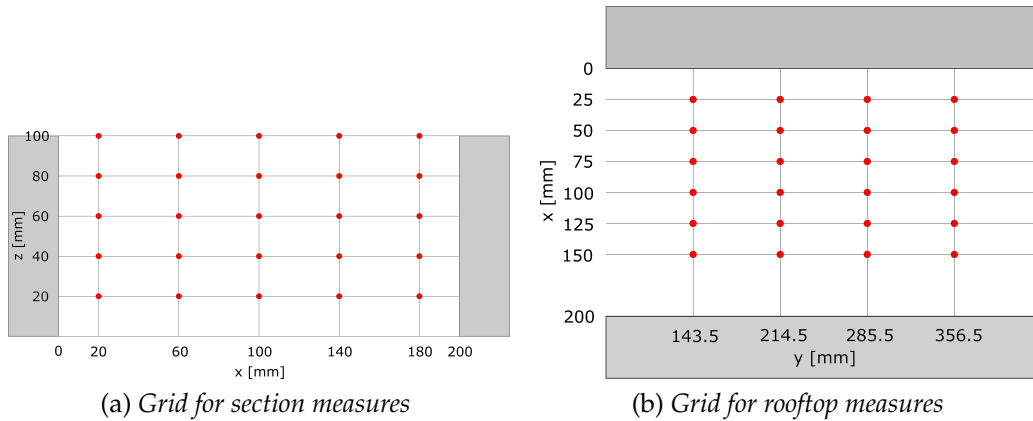


Figure 5.3: Measurement grids

5.2 Data treatment

Particular attention needs to be given to $\overline{w'c'}$ measures; in fact, these are obtained through a combined use of FID and LDA, and the different temporal response of the two instruments gives rise to non-perfectly coupled measures in time, which have to be corrected before being analyzed. The FID, in fact, sucks air from the measurement point and sends it to the combustion chamber, where the actual measure takes place; this process takes a certain time (few milliseconds), and is slower than the acquisition process of the LDA. As a consequence, the time instant at which the LDA measures velocity is the instant at which the FID sucks air from the sampling point, but this does not correspond to the time instant at which the FID actually measures the concentration (which is shifted few milliseconds forward). The acquisition programme, however, is not able to take this delay into account when acquiring the measures (meaning that velocities and concentrations are saved at the same time instant, but concentrations should be saved after the delay to be correctly coupled with their corresponding velocity measures), and this results in the fact that the output file contains velocity and concentration measures that are not actually coupled in time, leading to non reliable estimates of cross-correlations.

To solve this issue, once the data have been acquired, it is necessary to manually calculate the cross-correlations (in our case $\overline{w'c'}$) in a reliable way; to do so, we decided to adopt the "sample-and-hold" (S+H) reconstruction and re-sampling method. It consist of the following steps:

- Shifting the FID signal with a suitable time delay Δt_{lag} ;
- Resampling the concentration values on the same temporal pattern of LDA measures (the velocity measures);
- Computing the cross-correlations with transit-time weighting.

This method is quite straightforward and it has the advantage to require a very low computational cost; however, the most well-established technique to compute cross-correlations is the slot correlation technique (Mayo 1975; Muller

et al. 1998; Nobach 2016), which on the other hand requires a high computational cost and is much more complex to implement. The results obtained with the S+H method have been proven to be sufficiently reliable, with a maximum error of 6% for some points (Marro et al. 2020).

The optimal value of Δt_{lag} is obtained by combining an analysis of the characteristics of the FID sampling tube, to compute a first approximate value of Δt_{lag} , and a sensitivity analysis around Δt_{lag} , in order to find the value of $\Delta t_{lag,opt}$ that leads to the highest correlation coefficient for $\overline{w'c'}$:

$$R_{\overline{w'c'}} = \frac{\overline{w'(t) c'(t)}}{\sigma_w \sigma_c} \quad (5.2)$$

In fact, velocity and concentration measures are not independent and for this reason their correlation coefficient reaches the maximum when the $\Delta t_{lag,opt}$ is adopted.

The approximate value of Δt_{lag} is computed as $\Delta t_{lag} \approx \frac{L_c}{\overline{u_c}}$, where $\overline{u_c}$ is the mean travel velocity along the capillary tube and L_c is the length of the capillary tube; $\overline{u_c}$ is obtained from the formula for pressure drops along a smooth pipe: $\Delta p = \frac{L_c}{2r_c} \cdot \frac{\rho_{air} \overline{u_c}^2}{2} \cdot \lambda_f$, where λ_f is the head-loss coefficient, equal to $\lambda_f = \frac{64}{Re_c}$ in the case of laminar flow.

5.3 Mass conservation verification

Before computing the mass exchange velocity for both the layout with trees and the layout without trees, a verification of mass conservation has been performed for the case without trees, by measuring on the whole rooftop of the canyon the exiting mass flowrate (turbulent and mean) and comparing it with the source. To do so, measures of \overline{w} , \overline{c} and $\overline{w'c'}$ have been taken on a grid which is much larger than the source, in order to be sure to catch almost all the emitted ethane. The grid is shown in figure 5.4: blue dots correspond to real measurements, orange dots correspond to values extrapolated from real measure trends. Extrapolated values are needed close to the canyon walls because the LDA mirror (needed for laser reflection) has its own volume, which does not allow the

instrument to perform measures close to the canyon walls (especially the downwind one, due to the asymmetry of the mirror).

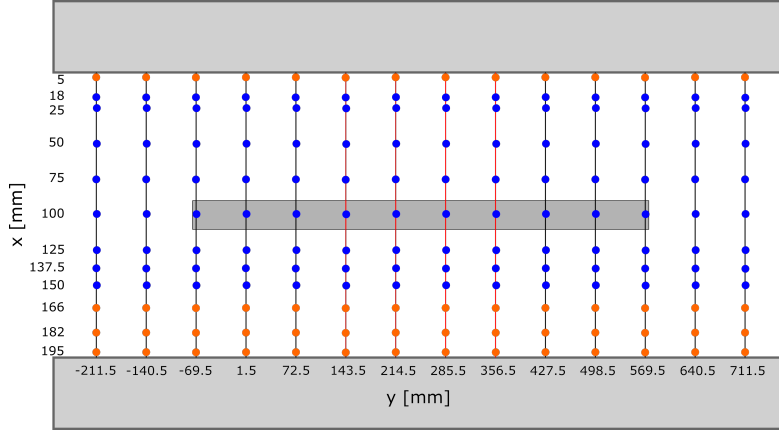


Figure 5.4: Grid adopted for $\overline{w'c'}$, \overline{w} and \overline{c} measures

The extrapolation process has been performed by taking into account the trend of the first three measures of each section ($x = 18$ mm, $x = 25$ mm and $x = 50$ mm) for the upwind wall and the trend of the last three measures of each section ($x = 125$ mm, $x = 137.5$ mm and $x = 150$ mm) for the downwind wall, exploiting then a best-fit procedure in order to obtain the needed values. Results show that the best-fit curve for $\overline{w'c'}$ is an exponential ($a + b \cdot e^{cx}$ for the upwind wall, $a \cdot e^{bx}$ for the downwind wall), while the best-fit curves for \overline{w} and \overline{c} are lines; in particular, for the mean concentration a single line fits quite well all the measures, while for wind velocity two different lines have been used for the upwind and downwind walls (figure 5.5).

The choice of the extrapolated points ($x = 5$ mm, $x = 166$ mm, $x = 182$ mm and $x = 195$ mm) has been made because turbulent fluxes are expected to increase consistently as we get close to the downwind wall, while mean fluxes are expected to become important close to both walls, where vertical mean velocity is non-null (positive on one side and negative on the other, following the recirculating pattern inside the canyon) and concentration is higher.

Figure 5.6 shows both turbulent and mean fluxes maps for the measured points (no extrapolation); as expected, $\overline{w'c'}$ increases as we move along the wind

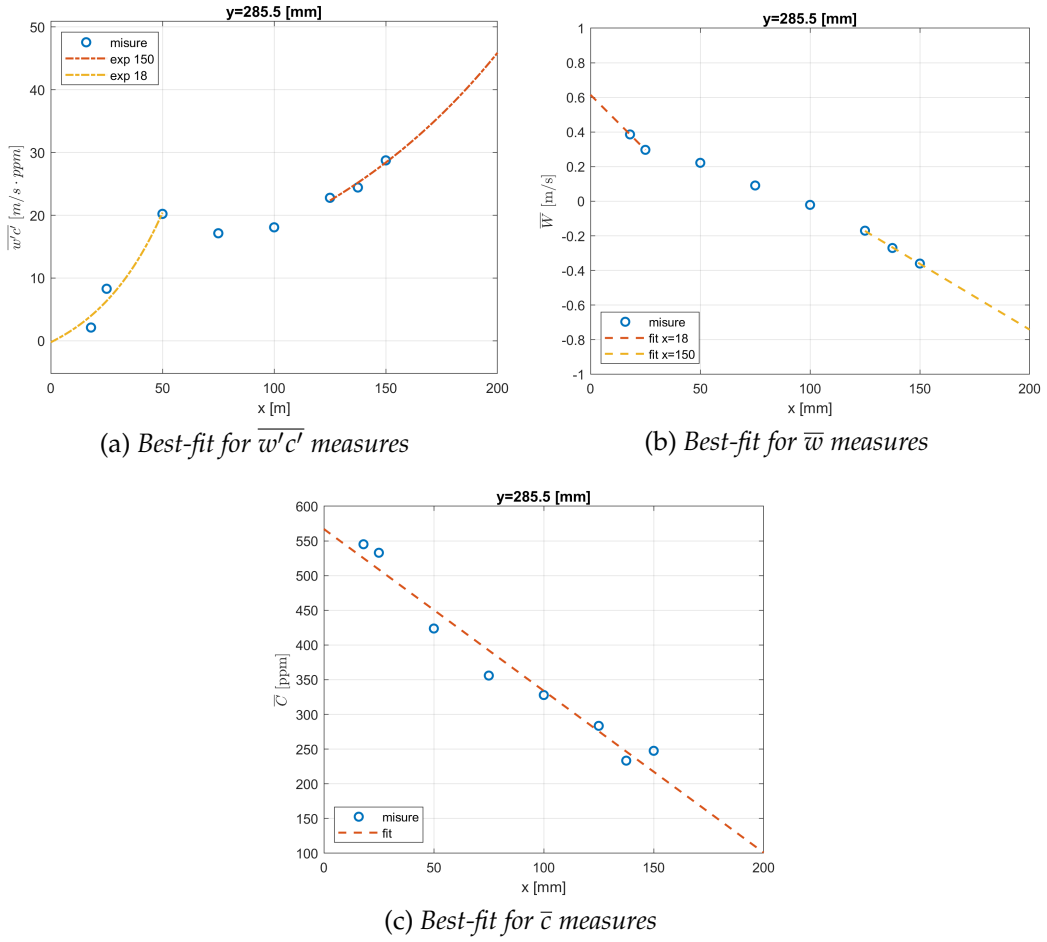


Figure 5.5: Best-fit for measured values

direction, while \overline{w} has positive values close to the upwind wall (exiting direction) and negative values close to the downwind wall (entering direction). \overline{c} is instead higher in the zone near the upwind wall, since the recirculation vortex inside the canyon tends to drag pollutants there. This results in a mean flux $\overline{w} \cdot \overline{c}$ that is highly positive close to the upwind wall (flux exiting the street canyon) and negative close to the downwind wall (flux entering the street canyon); globally, however, the mean flux is directed outside the canyon.

The global exiting mass flowrate is computed by integrating the global flux at the rooftop on the corresponding surface:

$$q_{out} = \int_L \int_W (\overline{w'c'} + \overline{w} \cdot \overline{c}) dx dy \quad (5.3)$$

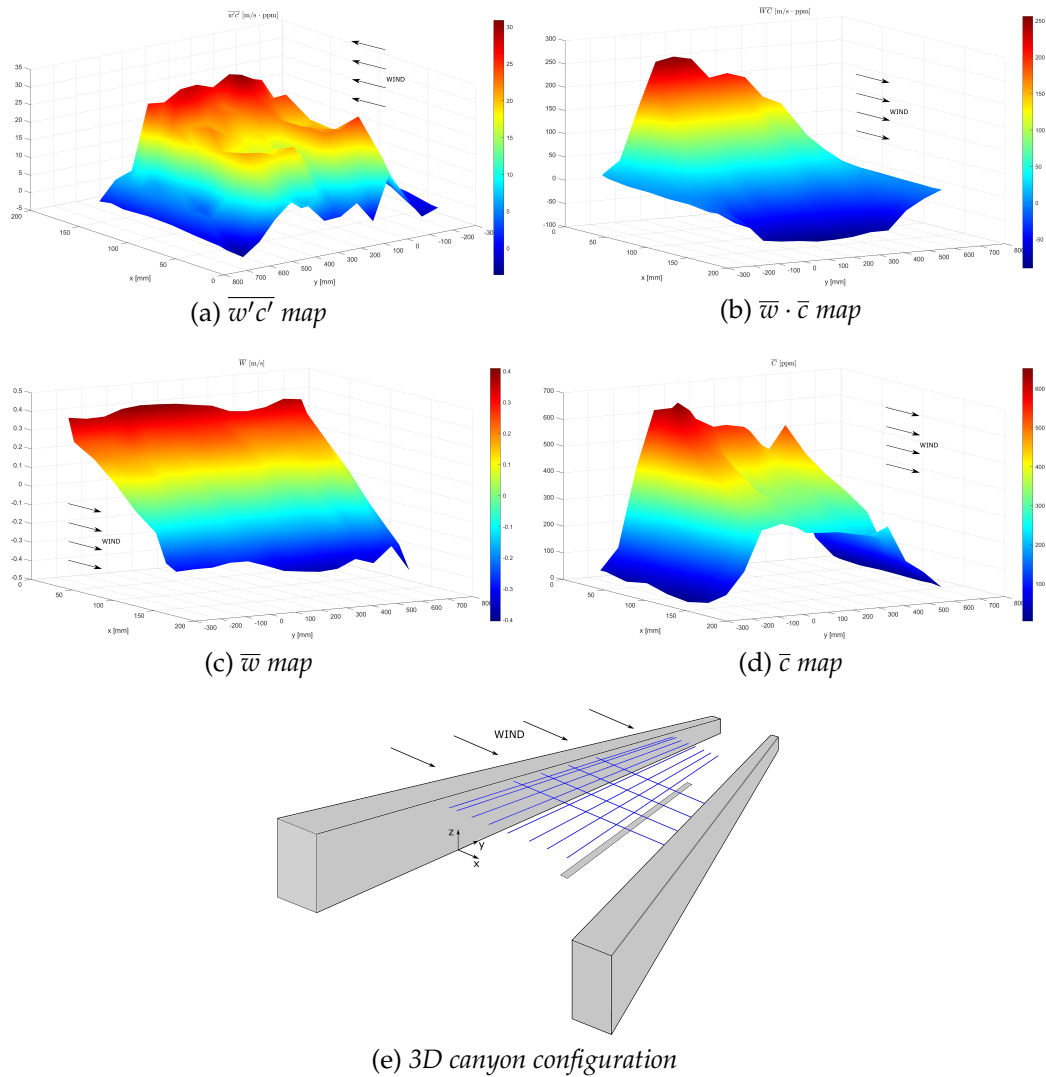
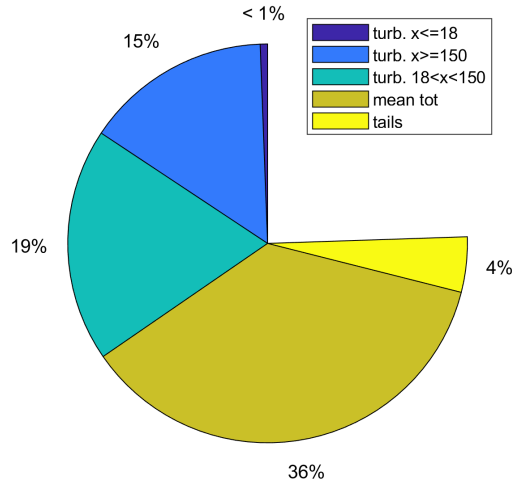


Figure 5.6: Maps of measured values and relative 3D canyon configuration and measurement grid

The result of this integral, which is computed numerically as explained before, can be split into different contributes, namely the turbulent contribution, the mean contribution and the global contribution of the so-called "tails". These tails account for the global exiting flux from the portion of the street canyon which is not included into the control volume of the measures (so for $y < -211.5$ mm and $y > 711.5$ mm); a small fraction of the emitted ethane, in fact, will be diffused towards the walls of the windtunnel, but it will still exit from



(a) Pie chart with the results of the integral

	$x < 18$ mm [%]	$x > 150$ mm [%]	18 mm $< x < 150$ mm [%]	total [%]
Mean flux	45.2	-37.7	28.9	36.4
Turbulent flux	0.6	15.1	18.9	34.6
Tails	-	-	-	4.5
Total	45.8	-22.6	47.8	75.5

(b) Numerical results of $\frac{q_{out}}{q_{source}}$

Figure 5.7: Results of the integral

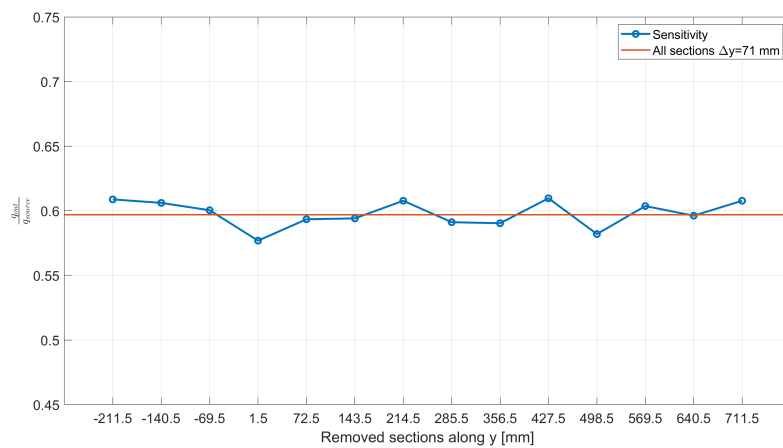
the rooftop since the long canyon has no intersections; tails account for this contribution, by considering the measured values closest to the windtunnel walls ($y = -211.5$ mm and $y = 711.5$ mm sections) constant for the whole remaining length of the canyon.

Results of the integral (normalized by the source emission) are shown in figure 5.7a and table 5.7b: the first thing that needs to be noted is the fact that only $\approx 75\%$ of the entering flowrate has been recovered from the rooftop. This result, despite being not so close to 100%, can be accepted considering all the extrapolations made; in particular, the extrapolation of $\overline{w'c'}$ made for $x > 150$ mm may not reflect perfectly the reality of the phenomenon, because turbulent fluxes are expected to increase closer to the downwind wall, but the last available measures ($x = 150$ mm) are probably too far from the wall to really get the trend of $\overline{w'c'}$ in that particular zone. Concerning the various contributions, the mean

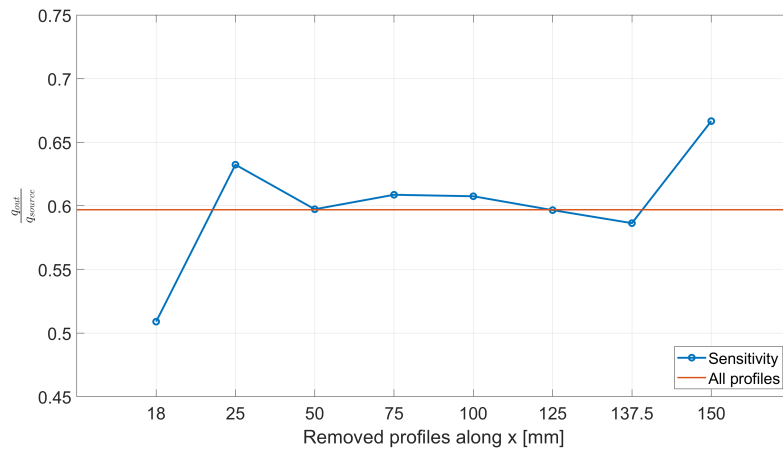
flux and the turbulent flux have almost the same impact on the global flux (even if the turbulent flux is always exiting the canyon, while the mean flux is entering on one side and exiting on the other), while tails have a very small impact.

5.4 Sensitivity analysis on the grid refinition

Once the integral has been calculated, a sensitivity analysis on the grid used for measures at the rooftop has been performed; the aim is to demonstrate that the grid adopted for the measures necessary to calculate u_d is sufficiently refined by



(a) Sensitivity analysis on single sections

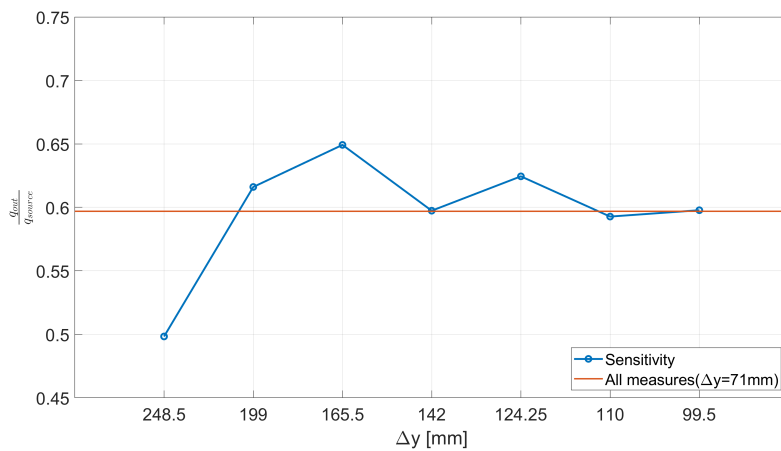


(b) Sensitivity analysis on single profiles

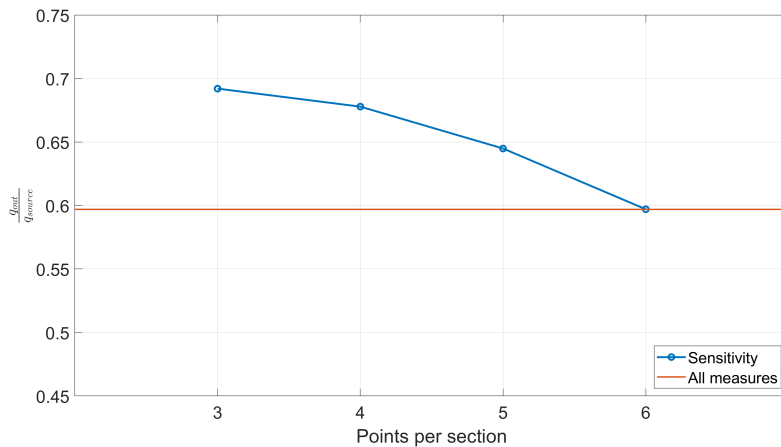
Figure 5.8: Sensitivity analysis: every point on the x axis corresponds to the removed section/profile

showing that the exiting flowrate almost doesn't change if we reduce the number of points used for the integral computation. For this section only measured points are taken into account, since the extrapolation points do not take part to the actual grid for measurements.

The sensitivity of the exiting flowrate on each section, as well as the sensitivity on each profile along y has been assessed by computing the integral several times, removing each time a different section/profile of measures (figure 5.8). Results show that no particular section has a deep impact on the exiting flux, while the two profiles closest to the canyon walls do contribute heavily to the



(a) Number of sections



(b) Number of points per section

Figure 5.9: Sensitivity analysis on the measurement grid

integral result, and thus cannot be removed from the final grid.

Then, by reducing the number of considered sections (increasing thus the Δy between two consecutive sections, but keeping the number of points per section fixed), results show that a good approximation of the most precise value (obtained with 14 sections and a Δy of 71 mm) is achieved with just 9 sections and a Δy of 110 mm, while by reducing the number of measurement points on each section (keeping however the ones which give the greatest contribution and the number of sections fixed), a good approximation of the most precise value (obtained with 8 points on each section) is obtained with just 6 points per section (figure 5.9).

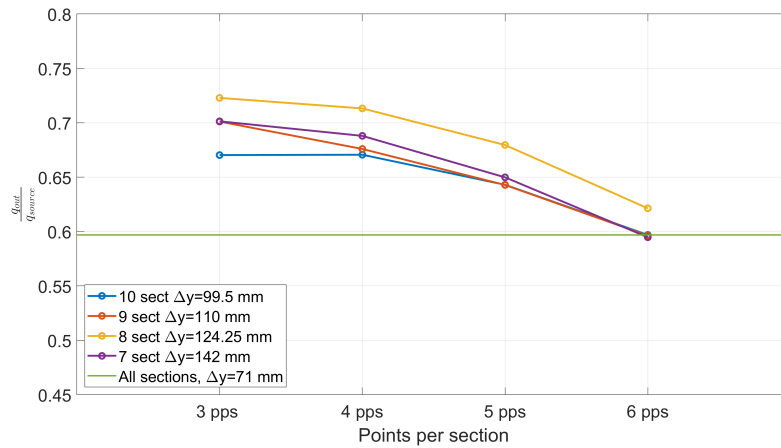


Figure 5.10: Sensitivity analysis; combination of results presented in figure 5.9

Finally, by combining these results, figure 5.10 show that reducing the number of sections to 9 and, at the same time, the number of points per section to 6 doesn't cause the exiting flux to vary with respect to the most precise value (the relative error is lower than 1%). It is thus possible to conclude that the grid used for the measures needed to calculate u_d is sufficiently refined, as the same result is obtained with a less refined grid. Still, it has to be remembered that these results are obtained with respect to the most accurate measured values, but as explained previously these allow to recover only 75% of the source.

5.5 Results

5.5.1 Concentration maps

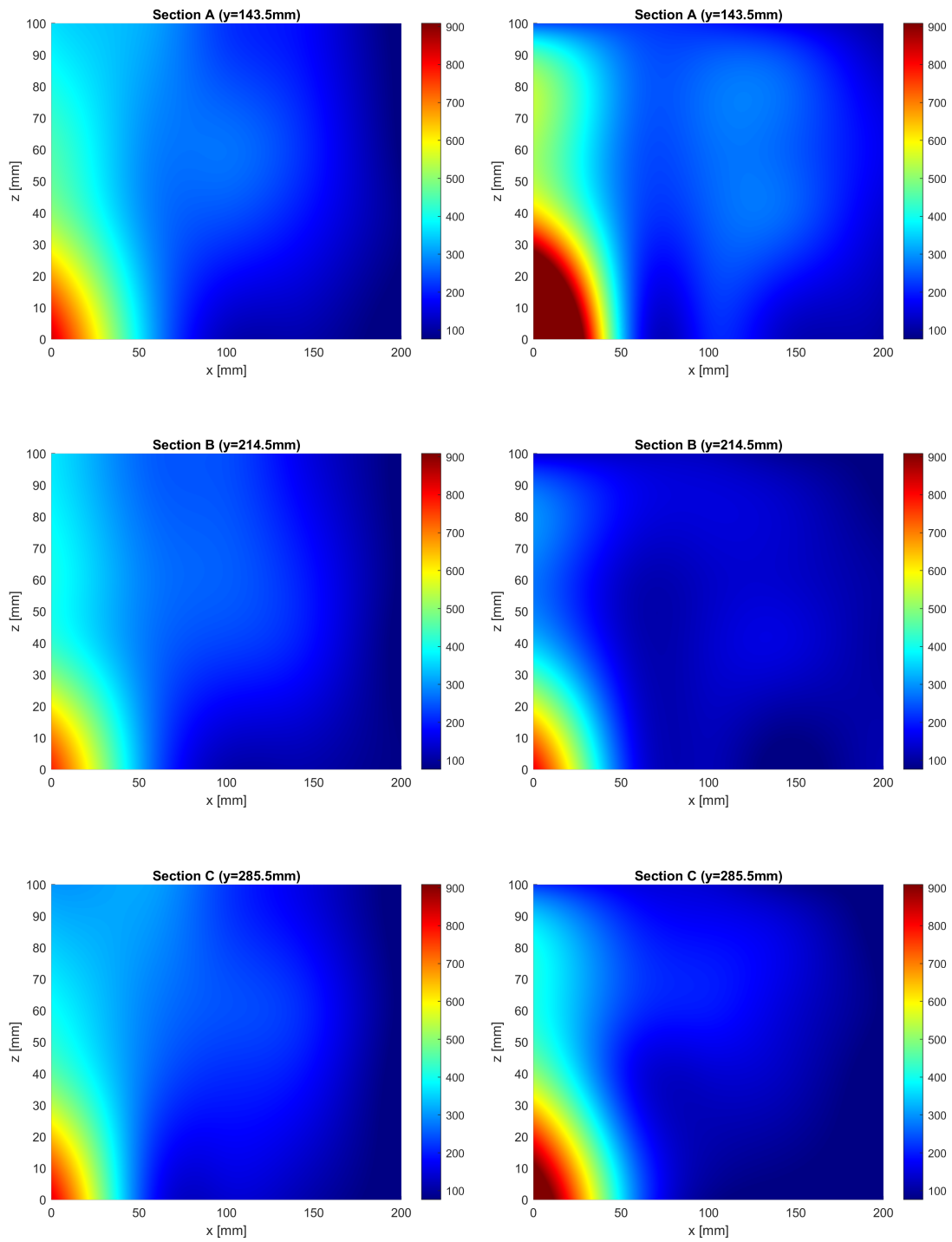
Concentration measures inside the street canyon have been taken on the grid displayed in figure 5.3a, using the Flame Ionization Detector, for both configurations (with trees and without trees). A linear extrapolation process has been made to obtain concentration values close to the canyon walls and to the street, namely at $x = 0$ mm, $x = 200$ mm and $z = 0$ mm. Results show that, for each section of the two configurations, concentrations are higher in the area close to the upwind wall, especially in the lower corner. This is due to the presence of the internal canyon vortex, which at ground level tends to transport pollutants from the upwind to the downwind wall, as shown in figure 2.1 (Gromke and Ruck 2007).

When comparing the two setups, it is possible to see that concentration maps in the no-trees configurations are very similar for all four sections, giving proof of the fact that in such setup the experiment can be considered bidimensional. On the other hand, for the configuration with trees, concentration maps not only show differences with respect to the no-trees layout, but also between the four sections considered (figure 5.10). This result shows that the presence of trees alters the bidimensionality of the experiment, leading to higher concentrations in the external area of the control volume (sections A and D) and lower ones in the central portion (sections B and C).

This important result can be seen even more clearly by analyzing concentration profiles along y (along the street canyon), for different values of x (figure 5.10). It is possible to see that concentrations are almost constant along the four sections for the no-trees case, while with trees concentrations tend to vary consistently between the four sections. A sort of symmetry with respect to the centre of the source is still present, especially when moving towards the downwind wall (higher x values), but it is evident that the experiment can no longer be considered bidimensional.

Concentration measures are needed when computing u_d , more specifically

Preliminary measurements of the vertical exchange velocity u_d



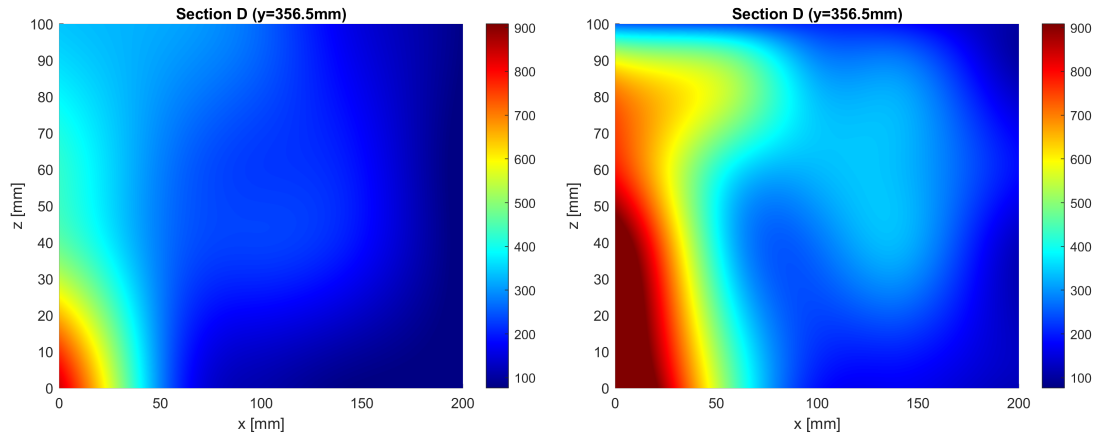
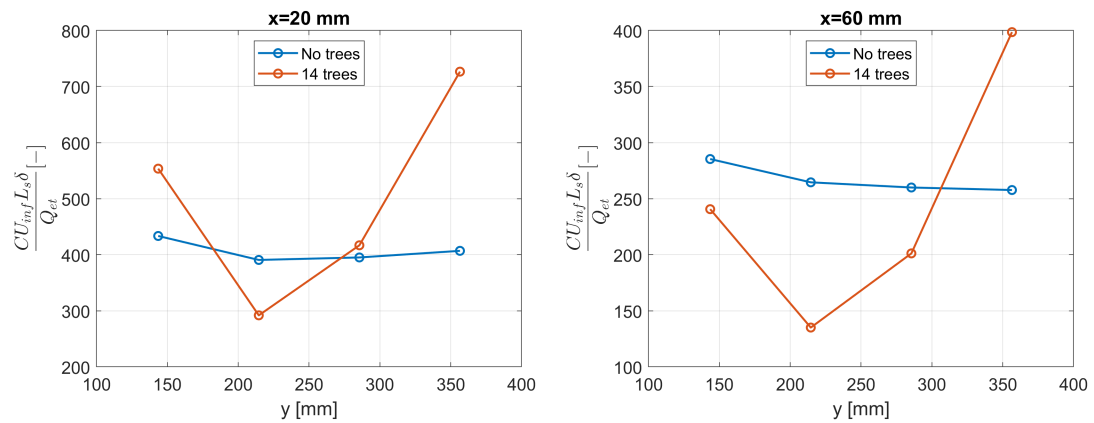


Figure 5.10: Concentration maps on the four reference sections; configuration without trees on the left, configuration with trees on the right

the average concentration on the control volume. This is obtained by multiplying each puntual concentration measure by its corresponding volume, summing all contributes and then dividing everything by the total volume:

$$\langle c \rangle = \frac{\sum_{i=1}^N c_i \cdot V_i}{V_{tot}} \quad (5.4)$$

As expected, the average concentration is higher in presence of trees, as already proven by past studies (Gromke and Ruck 2007; Gromke and Ruck 2009; Buccolieri, Gromke, et al. 2009; Buccolieri, Salim, et al. 2011): 189.9 ppm for the configuration without trees, 206.2 ppm for the configuration with trees.



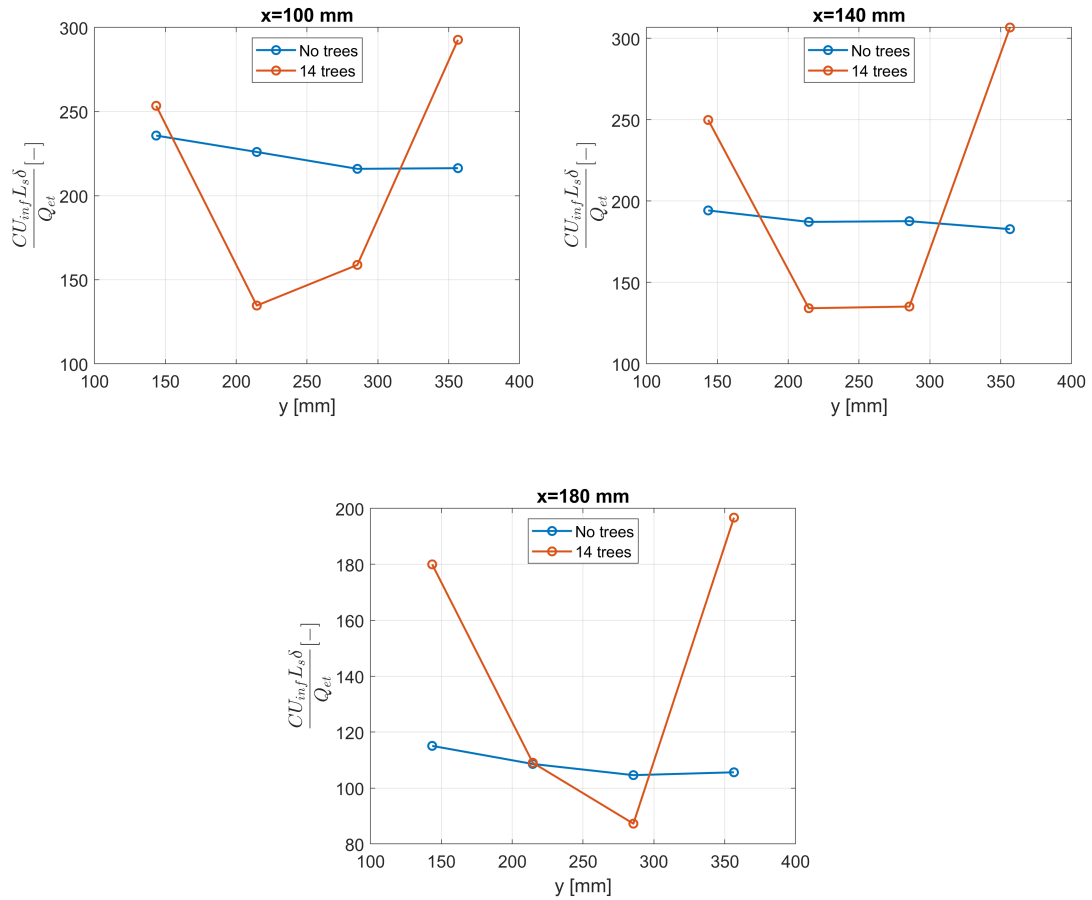


Figure 5.10: Concentration profiles along y. Each point is the average concentration over z, for the given x and y value.

However, the difference is not so marked. This is probably due to the fact that concentrations become higher between trees and canyon walls, as well as very close to trees in general, but the Flame Ionization Detector cannot reach those points in such a small scale model. Measured concentrations in the presence of trees are thus higher than without trees, but are still very likely to be underestimated.

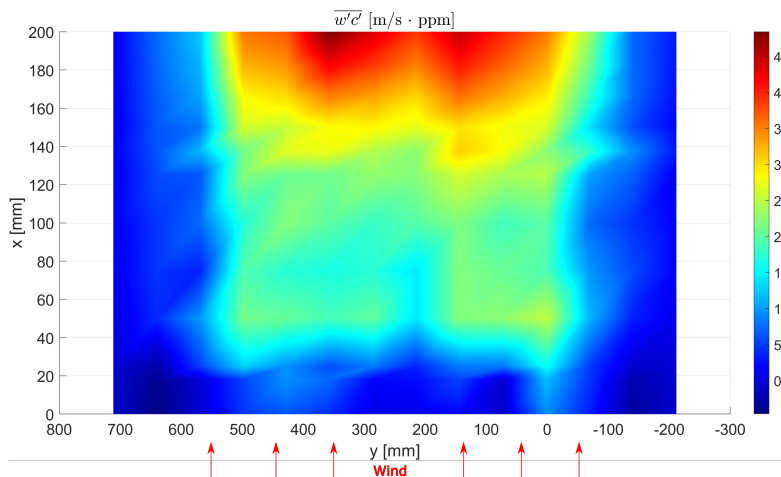
5.5.2 Flux maps

The mass fluxes needed to compute u_d are the ones at the rooftop of the canyon. All the maps at the rooftop in the no-trees configuration are more extended

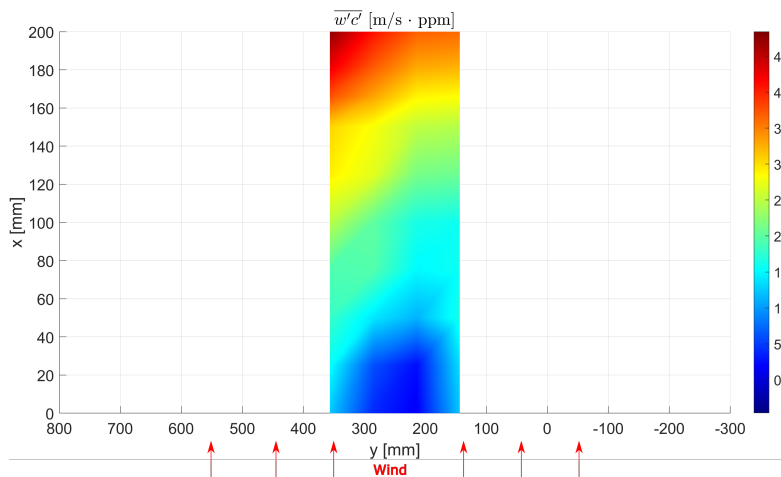
along y than the ones in the configuration with trees because measures outside the control volume have been performed for the mass conservation verification. However, all the quantities calculated in the following sections are referred only to the four sections in the control volume also for the setup without trees. Figure 5.11 shows turbulent vertical fluxes $\overline{w'c'}$, while figure 5.12 shows mean vertical fluxes $\overline{w} \cdot \overline{c}$, for both setups (with and without trees). Extrapolation close to the canyon walls (see figure 5.5) is considered for both layouts, in order to be sure not to underestimate vertical fluxes. Turbulent fluxes tend to increase when moving towards the downwind wall (see section 5.1), while mean fluxes are bigger close to the upwind wall. Considering the two configurations, no big differences can be seen in the turbulent fluxes, while mean fluxes are higher in the configuration with trees due to the presence of a higher mean concentration (figure 5.14) that overcomes a slightly lower wind velocity (figure 5.13).

By summing and integrating the two fluxes over the surface of the rooftop of the canyon it is possible to obtain the total vertical flowrate exiting the street canyon. Results in table 5.1 are presented in the form $\frac{q_{vert}}{q_{source}}$, for a more clear understanding. It is possible to see that the vertical flowrate increases significantly when trees are introduced, as it passes from 69% of the source to 110% of it. By computing a very simple mass balance it is also possible to calculate the lateral flowrate, as $q_{source} - q_{vert}$. This can help understanding the fact that, while in the configuration without trees there is a non-negligible lateral flux exiting the control volume, in the configuration with trees this flux not only vanishes, but becomes slightly negative, meaning that a small flux enters the control volume.

However, due to the fact that the presence of trees alters the bidimensionality of the experiment, the vertical flowrate changes inside the control volume along y in the configuration with trees, and depends thus on the size of the control volume considered. This is probably due not only to the presence of the trees, but also to the fact that even if the source is longer than the control volume, it is not so long to be considered infinite with respect to the control volume itself. The length of the source is the same also in the case without trees, but in that configuration bidimensionality is still achieved since probably it is the presence of trees that triggers the loss of bidimensionality. In the setup without trees, in fact, the vertical flux is constant along y , and so is the lateral flux,



(a) No trees setup



(b) 14 trees setup

Figure 5.11: $\overline{w'c'}$ maps

even if it is not negligible.

This result is surprising, because the expectations were to obtain a higher vertical flux in the no-trees configuration, as the presence of vegetation is supposed to reduce the mass exchange between canyon and outer atmosphere. However, since no one previously performed a similar experiment, measuring mass fluxes in order to compute the exchange velocity, it is not possible to know if the measurement grid at the rooftop is refined enough, and what is the error that is made on the flux computation by using such grid. Moreover, the role of

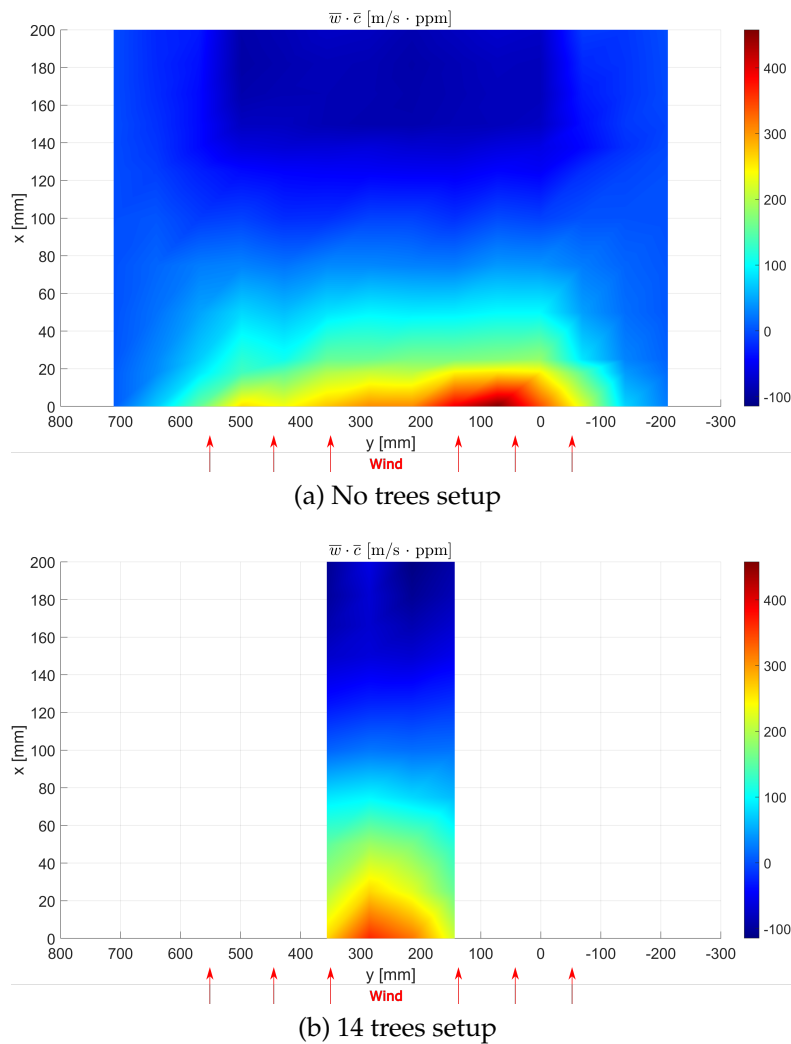


Figure 5.12: $\bar{w} \cdot \bar{c}$ maps

the lateral flux still has to be clarified, as in the present thesis it has been simply calculated through a mass balance, but it should be also directly measured as the vertical one in order to have a further verification of mass conservation.

For all these reasons, the results and the measurements in this work have to be considered preliminary, very useful and necessary to understand the criticalities of the experiment and the possible ways to cope with them. To clarify if the measurement grid is refined enough, further measures at the rooftop should be taken after closing the street canyon on the lateral sides of the control volume. In this way, all the pollutant emitted by the source has to exit the control volume

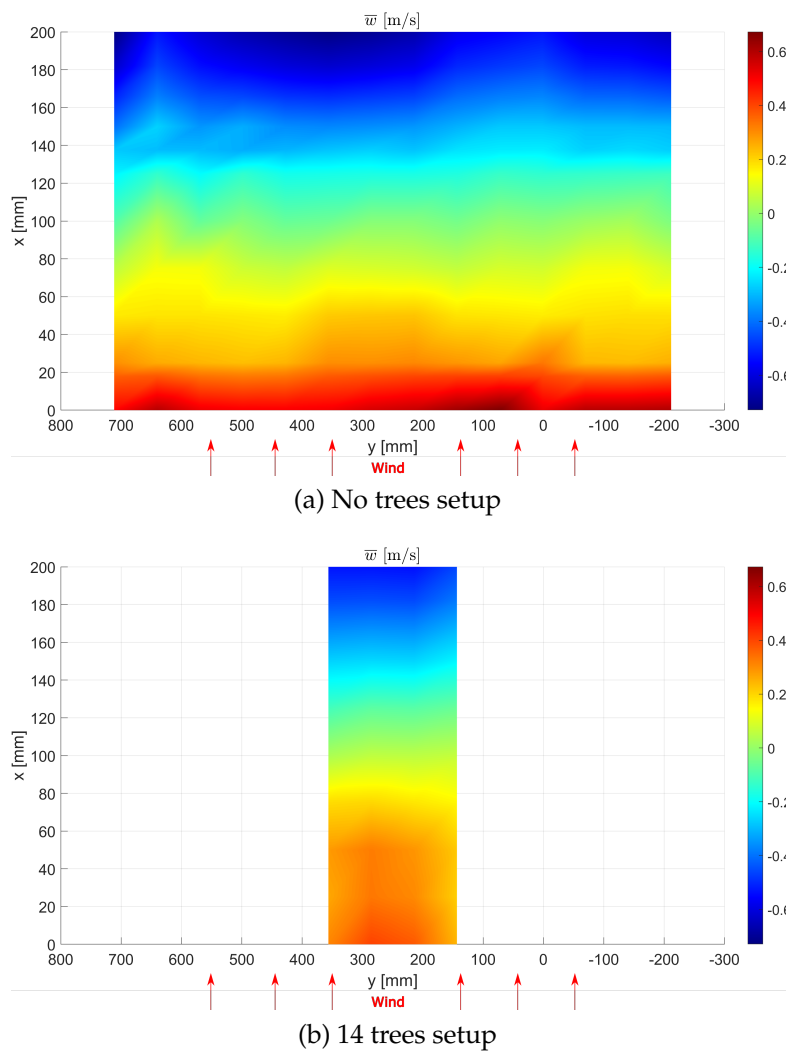


Figure 5.13: \bar{w} maps

from the top (as the sides are blocked), and it is thus possible to calculate the error made in the flux computation when using a more or less refined grid.

5.5.3 Vertical exchange velocity

Putting together all the previous results, it is now possible to compute the vertical mass exchange velocity u_d and see how the presence of trees influences it. Results are presented in table 5.1, where also flowrates and average concentrations are reported. It is possible to see that u_d is higher for the layout with trees,

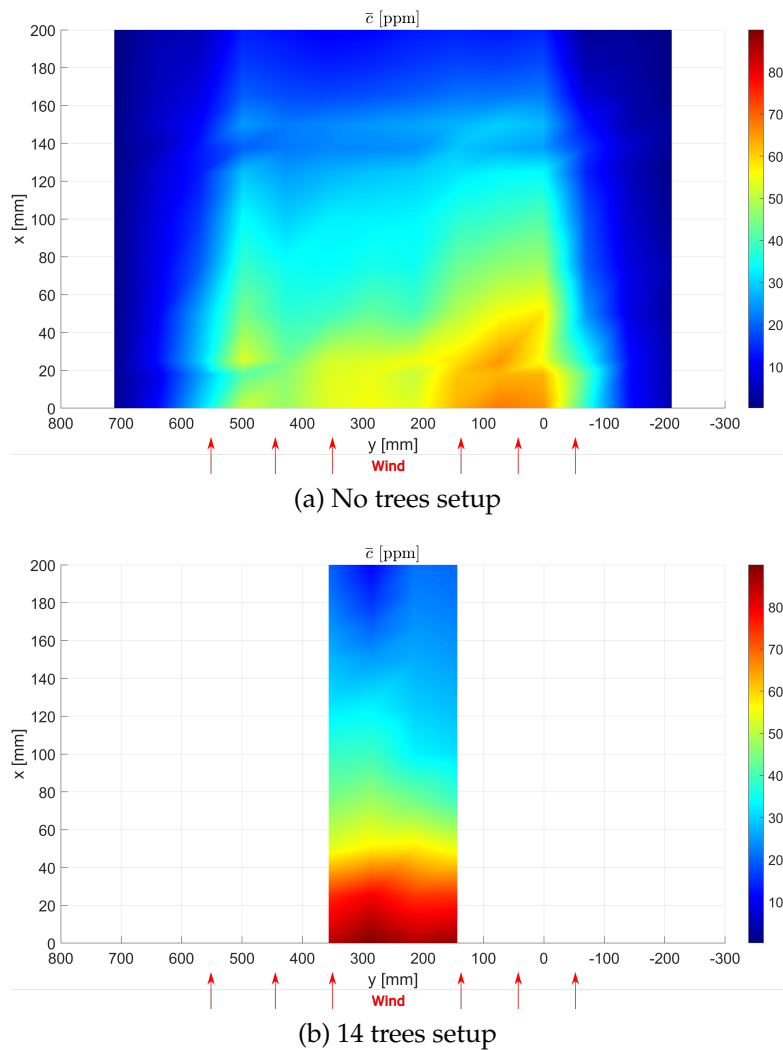


Figure 5.14: \bar{c} maps

due to the fact that the measured vertical flowrate is significantly bigger, even if the also the average concentration in the control volume is higher.

However, since flux measures are still to be verified (as explained in the previous paragraphs), a different way to calculate u_d is to consider the exiting vertical flux equal to the source flux, as done by Salizzoni, Soulhac, et al. (2009). In this way, the only quantity that varies between the two configurations is the average concentration in the control volume, but it is a less accurate way to compute u_d because it implicitly assumes that trees do not influence the

Table 5.1: Results of the experimental campaign

Quantity	No Trees	14 Trees
$\langle c \rangle$ [ppm]	189.9	206.2
$\int_W \int_L (\overline{w'c'} + \overline{w} \cdot \overline{c}) dx dy \left[\frac{m^3}{s} \right]$	2.51 e-6	4.02 e-6
$u_d \left[\frac{m}{s} \right]$	0.093	0.137
$\frac{u_d}{u_\infty} [-]$	0.017	0.026
$\frac{q_{vert}}{q_{source}} [-]$	0.69	1.10
$\frac{q_{lat}}{q_{source}} [-]$	0.31	-0.10
$\frac{u_d}{u_\infty}$ with $q_{vert} = q_{source} [-]$	0.026	0.023

exiting flux and that the lateral flux is always null. Results in this case are obviously opposite with respect to the ones obtained using the measured flux, since the average concentration is higher in the configuration with trees, leading to a lower vertical exchange velocity.

Further experiments should thus be performed in order to:

- Check the accuracy of flux measures by closing the lateral sides of the control volume;
- Measure directly the lateral fluxes, in order to see if they are negligible or not;
- Increase the length of the source in order to recreate a setup that is not possibly influenced by the length itself, in which the only variable is the presence (or absence) of trees.

Still, the preliminary result obtained with the present experiment are valid, because they confirm that the presence of trees causes an increase in the average concentration inside the canyon. Moreover, they highlight which are the main issues related to flux measures, giving crucial hints on which should be the next experiments needed for a better understanding of the topic.

6. Analysis of the time series of $w'c'$

After having computed the mass exchange velocity u_d and discussed the differences introduced by the presence of trees on such quantity, a more detailed analysis has been done on the time series of turbulent mass flux $w'c'$. This focus is only on a small set of points of the grid, namely the ones on the rooftop of the canyon at $y = 285.5$ mm. This choice has been made because in the portion of street canyon above the source the turbulent mass flux is expected to vary significantly only along the wind direction (x direction) and not along the street canyon (y direction); the choice of the section at $y = 285.5$ mm (and not other sections which are still above the source) has been done because it is in the centre of the source, ensuring thus a sufficient distance from the borders of the source itself, where there is a very quick drop of turbulent mass fluxes.

The aim of this part of the study is again to search for differences between the configuration without trees and the one with trees, as well as to catch the main features of turbulent mass flux $w'c'$ through the analysis of the most relevant statistics of the time series. To do so, two different approaches have been adopted:

- Analysis of traditional statistics (variance, skewness, kurtosis), coupled with a spectral analysis of the $w'c'$ signal;
- Network-based analysis of the $w'c'$ signal, consisting of network creation from the $w'c'$ time series through the visibility graph algorithm and analysis of the network based metrics.

We expect trees to have a certain influence on the turbulent structures that are present in the shear layer, which are responsible for the interaction between

the inner area of the canyon and the atmosphere above it. In particular, the size of turbulent vortices that are generated in the shear layer should be affected by a reduction, caused by the presence of trees, which thus obstaculate the washout process of the cavity (the mass exchange between the inside and the outside of the street, responsible for the removal of pollutants from the cavity).

6.1 *Traditional statistics*

For the first part of this focus, traditional statistics are computed from $w'c'$ time series; these are variance $\sigma_{w'c'}^2$, skewness $s_{w'c'}$ and kurtosis $k_{w'c'}$. Variance is the second order moment of the signal:

$$\sigma_{w'c'}^2 = E[(w'c' - \overline{w'c'})^2] \quad (6.1)$$

Skewness is the third order moment of the signal divided by the standard deviation elevated to the third power:

$$s_{w'c'} = \frac{E[(w'c' - \overline{w'c'})^3]}{\sigma_{w'c'}^3} \quad (6.2)$$

It is a measure of the symmetry of the PDF of the signal, taking as a reference the Gaussian PDF, which has skewness exactly equal to 0. If the skewness is > 0 it means that the right tail of the distribution is longer with respect to the left one, if the skewness is < 0 it is the opposite (figure 6.1a).

This measure can help to understand the shape of the time series in terms of frequency of measures higher (or lower) with respect to the mean value of the series.

Kurtosis is the fourth order moment of the signal divided by the standard deviation elevated to the fourth power:

$$k_{w'c'} = \frac{E[(w'c' - \overline{w'c'})^4]}{\sigma_{w'c'}^4} \quad (6.3)$$

It is a measure of the weight of the tails of the PDF of the signal, taking again as a reference the Gaussian PDF, which has kurtosis equal to 3. If the kurtosis is > 3 it means that the distribution has longer tails with respect to a Gaussian,

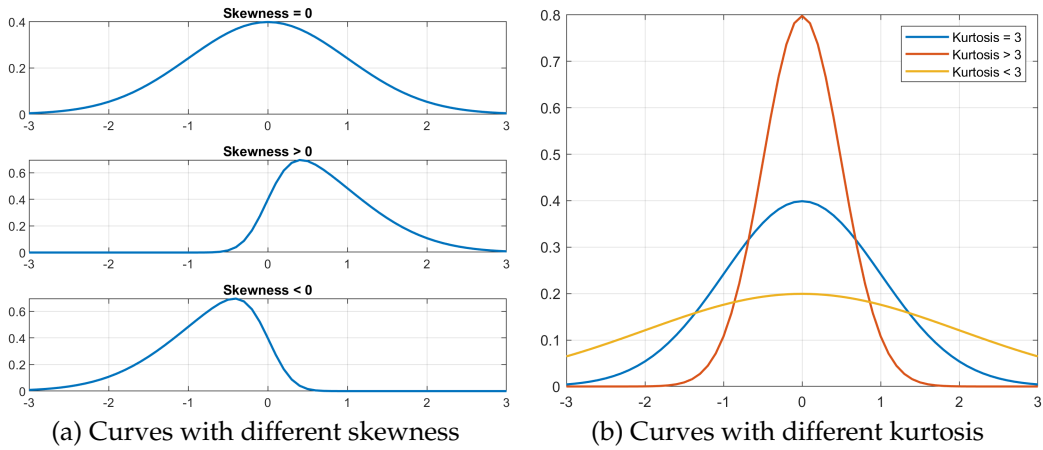


Figure 6.1: Examples of curves with different skewness and kurtosis

leading to a more peaked shape, while if the kurtosis is < 3 it means that the tails are shorter with respect to a Gaussian, leading to a more flatted shape (figure 6.1b). Kurtosis can be interpreted as a measure of the intermittency of the signal: a high kurtosis implies higher probability of finding values that stand far away from the mean value, leading thus to a higher intermittency of the signal.

It is important to remember that all the n -th order moments of $w'c'$ are weighted on the transit time of the particles, since the measures are taken with the LDA and are characterized by a non-constant sampling frequency.

Figure 6.2 shows the trend of $\overline{w'c'}$, as well as the behaviour of variance, skewness and kurtosis for the two layouts. It is possible to see that turbulent mass flux (figure 6.2a) tends to increase for both cases when moving downwind, as expected, but no big differences in the numeric values are introduced by the presence of trees. However, if we analyze both turbulent and mean fluxes, as done in figure 6.3, it is clear that mean fluxes increase consistently when trees are introduced (more exiting flux); this is due to the fact that the presence of trees reduces the size of the internal recirculation vortex, causing more flux to exit from the central zones and less flux to enter from the zone close to the downwind wall. Considering thus the total exiting flux (sum of turbulent and mean ones), the contribution of turbulent mass transport is less important when trees are present, as it passes from 45% of the total flux for the case without trees

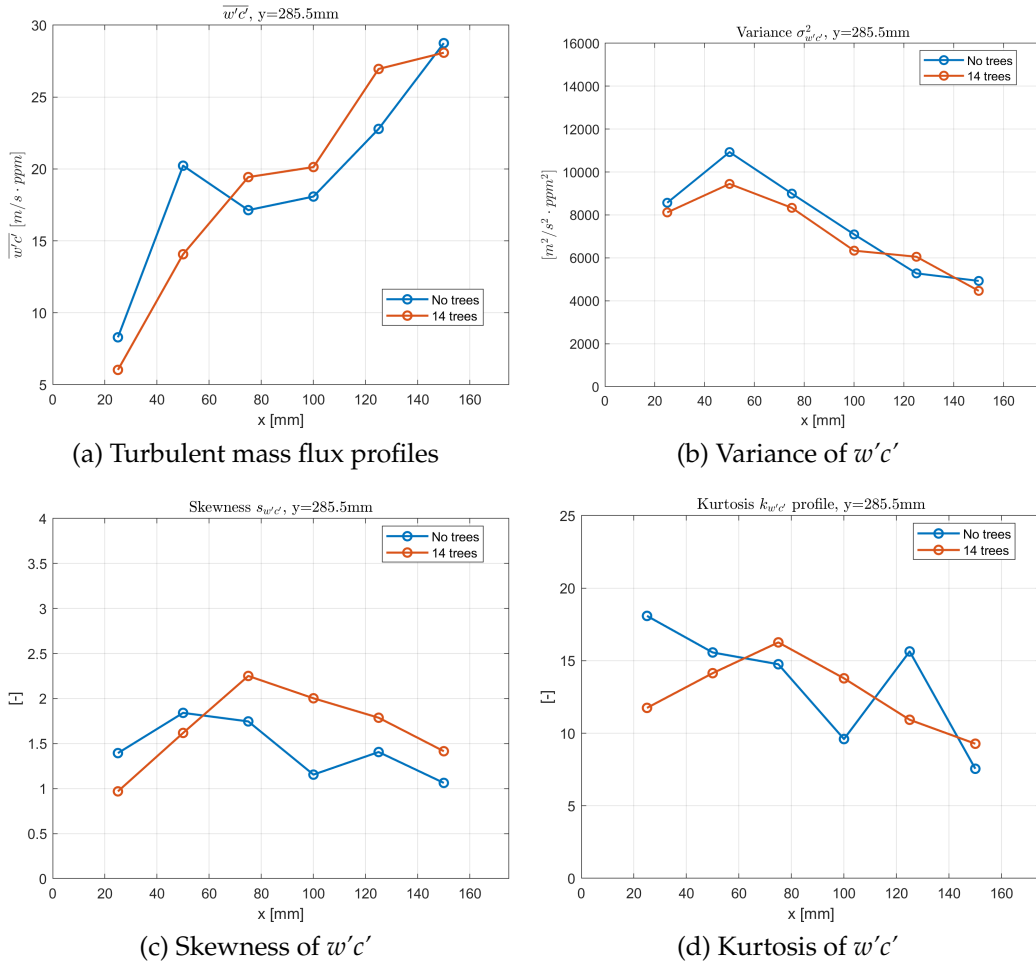


Figure 6.2: Traditional statistics of $w'c'$. All the measures are taken for different values of x at $z = 95$ mm and $y = 285$ mm.

to 29% of the total flux for the case with trees, confirming the hypothesis that turbulent structures are obstacolated by the presence of vegetation.

Another interesting effect caused by the presence of trees is the fact that the exiting flowrate (integral of the flux on the surface) is no longer constant along y direction when considering the portion of street canyon above the source; in fact, figure 6.4 shows that while for the no trees layout the integral computed on the various sections along y is almost constant, the same cannot be stated for the case with trees. The conclusion is that the presence of trees alters the bidimensionality of the setup, also in the area above the source, leading to a

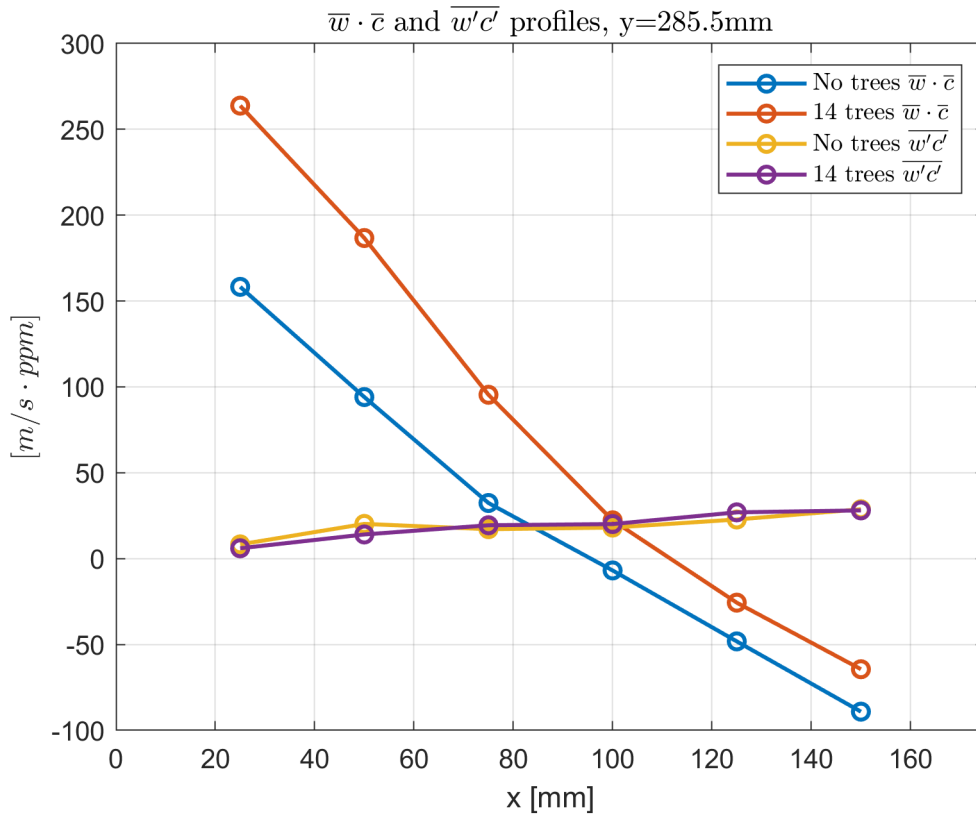


Figure 6.3: Turbulent and mean mass fluxes profiles

more intense exiting flux in the central portion of the canyon.

Figure 6.2b shows the trend of the variance of $w'c'$ signal along x ; variance tends to reduce as we move downwind, revealing a lower variability of the signal; its value, however, remains quite high with respect to the mean value $\overline{w'c'}$, indicating the fact that the signal is intermittent and characterized by frequent peaks. Variance, as the mean value, doesn't show great differences between the two analyzed cases.

Figure 6.2c shows the skewness of $w'c'$ along x ; its value is positive all along the section, but very close to 0 (especially near the canyon walls), indicating the fact that the distribution of turbulent mass fluxes is almost symmetric. Skewness is slightly higher for the case with trees, but globally the difference is not so evident as for the other statistics.

Figure 6.2d shows the kurtosis of $w'c'$ along x ; it is higher than the one of a

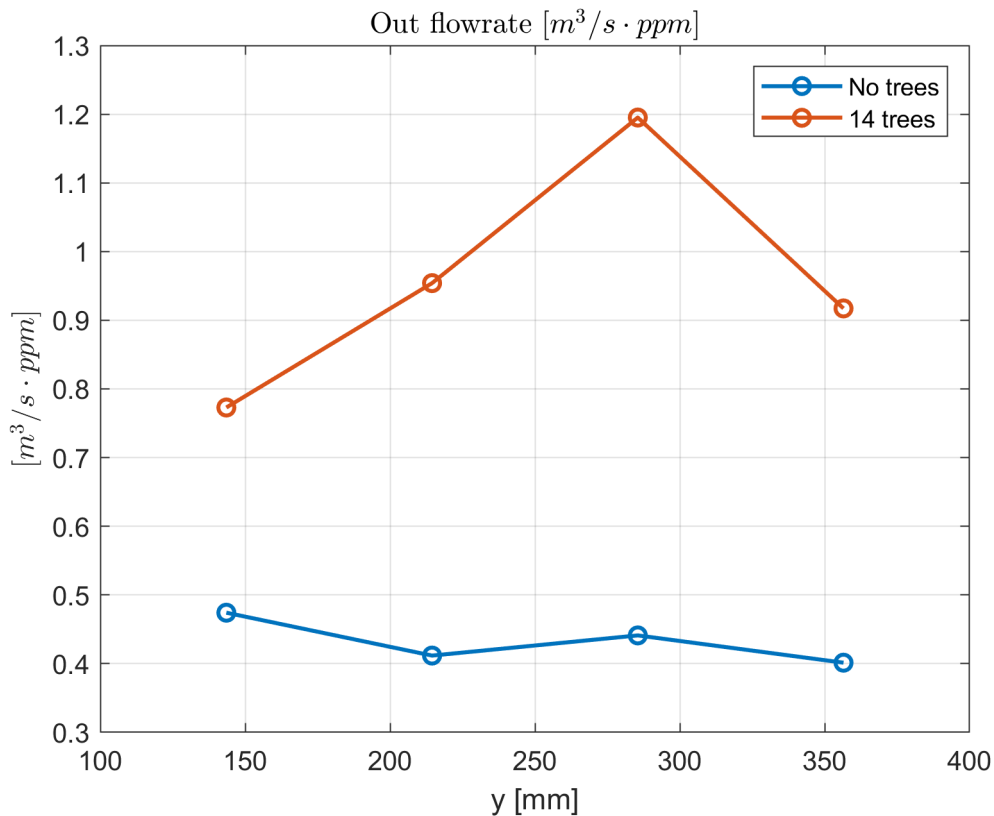


Figure 6.4: Exiting flowrate along y

Gaussian, indicating the fact that the series have heavier tails and thus a more "peaked" shape. The fact that the kurtosis is high also confirms that all the analyzed time series are quite intermittent, with frequent values that stand far away from the mean one, as already shown by the variance. Again, there are no great differences between the two layouts.

The analysis of traditional statistics has mainly highlighted general features of the turbulent mass fluxes time series, without being able though to spot differences introduced by the presence of trees. A further tool that has been adopted is the spectral analysis, which is a typical tool used to analyze the frequency content of a signal by passing from time domain to frequency domain. For the present study, the power spectral density of $w'c'$ for a given frequency can be interpreted as the intensity of turbulent structures of a certain size: the higher is the frequency, the smaller is the size of the related structure. Since

we expect to witness a reduction of the size of turbulent structures caused by trees, particular attention is given to the portion of spectra characterized by low frequencies, which is the one that indicates the presence of large size structures.

As $w'c'$ measures are characterized by a non-constant acquisition frequency, they have to be treated in a specific way also when calculating spectras, because traditional arithmetic algorithms developed for data sampled at a fixed rate cannot be adapted to LDA measures, as they are not sufficient to avoid the bias that is generated by the fact that the sampling process depends on the wind velocity. Fortunately, this problem has already been studied in the past and different solutions have been proposed; the oldest one is the slotting technique, proposed by Gaster and Roberts (1975). With this method, autocorrelation functions (we remember that the Power Spectral Density of a signal is the Fourier transform of the autocorrelation function of the signal itself) are computed as ensemble average of binned pairs of samples; binning process is performed by considering a certain $\Delta\tau$ of arrival times. Spectra computed using the slotting technique show good agreement with spectra of signals acquired at a constant rate; however, the implementation of the method is quite complex and slow.

A second proposed method is the direct method, introduced by Buchhave (1979); it consists of weighting with the residence time all statistics related to the measures characterized by non-constant acquisition frequency, including the discrete Fourier transform necessary to calculate Power Spectral Density. The implementation of this method (see Velte, George, et al. (2014) as an example) is again not so immediate and fast, but results are good since residence time weighting is mathematically the correct way to deal with the issue.

The last considered method is the Sample and Hold method; it consists in re-sampling the measurements at a constant frequency (the mean acquisition frequency), so that traditional algorithms can then be applied in order to calculate Power Spectral Density. This method is the least accurate of the three, because the re-sampling process introduces bias in the Power Spectral Density, but past studies show that this bias starts to be non-negligible only at high frequencies, especially if the re-sampling rate is high (Nobach et al. 1998, Velte, Buchhave, et al. 2014, Damaschke et al. 2018). Since for the present study we

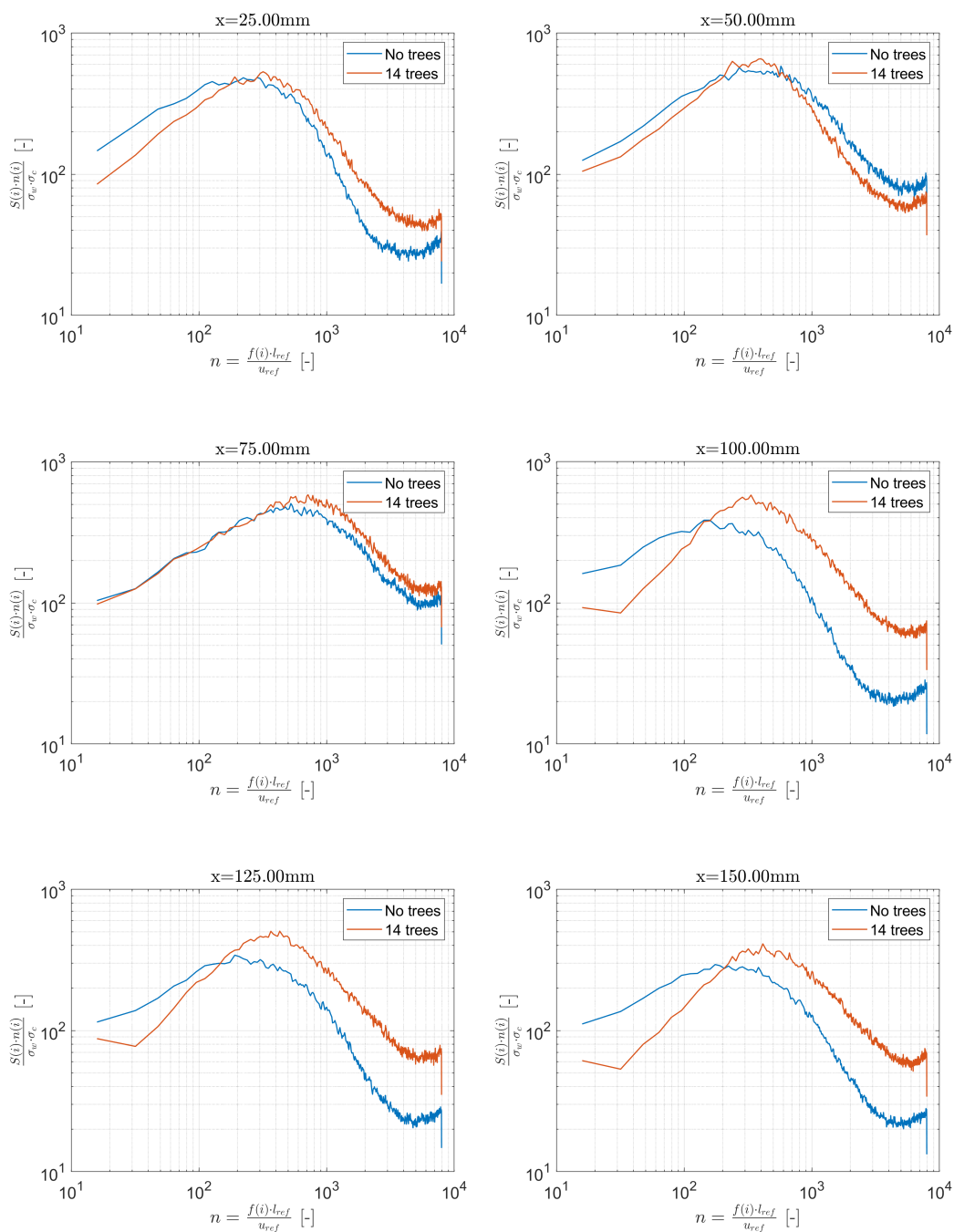


Figure 6.5: Spectra of $w'c'$

are interested in what happens to spectra at low frequencies, as mentioned before, and the average acquisition data rate is sufficiently high (> 700 Hz for all

sets of measures), we decided to adopt the Sample and Hold method for Power Spectral Density calculation, as it is simpler to implement and definitely faster than the other two proposed ones.

Moreover, the integral of the Power Spectral Density is by definition the variance of the signal; by performing the integration of the spectrum derived with the S+H method, results show that there is good agreement with the variance calculated from the original measures, as the average relative error is only 7% for the no trees case and 14% for the layout with trees, proving that the chosen method is valid.

Spectra and related frequencies are also normalized before being plotted; normalization is done in the following way for respectively frequencies and PSD:

$$n = \frac{f \cdot l_{ref}}{u_{ref}} \quad (6.4)$$

$$s = \frac{S \cdot n}{\sigma_w \cdot \sigma_c} \quad (6.5)$$

Where l_{ref} is a reference length for the setup (in this case the width of the canyon), u_{ref} is a reference velocity for the experiment (in this case the friction velocity u_*), σ_w and σ_c are vertical velocity and concentration standard deviations.

Results are presented in figure 6.5: each plot corresponds to the spectrum of the set of measures taken in one specific point along x on the $y = 285.5$ mm section. From the graphs it is possible to see that the presence of trees tends to shift the PSD to higher frequencies, leading to a reduction of the contribution of low frequency components to the vertical turbulent mass flux; high frequency components, associated to turbulent structures of small scale, become thus the main responsible for the turbulent mass exchange between the canyon and the Atmospheric Boundary Layer when trees are present. Moreover, the reduction of the PSD in the low frequencies region becomes more evident as we move towards the downwind wall; this can be explained by the fact that as we get closer to the downwind wall, turbulent fluxes become more important and turbulent

structures start to get bigger, as explained in Chapter 5 (i.e. figure 5.1). The reduction of the size caused by trees is witnessed mainly there for this reason, because it is the area where turbulent structures of big size are present and can thus be affected by trees (close to the upwind wall, in fact, the shear layer still has to develop, and also for the configuration without trees turbulent mass flux is very small and characterized by small scale vortices).

6.2 Complex network analysis

Network science is a new approach to research that has developed in the last two decades, which is becoming more and more relevant thanks to the fact that it can be applied to many fields of research, and thanks to its suitability to describe any discrete system. For the present study, network analysis has been used as an alternative tool with respect to traditional statistics to grasp the characteristics of turbulent mass flux and to highlight differences between the two examined layouts. In the following sections, a general introduction on complex networks, network mathematic formulation and network metrics is provided, together with an overview of the main fields of application of network science; finally, results of the analysis applied to turbulent mass fluxes are presented.

6.2.1 Introduction

Originally, the first applications of networks were social networks, developed to catch all the connections between individuals in order to understand which were the effects of such relationships on the society; this happened back in the 1920s, but it is necessary to wait until early 1990s to start finding applications in other disciplines, in particular the physics-related ones. Moreover, in the last few years network science has experienced a huge growth thanks to the evolution of computation systems, which allow to model complex networks of great dimensions (millions of nodes) and to calculate the related metrics in a more efficient way and in a lower amount of time. Networks are created in order to describe geometrically all the elements of a system and the relationships that occur between them; complex networks, however, are particular networks that

are formed from real-world systems, which show non-trivial features and complexity (Iacobello 2020).

The main fields that have taken advantage of the tools of network sciences are the following (for further details, see F. Costa et al. (2011)):

- **Biological networks:** related to biomolecular analysis, neuroscience and general medicine. In particular, for general medicine, network analysis is very useful to understand how general diseases spread around the world, as well as to understand brain functions, evolution and connections in the neuroscience field;
- **Physical and Engineering networks:** many physical and engineering fields can take advantage of network science. In particle physics and chemistry, for example, networks can highlight interactions between molecules; considering earth sciences, climate networks are widely used to analyze climate dynamics, in particular long range effects and global changes in climate dynamics.

Talking about engineering, computer sciences and internet systems, transportation and electric systems are the areas where complex networks are most commonly found. Computer sciences and the internet have an intrinsic web-like structure, which can be easily converted into a network, giving thus the opportunity to be analyzed with an approach that fits very well their inner structure. Transportation systems take advantage of network science especially for improving their efficiency (e.g. airport transportation, where flights and airports can be identified with links and nodes of a network) and accessibility (e.g. road networks, which can be used as a mean to understand how to improve traffic in a city).

Electric systems can also be described with a network approach, as they are made of several transmission lines which can be easily converted into networks in order to highlight weaknesses of the system itself;

- **Social and Economic networks:** social activities, such as sports, tourism, politics, may take advantage of complex networks, since all these are fields where interactions play a very important role and, for this reason, their

analysis through networks is appropriate. Economic studies are also suitable for complex network analysis, because there is a very high amount of detailed data (needed for an accurate network formulation) and because also these systems are composed of people who interact one with the other.

Besides all these possible applications in different fields, the interest for the present study is on fluid flows; complex networks have already been employed in fluid mechanics in the past decade, but still it is a very new approach and only few problems have been tackled. In particular, time series from turbulent jets measures represent the most studied topic: Charakopoulos et al. (2014) used complex network analysis to separate different regions in a turbulent heated jet, by comparing results obtained at different spatial points within the jet; they also found correspondence between the minimum value of the network metrics and the jet axis. Manshour et al. (2015) studied acceleration series in a helium turbulence, while Murugesan, Zhu, et al. (2019) analyzed the synchronization of a hydrodynamically self-excited jet, using different metrics to find the route to synchronization.

Another topic recently addressed using a network approach is the one of reacting flows; dynamical transition from stable operation to thermoacoustic instability in a turbulent combustor has been studied by Unni et al. (2018), while unsteady pressure time series in a combustor have been analyzed by Murugesan and Sujith (2015).

Turbulent transport of a scalar (same topic of the present study) has already been studied by Iacobello, Marro, et al. (2019); in particular, the dynamics of a passive scalar plume in a turbulent boundary layer have been analyzed using different network metrics, which showed that a stronger meandering motion of the plume is associated to higher values of these metrics. Also the weakening of the plume as the distance from the source increases is captured by network metrics.

Wall-bounded turbulence has also been tackled by Iacobello, Scarsoglio, and Ridolfi (2018), studying through complex network metrics the spatio-temporal features of the velocity field of a fully developed turbulent channel flow. A

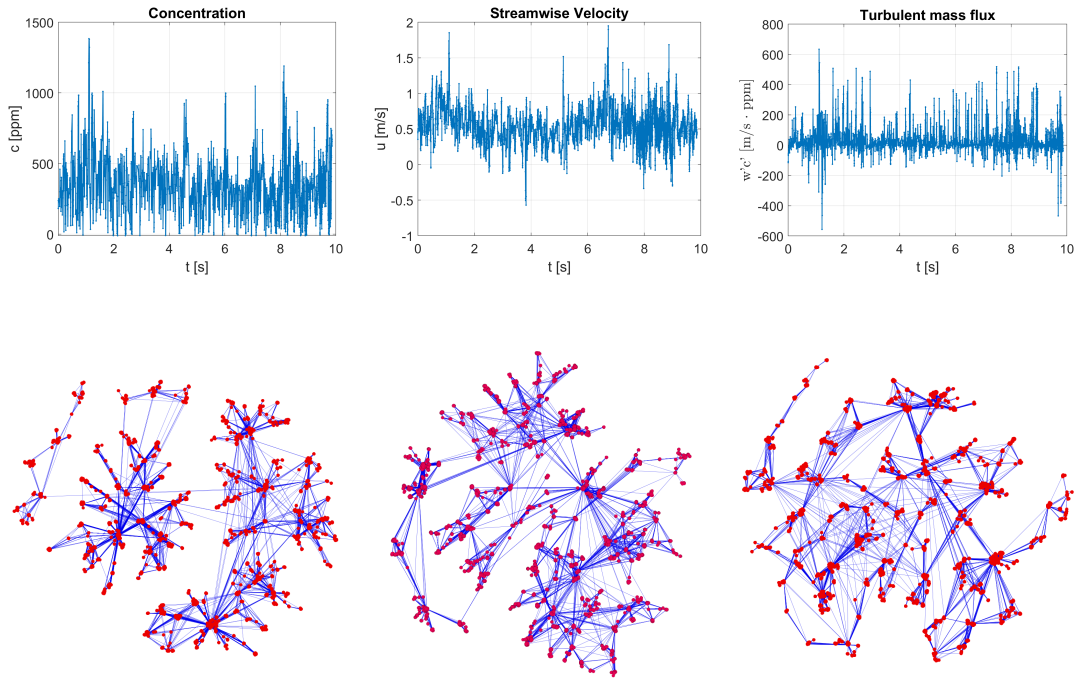


Figure 6.6: Examples of time series (top) and corresponding networks (bottom), generated with the visibility algorithm, for concentration, streamwise velocity and turbulent mass flux

turbulent channel flow is also studied by Jacobello, Scarsoglio, Kuerten, et al. (2018), with two spatial networks generated from streamwise and wall-normal velocity components; particular attention is given to long-range links, able to identify temporal persistence of defined velocity patterns (high and low speed streaks).

6.2.2 Network mathematical formulation

A network can be defined as a graph $\mathcal{G} = (\mathcal{N}_v, \mathcal{N}_e)$ consisting of a set of nodes (\mathcal{N}_v , also called vertices) and a set of links (\mathcal{N}_e , also called edges); the topology of the network is the structure obtained through the interactions between nodes, which can also be plotted thanks to dedicated softwares (figure 6.6). Nodes can represent different features of the system, depending on how the problem is approached (see section 6.2.3): time instants, states of the system, spatial locations, Lagrangian particles. Networks, however, are classified depending on

how links are defined; they can either be:

- **Weighted:** if links have an intensity (a scalar that quantifies the intensity of the link), they are not all equal and the network is said to be weighted;
- **Unweighted:** if links do not have an intensity and are all equal the network is said to be unweighted;
- **Directed:** if links have a direction from one node to the other (and thus represent a transition from a state to another for example);
- **Undirected:** if links do not have directions.

For the present study, the analyzed networks will be of the unweighted and undirected type.

Mathematically, each network can be represented through a matrix, called adjacency matrix, which explicits the relationship between nodes; each entry of the adjacency matrix is defined as follows:

$$\mathcal{A}_{i,j} = \begin{cases} 1 & \text{if nodes } \{i, j\} \text{ are linked} \\ 0 & \text{otherwise} \end{cases} \quad (6.6)$$

Where $i, j = 1, \dots, N$ indicate the nodes; the matrix is thus a complete way to take into account all the possible interactions that can be present in a network. If the network is weighted, the adjacency matrix is replaced by the weight matrix $\mathcal{W}_{i,j}$, where each entry is not only either 0 or 1, but is a real number corresponding to the weight of the link that joins node i with node j . When the network is undirected the adjacency (or weight) matrix is symmetrical ($\mathcal{A}_{i,j} = \mathcal{A}_{j,i}$ or $\mathcal{W}_{i,j} = \mathcal{W}_{j,i}$).

Weights are normally assigned to links in order to quantify the intensity of the relationship between different nodes, but there are some particulare cases where weights can be assigned also to nodes, namely the ones where nodes represent an heterogeneous set of entities and it is useful to make a distinction between them according to their nature.

If $\mathcal{A}_{i,j} = 1$ then nodes i and j are said to be adjacent; given a node i , the set of all the nodes adjacent to i forms what is called the first neighbourhood of i :

$\Gamma^1(i)$. Conversely, all the members of the first neighbourhood of i are called first neighbours of i .

Complex networks can also be classified as either static or dynamic; static networks are the ones which do not evolve in time (for example, the ones related to a stationary process), while dynamic ones are the one where links or nodes (or both) change as time goes on (for example, the ones related to transient phenomena).

6.2.3 Network types and construction

The aim of network analysis, especially when applied to fluid flow dynamics, is to extract useful and non-trivial information from data measured on the field; according to the structure of the available data, three different ways to approach the problem have been explored:

- **Time series analysis:** with this approach, nodes correspond to single time instants or groups of time instants; measures are taken in a single position in space and the focus is on the temporal behaviour of a certain quantity;
- **Spatial networks:** with this approach, nodes correspond to specific positions in the space; in this case, the focus is on the spatial behaviour of a certain measured quantity;
- Both time series and spatial networks can be built also from a Lagrangian point of view, where particle trajectories are exploited to build networks; in this case, the focus is on the particle motion either in time or space.

For the present study, time series analysis is performed, since each coupled LDA-FID measure represents the behaviour of turbulent mass flux $w'c'$ in a certain point for a determined period of time. For each spatial point, a network is built with the measures, and then the behaviour of network metrics is studied as the spatial location considered changes (along the wind direction).

There are three main different ways to create networks starting from time series:

- **Proximity networks:** the time series is divided into different sub-intervals, which are called *state vectors* as they are representative of a state of the system; for this reason they represent the nodes of the network. Links are activated if there is a sufficiently high correlation between the nodes, which represent states of the system (in this case, we talk of correlation-based proximity); alternatively, state vectors are placed into a phase space and links are activated if two states are sufficiently close in the phase space (in this case, we talk of recurrence-based proximity);
- **Transition networks:** with this approach, each node corresponds to a discrete state of the system (which can be defined by a sub-interval of the time series); links between nodes are active if there is a non-zero probability that one node is immediately followed by the other node in time. As a result of this process, networks are directed and links are weighted (the weight of each link is the value of the probability mentioned before). Mathematically speaking, this approach corresponds to a Markovian process, with given transition probabilities between different discrete states;
- **Visibility graphs:** it is a geometrical approach for building networks from time series. In this case, each single time instant corresponds to one node, and links are active depending on a convexity criterion (in this case we talk of natural visibility graphs) or on a more simple ordinal criterion (in this case we talk of horizontal visibility graphs). This results in an undirected network, which can though be either weighted or unweighted; another important characteristic is that this is a non-parametric formulation, since no parameters are needed to define nodes, whereas for the other two criteria each node (state) has to be defined, and the definition usually involves several arbitrary parameters.

For the present study, the visibility algorithm has been used, thanks to its immediateness and to the intrinsic simplicity brought by the absence of parametrization. In the following section, the visibility algorithm is explained with more details.

6.2.4 Visibility graphs

Visibility graph is a geometrical method adopted to generate networks from measured time series. The method was proposed by Lacasa et al. (2008) and is based on a convexity criterion: two elements $(s(t_i), s(t_j))$ of a time series $s(t_n)$, $n = \{1, 2, \dots, N\}$ are connected in the network if the following condition is satisfied:

$$s(t_k) < s(t_j) + (s(t_i) - s(t_j)) \cdot \frac{t_j - t_k}{t_j - t_i} \quad (6.7)$$

This must hold for every t_k between t_i and t_j ; in this case, it is said that the two points i and j have visibility. The procedure is shown in figure 6.7, and geometrically it states that two nodes are connected if the straight line that joins them does not intercept any other value of the time series itself. From this definition, it is also clear that visibility graphs are undirected and unweighted networks.

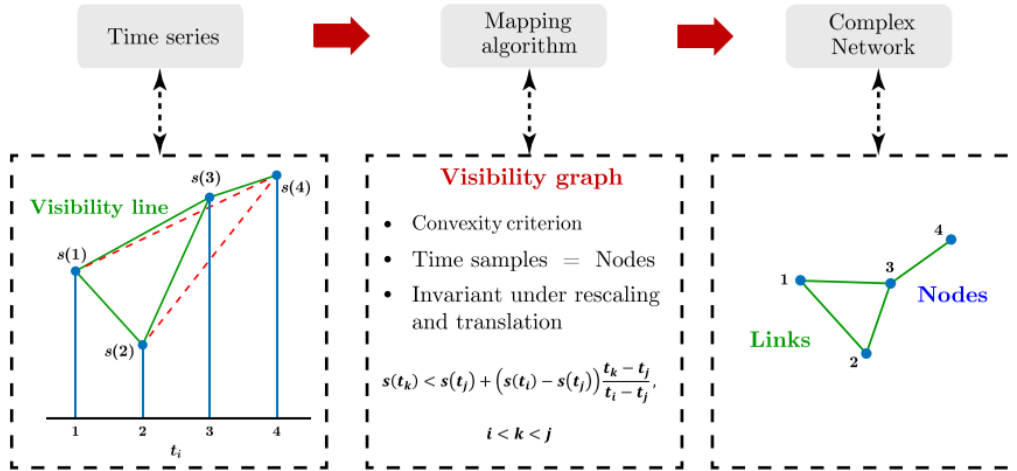


Figure 6.7: Building process of a network from a time series with the visibility algorithm

The main alternative to natural visibility criterion is the horizontal visibility, which considers only horizontal lines between data; two nodes have horizontal visibility if the following condition is satisfied:

$$s(t_k) < \min[s(t_i), s(t_j)] \quad \text{for any } t_j < t_k < t_i \quad (6.8)$$

It is a simpler criterion, which however provides different results in terms of network metrics with respect to natural visibility networks; for further applications of horizontal visibility graphs, see Luque et al. (2009) and Manshour et al. (2015).

The main advantage of visibility algorithm with respect to proximity or transition algorithms is the fact that it does not need any parametrization; in fact, each instantaneous value of the time series represents a node and for this reason no grouping of values is necessary (while for the other methods, nodes are generated from sub-intervals of the whole time series, and the splitting procedure always requires parameters that need to be defined). Another feature, which can be either an advantage or a disadvantage according to the kind of study that is being performed, is that visibility graphs are invariant under rescaling and translation both on horizontal and vertical axes. This means, for example, that two time series with the same shape but different mean value and variance will result in the same network; if the study must be sensitive to rescaling and to the actual values of the time series rather than to the geometrical shape and features of the series, invariance is a big drawback, but if the focus is on the structure of the series, invariance is an advantage because no normalization of the series is needed.

Another advantage of the visibility algorithm has emerged from the present study, which involves a non-constant frequency data acquisition; it is the fact that even if the sampling process is not characterized by a constant acquisition frequency, the visibility algorithm can be directly applied to the original data, without the need of re-sampling or particular other treatments. This is a great advantage, especially after seeing all the care that must be put into data processing when computing traditional statistics and spectra from these particular sets of data.

6.2.5 Network metrics

Once the network has been built, metrics are necessary for a detailed analysis of its features; the behaviour of the metrics can be linked to the topological structure of the time series, which in turn reflects the physical phenomenon that is being considered and described by the network. It is thus possible, by selecting the most relevant metrics, to describe specific features of the physical phenomenon using network metrics rather than traditional statistics. The choice of the best metrics to describe the system is not a trivial task, which has to be accomplished according to the way the network has been built.

There are different types of network metrics, which describe different characteristics of the network; metrics can be referred to single nodes or to the whole network (either directly or as an average of metrics referred to single nodes). In the following section, a description of the metrics adopted for the present study is provided. It has to be noted, however, that not all the chosen metrics provide relevant results and show interesting features that can be related to the physics of the turbulent mass transport and the influence of trees on it; still, all of them have been analyzed because the application of network science to this field is new and it was not possible to understand a-priori from other previous works if a certain metric would have been useful or not. For a more complete set of metrics that can be used in network science, see Iacobello (2020).

Connectivity metrics The most simple way to analyze a complex network is to study how many connections each node activates. Connectivity metrics, thus, can be interpreted as an index of centrality, since the higher is the number of links activated by a node, the higher is its importance in the network. The definition of connectivity metrics depends on whether the network is weighted or unweighted, meaning that there are specific metrics for each type of network; for the present study, only unweighted networks are analyzed, so the metrics here described are related to this type of network.

- **Node degree** $\mathcal{K}(i)$: it is defined as the number of nodes connected to node

i :

$$\mathcal{K}(i) = \sum_{j=1}^{\mathcal{N}_v} \mathcal{A}_{i,j} \quad (6.9)$$

It is the simplest way to determine the index of centrality of a node. This measure can be averaged on the whole network as:

$$\bar{\mathcal{K}} = \frac{1}{\mathcal{N}_v} \sum_i^{\mathcal{N}_v} \mathcal{K}(i) \quad (6.10)$$

Which is a measure of the average number of links that a node activates in the network;

- **Network density \mathcal{Q}** : it is defined as the ratio between the number of links and the total possible number of links in the network:

$$\mathcal{Q} = \frac{2\mathcal{N}_e}{\mathcal{N}_v(\mathcal{N}_v - 1)} = \frac{\bar{\mathcal{K}}}{\mathcal{N}_v - 1} \quad (6.11)$$

It is a measure of the sparsity of the network; this metric, however, is usually very small and not suitable for comparisons when dealing with real-life systems, which are composed of a high number of nodes and thus a very high number of possible links;

- **Probability distributions**: these are not a specific tool of network science, but they can be used to further investigate the behaviour of node-related metrics. The most common analysis regards the probability distribution of node degree $\mathcal{K}(i)$, but in principle the PDF of all node-related metrics can be analyzed.

Distance-based metrics Distance-based metrics, as connectivity metrics, are defined according to the way the network has been built; if the network describes a time series (as in the present work), these metrics are related to the temporal distance between peculiar events highlighted by the network topology, while if the network is a spatial network, these metrics are related to the spatial distance between points where peculiar events occur.

- **Mean link length** $d^t(i)$: it is defined as the mean temporal distance between node i and its first neighbours:

$$d^t(i) = \frac{1}{\mathcal{K}(i)} \sum_{j=1}^{\mathcal{N}_v} \mathcal{A}_{i,j} |t_j - t_i| \quad (6.12)$$

This metric can be also averaged on the whole network:

$$\bar{d}^t = \frac{1}{\mathcal{N}_v} \sum_i^{\mathcal{N}_v} d^t(i) \quad (6.13)$$

Which is the average temporal distance between a node and its first neighbours in the network;

- **Average peak occurrence** Φ : it is defined as the inverse of the average mean link length, and it is useful to highlight small values of the average mean link length through a frequency measure:

$$\Phi = \frac{1}{\bar{d}^t} \quad (6.14)$$

Its name derives from the fact that it is a useful metric to capture the frequency of extreme events in the time series.

Clustering metrics Besides two-nodes relationships (which characterize connectivity metrics), also three-nodes relationship are an important feature of networks. In particular, a triple is a set of three nodes in which at least two of them are directly linked; a triangle, on the other hand, is a set of three nodes all connected between them. Based on these two definitions, the most important clustering metrics are:

- **Transitivity** \mathcal{T} : it is a metric related to the whole network, defined as the ratio between the total number of triangles and the total number of triples present in the network:

$$\mathcal{T} = \frac{3\mathcal{N}_{\Delta}}{\mathcal{N}_{\wedge}} \quad (6.15)$$

The factor 3 in the numerator takes into account the fact that in every triangle there are 3 triples, and allows transitivity to be a coefficient comprised between 0 and 1;

- **Clustering coefficient $\mathcal{C}(i)$** : it is a node-related metric, defined as the ratio between the triangles and the triples in which node i is involved:

$$\mathcal{C}(i) = \frac{\mathcal{N}_{\Delta}(i)}{\mathcal{N}_{\wedge}(i)} \quad (6.16)$$

It is possible also to calculate the average clustering coefficient for the whole network as:

$$\bar{\mathcal{C}} = \frac{1}{\mathcal{N}_v} \sum_i^{\mathcal{N}_v} \mathcal{C}(i) \quad (6.17)$$

Although it is conceptually similar to the transitivity, the average clustering coefficient is biased by low degree vertices, because the contribution of the clustering coefficient of each node to the average clustering coefficient has the same weight (thus nodes with low degree/centrality give the same contribution of nodes with high degree/centrality), while for the transitivity it is directly counted the total number of triples and triangles, without considering the nodes to which they belong. As a result, the contribution of low-degree nodes is more evident in the average clustering coefficient.

Assortativity measures Assortativity is defined as the tendency of nodes to link with similar nodes; similarity is usually measured through a connectivity metric such as the node degree. If nodes tend to link with similar nodes, the network is said to be assortative; if nodes tend to link with dissimilar nodes, the network is said to be disassortative; if nodes do not have a tendency to link neither with similar nor with dissimilar nodes, the network is said to be non-assortative.

- **Pearson assortativity coefficient r** : it is defined as the Pearson correlation

coefficient of the degree of the nodes at the ends of each link:

$$r = \frac{\text{cov}[\mathcal{K}(i), \mathcal{K}(j)]}{\sigma_{\mathcal{K}(i)} \cdot \sigma_{\mathcal{K}(j)}} \quad \forall \{i, j\} \text{ so that } \mathcal{A}_{i,j} = 1 \quad (6.18)$$

Assortativity is thus measured by a scalar; since it is a correlation coefficient, its value will be between -1 and 1. If the network is assortative, r will be positive; if the network is dissortative, r will be negative; if the network is non-assortative, r will be null (or close to 0).

In the next section, results of the analysis of the metrics related to time series of $w'c'$ are provided.

6.2.6 Results

The analysis on the time series of turbulent mass flux $w'c'$ has been performed on each point along x on the central section ($y = 285.5 \text{ mm}$) as for traditional statistics; all the metrics mentioned in section 6.2.5 have been calculated and plotted, in order to see their trend and search for differences introduced by the presence of trees. The visibility algorithm and the metrics related to the network allow to characterize the original time series especially in terms of peaks and irregularities; a peak is defined as a point of the times series which is a local (or global) maximum, with order of magnitude comparable with the maximum excursion of the series $\Delta s = (\max[s(t_i)] - \min[s(t_i)])$. Irregularities instead can be defined as temporal variations with order of magnitude much smaller than Δs , but sufficient to decrease the visibility of the surrounding points; in other words, they are a sort of noise present on the signal which reduces the visibility, especially at medium range. It has to be noted that the visibility algorithm is able to highlight only positive peaks, but not negative ones (named *valleys* or *pits*). For this reason, if a series exhibits mainly pits or if we want to check the symmetry of the series itself, it is necessary to study not only $+s(t_i)$ but also $-s(t_i)$; the comparison between the behaviour of the metrics of $s(t_i)$ and $-s(t_i)$ will provide a complete analysis.

For the present study, the interest goes mainly to peaks and pits rather than to irregularities; this is due to the fact that peaks in the $w'c'$ time series can be

associated to the presence of turbulent structures of large size, allowing thus to link the physical phenomenon to the behaviour of some metrics, while no direct relationship has been found between irregularities of the time series and the physical phenomenon.

Figure 6.8 shows the trend of the various metrics along x direction. Starting from the average node degree (figure 6.8a), it is possible to see that it remains almost constant along x , and nearly no differences are visible between the two setups. Network density (figure 6.8b) shows some differences between the two cases, but the values are so small that probably the differences are caused by the very high number of nodes of each network, which makes this metric non-suitable for comparisons. Globally, thus, connectivity metrics are not so useful to describe the characteristics of turbulent mass transport.

Figure 6.8c shows the behaviour of transitivity; this metric can be interpreted as a measure of the irregularities of the time series, because it is much more affected by the presence of small irregularities rather than by the presence of peaks. In fact, given a node i and a couple of nodes $\{j, k\} \in \Gamma^1(i)$, which always form a triple with node i , a triangle is much more likely to be formed if nodes $\{j, k\}$ are separated by short time intervals (because when nodes are far in time there is a much higher probability that an intermediate node will obstruct their visibility); since irregularities tend to reduce the visibility in the short and medium range, the number of triples that also form a triangle in a regular time series is higher than the number of triples forming a triangle in a more irregular time series. Consequently, a low transitivity is a signal of irregularity of the series, and when comparing two series, the one with higher transitivity is the more regular one. When applied to flow dynamics, transitivity can be interpreted as a measure of the fluctuation level of the time series; for the present study, transitivity slightly increases while moving downwind for both setups, showing thus that turbulent mass flux evolves while moving towards the downwind wall. Again, no significant differences can be seen between the two cases, although the presence of trees seems to introduce a higher level of irregularity in the series, which can thus be related to smaller scale turbulent structures.

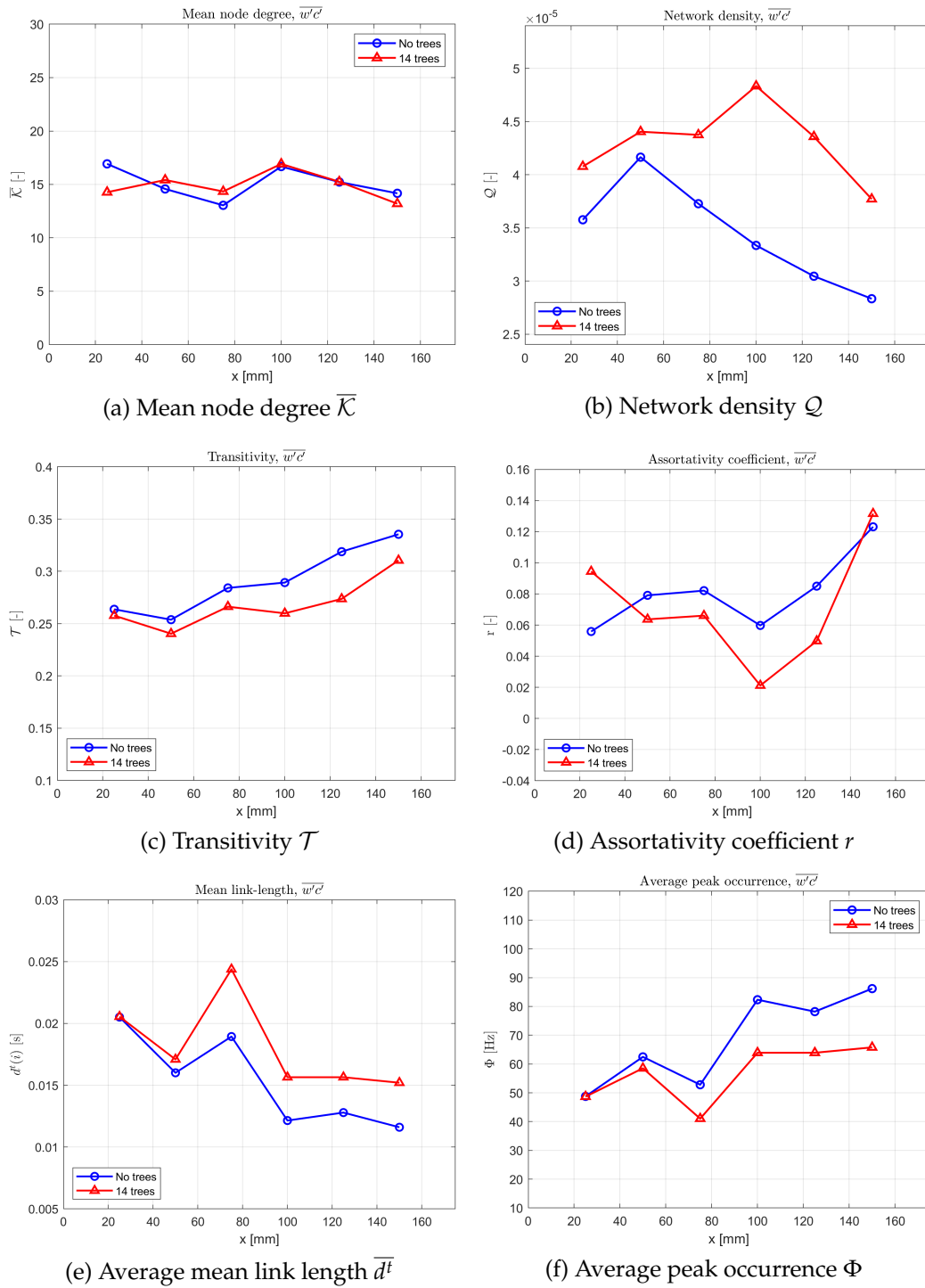


Figure 6.8: Network metrics from $w'c'$ time-series

Figure 6.8d represents the behaviour of the assortativity coefficient; assortativity can be interpreted as a measure of the intensity of the peaks with respect to the other values of the series. In fact, if r is highly positive it means that nodes tend to link with nodes of similar degree, indicating the fact that peaks are not pronounced with respect to the other values of the series, while if r is highly negative it means that the network is disassortative and nodes tend to link with nodes characterized by very different degree; this means that peaks (nodes with high centrality) are much more prominent than the rest of the measures (which have low centrality), and can thus be considered outliers (very large values with respect to a local subset of data). In our case, however, assortativity is very close to 0 for both setups, and for this reason it doesn't provide useful information on the time series, since networks can be considered almost non-assortative.

Finally, figure 6.8e and figure 6.8f show the average mean link length and the average peak occurrence respectively. Mean link length (and consequently average peak occurrence) can be interpreted as a measure of how far peaks are in the time series; in fact, peaks are high values that inhibit the long-range visibility between points, leading to a lower value of the average mean link length. For this reason, a series with a high number of peaks will have lower average mean link length and higher average peak occurrence with respect to a series where peaks are less frequent. In other words, these two metrics can be interpreted as a measure of the horizontal separation between peaks. Average peak occurrence increases consistently when moving along the wind direction, showing a much higher frequency of peaks when close to the downwind wall; this is due to the fact that peaks can be associated to turbulent structure of large size in the shear layer, which develop more frequently in the area close to the leeward wall. Moreover, these metrics are the ones that show the biggest difference when trees are introduced; in fact, while for small x values the two cases almost overlap, for high x values the difference is definitely non-negligible, showing that peaks are much less frequent when trees are present. This confirms the fact that the presence of trees reduces the size of turbulent structures, as already highlighted by spectra of $w'c'$, and that this effect is more evident where large structures are more present, namely close to the downwind wall.

As a conclusion, we have shown that network metrics are able to highlight

the same important features of the studied time series of turbulent mass flux as traditional statistics and spectra of the signal, but with a completely different approach. In particular, the most meaningful metrics for this particular studied phenomenon are the transitivity and the mean link length/average peak occurrence.

7. Conclusions

The aim of the present thesis was to assess the effects of vegetation on vertical mass exchange velocity u_d in a long street canyon. To do so, concentration and wind velocity measures have been taken and analyzed, in order to see the impact of the presence of trees also on each of these quantities. Results have shown that the average concentration of pollutants inside the street canyon increases with the presence of trees; concentration at the rooftop is also higher in the setup with trees. On the other hand, vertical wind velocity at the rooftop tends to reduce slightly. Considering mass fluxes at the top of the canyon, the turbulent ones remain almost unchanged, while the mean ones increase significantly with trees, leading to a total exiting flux that is higher when trees are present. Finally, u_d is found to be increased in the configuration with trees.

Another significant achievement has been the discover that the presence of trees alters the bidimensionality of the experiment. While in the no-trees configuration vertical mass fluxes exiting from the rooftop of the canyon are almost constant along the length of the control volume, in the presence of trees they tend to be much higher in the central portion of it. Also concentration measures inside the street canyon show the same result, but with opposite trend: concentrations are higher in the outer sections of the control volume and lower in the central ones.

These results, however, have to be verified through further experiments. The loss of bidimensionality may be due not only to the presence of trees, but also to the fact that the source cannot be considered infinitely long with respect to the control volume. For this reason, it is possible that concentrations are influenced by the edges of the source when trees are present, leading to biased results and, possibly, to different outcomes regarding u_d . Also, since lateral fluxes haven't

been measured, it is not possible to state with absolute certainty that the measures of the vertical flux are sufficiently accurate. For this reason, additional flux measures should be taken after closing the control volume on its lateral sides, in order to be totally sure that all the tracer gas emitted by the source exits from the roof of the canyon. In this way it is possible to estimate the error that is made by using the current measurement grid and thus decide if it is sufficiently refined.

Flux measures are in fact the most difficult part of the experiment, since they are influenced by many variables and it is hard to build an experimental setup where the presence or absence of trees is the only relevant one. Moreover, also data acquisition and data treatment are quite long and complicated, making it hard to collect big amount of information.

Further concentration measures inside the canyon with different measurement grids should also be performed, in order to have a more refined concentration map inside the control volume and to better understand how the presence of trees influences it, even if the available measures are already sufficient to see the effects that trees have on the average concentration. In particular, measurements as close as possible to trees and between trees and canyon walls are those that are likely to be the most relevant ones, as concentrations are expected to rise significantly when close to those elements.

Due to these reasons, all the measures and results regarding the vertical mass exchange velocity have to be considered preliminary, thus very useful to obtain a first overview of the topic and to understand which are the criticalities of the experiment, but not to be considered definitive.

A further analysis on the time series of turbulent mass fluxes $w'c'$ measures has been carried out, with the aim of better understanding which impact vegetation has on them, as well as introducing complex network analysis as an alternative way to treat fluidodynamic data. Measures have shown that turbulent mass fluxes remain almost constant when trees are introduced, but since the mean flux increases, their importance reduces, passing from 45% to 29% of the total exiting flux. Moreover, traditional statistics and spectra of the signal show that the presence of trees reduces the size of turbulent structures in the shear layer, confirming that turbulent fluxes are obstructed by vegetation.

The same results are obtained with the completely different approach of complex networks, exploiting several network metrics that are able to highlight the important features of $w'c'$ time series in the same way as traditional statistics.

Considering a more general aspect, the results obtained with the present thesis can be useful to city planners in order to implement vegetation in urban canyons. When dealing with the average concentration inside the street canyon, results are in line with previous studies and show that it increases when trees are present. This fact implies that in those streets where vehicular traffic is expected to be significant, trees should not be planted, or at least not in a dense configuration. It is preferable to project small green areas (such as parks for example) surrounding those roads, so that vegetation can still help against the urban heat island effect without reducing the removal of pollutants from the streets where they are generated.

City planners have also to keep in mind that all these considerations are valid for a wind direction perpendicular to the street axis. For this reason, it is important that they know in advance which are the main wind directions affecting a certain street, in order to know how much the previous considerations have to be taken into account. In fact, the impact of vegetation on the average concentration decreases as the wind direction passes from perpendicular to parallel with respect to the street axis. It is thus possible to be more flexible in the design of the vegetation of a street when dealing with one characterized by parallel wind rather than with another where wind is perpendicular most of the time.

When dealing with mass fluxes and exchange velocity u_d , on the other hand, since the measures and the results obtained have to be considered preliminary and need to be verified through further experiments (as explained in chapter 5 and in the previous paragraphs), it is not possible yet to provide definitive and useful advices to urban planners. However, if these results are confirmed, they show how the presence of trees reduces the lateral flux of mass, making all the produced pollutants exit vertically from the canyon rather than diffusing also laterally. In this way, a possible advice could be to place trees in those portions of streets where it is better not to have diffusion of pollutants along the street itself. An example could be a street partially accessible by cars and partially

pedestrian, where it would be better for human health not to have the pollutants produced by cars to be transported in the pedestrian part of the street. Average concentrations would be higher in the portion of street where trees are present, but pollutants would be transported much less in the pedestrian area of the road.

The candidate had the opportunity of directly using both the Flame Ionization Detector and the Laser Doppler Anemometer for concentration and wind velocity measures, understanding the experimental protocol necessary for their correct operation and the main issues related to windtunnel measurements. Data processing has been done using mainly the Matlab environment, allowing the candidate to treat the big amount of information coming from the field and to extract useful results from them. Also bibliographic research has been done, to clarify the context of the experiment, analyze previous studies on similar topics and also to provide detailed information on how to treat the particular data coming from coupled LDA-FID measures, especially regarding the spectrum of the signal.

Originally, the experimental campaign was supposed to study more configurations, changing the density of trees in the street canyon, in order to have a more detailed analysis of the effect of vegetation. Unfortunately, after approximately five weeks of experiments, an electronic component of the windtunnel broke and due to the complex pandemic situation it was not possible to repair it until few weeks ago. For this reason the present thesis includes only two configurations, the one without trees and the one with trees, which originally should have been the densest one. However, this fault gave the candidate the opportunity to work also on the analysis of time series, topic that otherwise wouldn't have been addressed in the present thesis, giving thus a more complete overview of the available measures.

Besides all the measures mentioned earlier, needed to validate the results obtained so far, future studies on this topic should be focused on intermediate tree density configurations, with the main aim of understanding if there is a threshold under which the presence of trees becomes negligible or not.

Bibliography

- Ahmad, K., M. Khare, and K.K. Chaudry (2005). "Wind tunnel simulation studies on dispersion at urban street canyons and intersections - a review". In: *Journal of Wind Engineering and Industrial Aerodynamics* 93, pp. 697–717.
- Beckett, K.P., P.H. Freer-Smith, and G. Taylor (2000). "Particulate pollution capture by urban trees: effect of species and windspeed". In: *Global Change Biology* 6, pp. 995–1003.
- Bhargava, A., S. Lakmini, and S. Bhargava (2017). "Urban Heat Island Effect: Its Relevance in Urban Planning". In: *Journal of Biodiversity & Endangered Species*.
- Boussinesq, M.J. (1897). *Théorie de l'écoulement tourbillonnant et tumultueux des liquides dans les lits rectilignes a grande section*. Ed. by Gauthier-Villars et fils.
- Bowler, D.E., L. Buyung-Ali, T.M. Knight, and A.S. Pullin (2010). "Urban greening to cool towns and cities: A systematic review of the empirical evidence". In: *Landscape and Urban Planning* 97, pp. 147–155.
- Buccolieri, R., C. Gromke, S. Di Sabatino, and B. Ruck (2009). "Aerodynamic effects of trees on pollutant concentration in street canyons". In: *Science of the Total Environment* 407, pp. 5247–5256.
- Buccolieri, R., S.M. Salim, L.S. Leo, S. Di Sabatino, A. Chan, P. Ielpo, G. de Genaro, and C. Gromke (2011). "Analysis of local scale tree - atmosphere interaction on pollutant concentration in idealized street canyons and application to a real urban junction". In: *Atmospheric Environment* 45, pp. 1702–1713.
- Buchhave, P. (1979). "The measurement of turbulence with the burst-type Laser Doppler Anemometer - Errors and correction methods". PhD thesis. Buffalo: Faculty of the Graduate School of State University of New York.

- Chang, C.R., M.H. Li, and S.D. Chang (2007). "A preliminary study on the cool-island intensity of Taipei city parks". In: *Landscape and Urban Planning* 80, pp. 386–395.
- Chapman, S., J.E.M. Watson, A. Salazar, M. Thatcher, and C.A. McAlpine (2017). "The impact of urbanization and climate change on urban temperatures: a systematic review". In: *Landscape Ecology*.
- Charakopoulos, A.K., T.E. Karakasidis, P.N. Papanicolau, and A. Liakopoulos (2014). "The application of complex network time series analysis in turbulent heated jets". In: *Chaos: An Interdisciplinary Journal of Nonlinear Science* 24.
- Choudhary, B.K. and A.K. Tripathi (2018). "Failing Cityscape: Urbanization and Urban Climate". In: *NGJI, An International Refereed Journal* 64, pp. 174–184.
- Damaschke, N., V. Kuhn, and H. Nobach (2018). "A fair review of non-parametric bias-free autocorrelation and spectral methods for randomly sampled data in laser Doppler velocimetry". In: *Digital Signal Processing* 76, pp. 22–33.
- Efthymiadis, D., C.M. Goodess, and P.D. Jones (2011). "Trends in Mediterranean gridded temperature extremes and large-scale circulation influences". In: *Natural hazards and earth system sciences*, pp. 2199–2214.
- F. Costa, L. da, O.N. Oliveira Jr., G. Travieso, F. Aparecido Rodrigues, P. Ribeiro Villas Boas, L. Antiqueira, M. Palhares Viana, and L.E. Correa Rocha (2011). "Analyzing and modeling real-world phenomena with complex networks: a survey of applications". In: *Advances in Physics* 60, pp. 329–412.
- Fallmann, J., S. Emeis, and P. Suppan (2014). "Mitigation of urban heat stress - a moelling case study for the area of Stuttgart". In: *Die Erde* 144, pp. 202–216.
- Fellini, S., L. Ridolfi, and P. Salizzoni (2020). "Street canyon ventilation: combined effect of cross-section geometry and wall heating". In: *Quarterly Journal of the Royal Meteorological Society*.
- Feyisa, G.L., K. Dons, and H. Meilby (2014). "Efficiency of parks in mitigating urban heat island effect: An example from Addis Ababa". In: *Landscape and Urban Planning* 123, pp. 87–95.
- Gaster, M. and J.B. Roberts (1975). "Spectral Analysis of Randomly Sampled Signals". In: *IMA Journal of Applied Mathematics, Volume 15, Issue 2*, pp. 195–216.

- Georgakis, C. and M. Santamouris (2017). "Determination of the Surface and Canopy Urban Heat Island in Athens Central Zone Using Advanced Monitoring". In: *Climate* 5.
- Giorgi, F. (2006). "Climate change Hot-Spots". In: *Geophysical Research Letters* 33.
- Godzik, S., T. Florkowski, S. Piorek, and M.M.A. Sassen (1979). "An attempt to determine the tissue contamination of *Quercus robur* L. and *Pinus silvestris* L. foliage by particulates from zinc and lead smelters". In: *Environmental Pollution* 18, pp. 97–106.
- Grilo, F., P. Pinho, C. Aleixo, C. Catita, P. Silva, N. Lopes, C. Freitas, M. Santos-Reis, T. McPhearson, and C. Branquinho (2020). "Using green to cool the grey: Modelling the cooling effect of green spaces with a high spatial resolution". In: *Science of the Total Environment* 724, pp. 1–10.
- Gromke, C. and B. Ruck (2007). "Influence of trees on the dispersion of pollutants in an urban street canyon - Experimental investigation of the flow and concentration field". In: *Atmospheric Environment* 41, pp. 3287–3302.
- (2009). "On the Impact of Trees on Dispersion Processes of Traffic Emissions in Street Canyons". In: *Boundary-Layer Meteorology* 131, pp. 19–34.
- Groß, G. (1993). *Numerical Simulation of Canopy Flow*. Ed. by Springer.
- Hunter, L.J., I.D. Watson, and G.T. Johnson (1991). "Modelling air flow regimes in urban canyons". In: *Energy and Buildings* 15, pp. 315–324.
- Iacobello, G. (2020). "Spatio-temporal analysis of wall-bounded turbulence: A multidisciplinary perspective via complex networks". PhD thesis. Turin: Politecnico di Torino.
- Iacobello, G., M. Marro, L. Ridolfi, and P. Salizzoni (2019). "Experimental investigation of vertical turbulent transport of a passive scalar in a boundary layer: Statistics and visibility graph analysis". In: *Physical Review Fluids* 4.
- Iacobello, G., S. Scarsoglio, J.G.M. Kuerten, and L. Ridolfi (2018). "Spatial characterization of turbulent channel flow via complex networks". In: *Physical Review E* 98.
- Iacobello, G., S. Scarsoglio, and L. Ridolfi (2018). "Visibility graph analysis of wall turbulence time-series". In: *Physics Letters A* 382, pp. 1–11.
- Irwin, H.P.A.H (1981). "The design of spires for wind simulation". In: *Journal of Wind Engineering and Industrial Aerodynamics* 7, pp. 361–366.

- Janhäll, S. (2015). "Review on urban vegetation and particle air pollution - Deposition and dispersion". In: *Atmospheric Environment* 105, pp. 130–137.
- Lacasa, L., L. Luque, F. Ballestreros, J. Luque, and J.C. Nuño (2008). "From time series to complex networks: The visibility graph". In: *Proceedings of the National Academy of Sciences of the United States of America* 105, pp. 4972–4975.
- Lee, K.W. and M. Ramamurthi (1993). "Filter collection". In: *Aerosol measurement, principles, techniques and applications*.
- Lin, B.S. and Y.J. Lin (2010). "Cooling Effect of Shade Trees with Different Characteristics in a Subtropical Urban Park". In: *HortScience*, pp. 83–86.
- Litschke, T. and W. Kuttler (2008). "On the reduction of urban particle concentration by vegetation - a review". In: *Meteorologische Zeitschrift* 17, pp. 229–240.
- Luque, B., L. Lacasa, F. Ballestreros, and J. Luque (2009). "Horizontal visibility graphs: Exact results for random time series". In: *Physical Review E* 80.
- Manshour, P., M. Reza Rahimi Tabar, and J. Peinke (2015). "Fully developed turbulence in the view of horizontal visibility graphs". In: *Journal of Statistical Mechanics: Theory and Experiment*, 2015.
- Marro, M., H. Gamel, P. Méjean, H. Correia, L. Soulhac, and P. Salizzoni (2020). "High-frequency simultaneous measurements of velocity and concentration within wall-bounded flows in wind-tunnel experiments". In: *Experiments in Fluids*. In press.
- Mayo, W.T.J. (1975). "Modeling laser velocimeter signals as triply stochastic Poisson processes". In: *Laser Anemometry*, pp. 455–484.
- Monin, A.S. and A.M. Obhukov (1954). "Basic Laws of turbulent mixing in the surface layer of the atmosphere". In: *Tr. Akad. Nauk. SSSR Geophys. Inst.* 24, pp. 163–187.
- Monteiro, M.V., K.J. Doick, P. Handley, and A. Peace (2016). "The impact of greenspace size on the extent of local nocturnal air temperature cooling in London". In: *Urban Forestry & Urban Greening*, pp. 160–169.
- Muller, E., H. Nobach, and C. Tropea (1998). "A refined reconstruction-based correlation estimator for two-channel, non-coincidence laser Doppler anemometry". In: *Measurement Science and Technology* 9, pp. 1437–1448.

- Murugesan, M. and R.I. Sujith (2015). "Combustion noise is scale-free: transition from scale-free to order at the onset of thermoacoustic instability". In: *Journal of Fluid Mechanics* 772.
- Murugesan, M., Y. Zhu, and K.B.L. Li (2019). "Complex network analysis of forced synchronization in a hydrodynamically self-excited jet". In: *International Journal of Heat and Fluid Flow* 76, pp. 14–25.
- Nimbus, ed. (2020). *Raccolta di dati climatici città di Torino*.
- Nobach, H., ed. (2016). *Present methods to estimate the cross-correlation and cross-spectral density for two-channel laser Doppler anemometry*. 18th International Symposium on the Application of Laser and Imaging Techniques to Fluid Mechanics. Lisbon, Portugal, 4-7 July.
- Nobach, H., E. Muller, and C. Tropea (1998). "Efficient estimation of power spectral density from laser Doppler anemometer data". In: *Experiments in Fluids* 24, pp. 499–509.
- Oake, T.R. (1982). "The energetic basis of the urban heat island". In: *Quarterly journal of the Royal Meteorological Society* 108, pp. 1–24.
- Oleson, K. (2012). "Contrasts between Urban and Rural Climate in CCSM4 CMIP5 Climate Change Scenarios". In: *Journal of Climate* 25, pp. 1390–1412.
- Oliveira, S., H. Andrade, and T. Vaz (2011). "The cooling effect of green spaces as a contribution to the mitigation of urban heat: A case study in Lisbon". In: *Building and Environment* 46, pp. 2186–2194.
- Petroff, A., L. Zhang, S.C. Pryor, and Y. Belot (2008). "An extended dry deposition model for aerosols onto broadleaf canopies". In: *Aerosol Science* 40, pp. 218–240.
- Popek, R., H. Gawronska, M. Wrochna, S. Gawronski, and A. Sæbø (2013). "Particulate Matter on Foliage of 13 Woody Species: Deposition on Surfaces and Phytostabilisation in Waxes - a 3-year Study". In: *International Journal of Phytoremediation* 15, pp. 245–256.
- Przybysz, A., A. Sæbø, H.M. Hanslin, and S.W. Gawronski (2014). "Accumulation of particulate matter and trace elements on vegetation as affected by pollution level, rainfall and the passage of time". In: *Science of the Total Environment* 481, pp. 360–369.

- Roupsard, P., M. Amielh, D. Maro, A. Coppalle, and H. Branger (2013). "Measurement in a wind tunnel of dry deposition velocities of submicron aerosol with associated turbulence onto rough and smooth urban surfaces". In: *Aerosol Science* 55, pp. 12–24.
- Salizzoni, P. (2006). "Mass and momentum transfer in the Urban Boundary Layer". PhD thesis. Turin: Politecnico di Torino and École Centrale de Lyon.
- Salizzoni, P., L. Soulhac, and P. Mejean (2009). "Street canyon ventilation and atmospheric turbulence". In: *Atmospheric Environment* 43, pp. 5056–5067.
- Salizzoni, P., R. Van Liefferinge, L. Soulhac, P. Mejean, and R.J. Perkins (2009). "Influence of wall roughness on the dispersion of a passive scalar in a turbulent boundary layer". In: *Atmospheric Environment* 43, pp. 734–748.
- Soulhac, L., P. Salizzoni, Cierco F.X., and R. Perkins (2011). "The model SIRANE for atmospheric urban pollutant dispersion; part I, presentation of the model". In: *Atmospheric Environment* 45, pp. 7379–73395.
- Ulbrich, U., E. Xoplaki, S. Dobricic, et al. (2013). "Past and Current Climate Changes in the Mediterranean Region". In: *Regional Assessment of Climate Change in the Mediterranean: Volume 1: Air, Sea and Precipitation and Water*, pp. 9–51.
- Unni, V.R., A. Krishnan, R. Manikadan, N.B. George, R.I. Sujith, N. Marwan, and J. Kurths (2018). "On the emergence of critical regions at the onset of thermoacoustic instability in a turbulent combustor". In: *Chaos: An Interdisciplinary Journal of Nonlinear Science* 28.
- Vardoulakis, S., B.E.A. Fisher, K.A. Pericleous, and N. Gonzalez-Flesca (2003). "Modelling air quality in street canyons: A review". In: *Atmospheric Environment* 37, pp. 155–182.
- Velte, C.M., P. Buchhave, and W.K. George, eds. (2014). *Power Spectrum Estimation of Randomly Sampled Signals*. 17th International Symposium on the Application of Laser and Imaging Techniques to Fluid Mechanics. Lisbon, Portugal, 7-10 July.
- Velte, C.M., W.K. George, and P. Buchhave (2014). "Estimation of burst-mode LDA power spectra". In: *Experiments in Fluids* 55.
- Winkler, P. (1988). "The growth of atmospheric aerosol particles with relative humidity". In: *Physica Scripta* 37, pp. 223–230.

- Xoplaki, E., J.F. González-Rouco, J. Luterbacher, and H. Wanner (2004). "Wet season Mediterranean precipitation variability: influence of large-scale dynamics and trends". In: *Climate Dynamics* 23, pp. 63–78.
- Zhou, W., G. Huang, and M.L. Cadenasso (2011). "Does spatial configuration matter? Understanding the effects of land cover pattern on land surface temperature in urban landscapes". In: *Landscape and Urban Planning* 102, pp. 54–63.
- Zhou, X.H., J.R. Brandle, E.S. Takle, and C.W. Mize (2002). "Estimation of the three-dimensional aerodynamic structure of a green ash shelterbelt". In: *Agricultural and Forest Meteorology* 111, pp. 93–108.